

**Aeroelasticity of Membrane Kites  
Airborne Wind Energy Applications**

Folkersma, M.A.M.

**DOI**

[10.4233/uuid:eae39f5a-49bc-438b-948f-b6ab51208068](https://doi.org/10.4233/uuid:eae39f5a-49bc-438b-948f-b6ab51208068)

**Publication date**

2022

**Document Version**

Final published version

**Citation (APA)**

Folkersma, M. A. M. (2022). *Aeroelasticity of Membrane Kites: Airborne Wind Energy Applications*. [Dissertation (TU Delft), Delft University of Technology]. <https://doi.org/10.4233/uuid:eae39f5a-49bc-438b-948f-b6ab51208068>

**Important note**

To cite this publication, please use the final published version (if applicable).  
Please check the document version above.

**Copyright**

Other than for strictly personal use, it is not permitted to download, forward or distribute the text or part of it, without the consent of the author(s) and/or copyright holder(s), unless the work is under an open content license such as Creative Commons.

**Takedown policy**

Please contact us and provide details if you believe this document breaches copyrights.  
We will remove access to the work immediately and investigate your claim.

# **AEROELASTICITY OF MEMBRANE KITES**

AIRBORNE WIND ENERGY APPLICATIONS



# **AEROELASTICITY OF MEMBRANE KITES**

AIRBORNE WIND ENERGY APPLICATIONS

## **Dissertation**

for the purpose of obtaining the degree of doctor  
at Delft University of Technology  
by the authority of the Rector Magnificus, prof. dr. ir. T.H.J.J. van der Hagen,  
chair of the Board for Doctorates  
to be defended publicly on  
Wednesday 7 September 2022 at 10:00 o'clock

by

**Mikko FOLKERSMA**

Master of Science in Mechanical Engineering,  
Tampere University of Technology, Tampere, Finland,  
born in Espoo, Finland.

This dissertation has been approved by the promotor.

Composition of the doctoral committee:

Rector Magnificus,	chairperson
Prof. dr. G.J.W. van Bussel,	Delft University of Technology, promotor
Dr.-Ing. R. Schmehl,	Delft University of Technology, copromotor
Dr. ir. A. Viré,	Delft University of Technology, copromotor

*Independent members:*

Prof. dr. ir. S. Hickel,	Delft University of Technology
Prof. dr. ir. J. Degroote,	Ghent University, Belgium
Prof. dr. H. Nilsson,	Chalmers University of Technology, Sweden
Dr. K. Roncin,	Centre de Recherche de l'École de l'Air, France
Prof. dr. D.A. von Terzi,	Delft University of Technology, reserve member

This research has been supported financially by the project AWESCO(H2020-ITN-642682), funded by the European Union's Horizon 2020 research and innovation program under the Marie Skłodowska-Curie grant agreement No. 642682.



*Front & Back:* Ximo studio

Copyright © 2022 by M. Folkersma

ISBN 978-94-6366-608-4

An electronic version of this dissertation is available at  
<http://repository.tudelft.nl/>.

# CONTENTS

<b>Summary</b>	<b>vii</b>
<b>Samenvatting</b>	<b>ix</b>
<b>1 Introduction</b>	<b>1</b>
1.1 Airborne wind energy . . . . .	2
1.2 Thesis goals and outline . . . . .	4
<b>2 State of the art of membrane kite aeroelasticity</b>	<b>5</b>
2.1 Membrane wing flight conditions . . . . .	5
2.2 Membrane kite types in AWE applications . . . . .	8
2.2.1 Leading edge inflatable kite . . . . .	10
2.2.2 Ram-air kite . . . . .	11
2.2.3 Single-skin kite. . . . .	11
2.3 Qualitative analysis of the flow around inflatable membrane kites . . . . .	12
2.4 Aerodynamic characterization . . . . .	15
2.5 Aeroelastic characterization. . . . .	17
2.6 Membrane wing studies. . . . .	18
2.7 Research goals . . . . .	21
2.8 Research questions . . . . .	21
<b>3 Components of a steady-state aeroelasticity membrane kite model</b>	<b>23</b>
3.1 Aerodynamics and turbulence modeling . . . . .	23
3.2 Transition model . . . . .	24
3.3 Mesh generation . . . . .	25
3.4 Structural mechanics . . . . .	26
3.5 Aeroelastic coupling . . . . .	27
3.6 Present computational setup . . . . .	29
3.7 Verification: cavity with membrane bottom. . . . .	34
3.8 Conclusions. . . . .	36
<b>4 Aerodynamics of leading edge inflatable kite airfoils</b>	<b>37</b>
4.1 Introduction . . . . .	38
4.2 Numerical model . . . . .	39
4.3 Validation assessment . . . . .	41
4.4 Results . . . . .	43
4.5 Conclusions. . . . .	47

---

<b>5</b>	<b>Aerodynamics of a leading edge inflatable kite</b>	<b>49</b>
5.1	Introduction . . . . .	50
5.2	Methodology . . . . .	50
5.3	Results . . . . .	54
5.4	Conclusions. . . . .	58
<b>6</b>	<b>Aeroelasticity of a ram-air kite</b>	<b>59</b>
6.1	Introduction . . . . .	59
6.2	Methodology . . . . .	60
6.3	Results . . . . .	63
6.3.1	Rigid pre-inflated kite . . . . .	63
6.3.2	Flexible kite . . . . .	64
6.4	Conclusions. . . . .	69
<b>7</b>	<b>Conclusions and recommendations</b>	<b>71</b>
7.1	Main findings of this work . . . . .	71
7.2	Recommendations for future research . . . . .	74
	<b>References</b>	<b>77</b>
	<b>Acknowledgements</b>	<b>83</b>
	<b>List of Publications</b>	<b>85</b>

# SUMMARY

The climate actions defined by United Nations require a rapid transition to low environmental footprint technologies. The energy sector is the major emitter of carbon dioxide emissions and a significant contributor to extracting resources for fuel and power plant construction materials. Wind energy is projected to produce a significant share of electricity and energy in the following decades. The wind turbines have a small footprint during the operation, but the turbine with its foundation is a massive structure with a significant material footprint. Airborne wind energy uses tethered devices to harness high-altitude wind energy, substantially reducing bulk material use. However, better models are required to make the systems reliable and efficient.

This thesis focuses on membrane traction kites that harness wind energy by flying fast crosswind maneuvers. A high-fidelity aeroelastic model for the kites is developed to predict the aerodynamic loads and the structural deformations of real systems. The aeroelastic model assumes that the membrane kite flight can be modeled as multiple steady-states without memory from the past. The steady-state aerodynamics are simulated by solving the incompressible Reynolds-averaged Navier-Stokes equations numerically. High-quality numerical grid generation strategies are developed for the unconventional wing shape of the membrane kites.

The membrane kites are tensile structures, and therefore a finite element model with cable and membrane elements without rotational degrees of freedom is used to calculate the deformed shape. The solver calculates the average surface without wrinkles and applies an additional model when an element is under compression. The steady-state response of the structure is calculated with a dynamic relaxation technique. The two solvers are coupled in a partitioned manner, and during each iteration, both solvers compute a steady state. The staggered approach requires several coupling iterations to converge. The fluid mesh needs to be altered to the deformed geometry during each iteration, and therefore, the mesh is deformed with radial basis function with greedy point selection.

This thesis presents three computational studies with the framework. The first two studies focus on the aerodynamics of rigidized LEI kite airfoil and wing. The aerodynamic model is validated with an already existing wind tunnel experiment on a similar airfoil. Generally, the largest model uncertainty in CFD is the mesh and therefore, the uncertainty is assessed by mesh refinement studies. A range of flight conditions is simulated by varying the inflow angle of attack, sideslip angle and Reynolds number. The flow around the wing is characterized by a recirculation zone behind the leading edge tube due to the lack of second skin. The zone is highly influenced by the inflow conditions. The effect of the chordwise inflatable tubes on aerodynamics is assessed by creating a model with and without them. The results show that the chordwise tubes have an almost negligible impact on the aerodynamic forces, which suggests they could be left out of the aerodynamic model in future work, simplifying the mesh generation and mesh

deformation.

The third study shows the aeroelasticity of a ram-air kite for several power configurations by changing the trim of the bridle lines. The kite forms a typical ram-air shape with ballooning in between ribs, and the nose of the wing is flattened at the stagnation region. The aerodynamics of the flexible kite is compared to a rigidized version of it. The wing is fixed at the symmetry plane and fixed to the pre-inflated shape with stagnation pressure. The results show that the flexible kite is aerodynamically more efficient than the rigidized version. The morphing wing adapts itself to the incoming flow in a way that extends the range of feasible flight conditions and improves efficiency. The aeroelastic framework converges satisfactorily with all the power setups, and it is computationally relatively inexpensive for fidelity. Consequently, the framework could be integrated into a membrane kite design process and could be a valuable asset in evaluating kite designs.

# SAMENVATTING

De klimaatacties van de Verenigde Naties vereisen een snelle transitie naar technologieën met een lage ecologische voetafdruk. De energiesector is de grootste uitstoter van koolstofdioxide en een aanzienlijke verbruiker van grondstoffen voor brandstof en bouwmaterialen voor energiecentrales. Windenergie zal naar verwachting de komende decennia een groot deel van de elektriciteit en energie produceren. Windturbines hebben een kleine voetafdruk over hun levensduur, maar de turbine met haar fundering is een massieve constructie met een aanzienlijke materiële voetafdruk. Airborne windenergie maakt gebruik van een vliegend apparaat dat aan de grond bevestigd is met een kabel. Hiermee kan op grote hoogtes windenergie worden opgewekt zonder toren en zware fundering, waardoor aanzienlijk wordt bespaard op materiaalgebruik. Er zijn echter betere simulatiemodellen nodig om deze systemen betrouwbaar en efficiënt te maken.

Dit proefschrift richt zich op membraanvliegers, die windenergie opwekken door snelle manoeuvres te maken dwars op de windrichting. Voor dit soort vliegers is een high-fidelity numeriek aero-elastisch model ontwikkeld, om daarmee de aerodynamische belastingen en de structurele vervormingen van echte systemen te voorspellen. Uitgangspunt bij het aero-elastische model is dat de vlucht van de vlieger kan worden gemodelleerd als aaneenschakeling van meerdere steady states zonder terugkoppeling naar eerdere toestanden. De steady-state aerodynamica wordt gesimuleerd door de incompressibele Reynolds-gemiddelde Navier-Stokes vergelijkingen numeriek op te lossen (CFD modellen). Er zijn verschillende strategieën ontwikkeld voor het genereren van een hoogwaardig numeriek rooster (mesh) voor de onconventionele vleugelvormen van membraanvliegers.

Membraanvliegers zijn structuren die op trek worden belast en daarom kan een eindig-elementenmodel met kabel- en membraanelementen gebruikt worden om de vervorming te berekenen. Rotatie vrijheidsgraden in de elementen worden daarbij niet meegenomen. De rekenmethode berekent het gemiddelde oppervlak zonder kreukels en gebruikt een extra model wanneer een element toch onder druk blijkt te staan. De steady-state respons van de constructie wordt berekend door middel van dynamische relaxatie. De twee rekenmodellen zijn gepartitioneerd gekoppeld, en met elke iteratie berekenen beide modellen een steady state. Deze stapsgewijze benadering vereist meerdere koppelingssiteraties om te convergeren. De mesh waarmee de stroming wordt berekend moet tijdens elke iteratie worden aangepast aan de vervormde geometrie en daarom wordt de mesh vervormd met een radiale basisfunctie met een lokaal optimale (greedy) puntenselectie.

In dit proefschrift worden drie numerieke studies gepresenteerd tezamen met het raamwerk voor de koppeling van aero-elastische modellen met een eindige elementen model. De eerste twee studies richten zich op de aerodynamica van een stijf Leading Edge Inflatable (LEI) vliegerprofiel en vleugel. Het aerodynamische model is gevalideerd

met een reeds bestaand windtunnel experiment met een vergelijkbaar profiel. Over het algemeen is de grootste modelonzekerheid in CFD modellen de mesh en daarom wordt de onzekerheid beoordeeld door mesh-verfijningsstudies. Een reeks van vluchtcondities wordt gesimuleerd door het variëren van de invalshoek van de instroom, de zijsliphoek en het Reynoldsgetal. De stroming rond de vleugel wordt gekarakteriseerd door een recirculatiezone achter de voorrandbuis door het ontbreken van een tweede huid. Deze zone wordt sterk beïnvloed door de instroomomstandigheden. Het effect van de opblaasbare buizen in de koorde richting op de aerodynamica wordt beoordeeld door ook een model zonder deze buizen te maken. De resultaten laten zien dat de koordebuisen een bijna verwaarloosbare invloed hebben op de aerodynamische krachten. Dit suggereert dat ze uit het aerodynamische model kunnen worden weggelaten, waardoor het genereren van een mesh en de vervorming ervan eenvoudiger wordt.

De derde studie betreft de aero-elasticiteit van een ram-air vlieger voor verschillende krachtenconfiguraties door de trim van de hoofdstellijnen te veranderen. De vlieger heeft een typische ram-air vorm met ballondelen tussen de ribben, en een neus van de vleugel die is afgeplat in het stagnatiegebied van de stroming. De aerodynamica van deze flexibele vlieger wordt vergeleken met de starre versie van dezelfde vlieger. De vleugel is in de numerieke studie gefixeerd op het symmetrievlak en heeft een, door stagnatiedruk vooraf opgeblazen vorm. De resultaten laten zien dat de flexibele vlieger aerodynamisch efficiënter is dan de starre versie. De vervormbare vleugel past zich aan op de inkomende stroming op een manier die het bereik van mogelijke vliegomstandigheden vergroot en de efficiëntie verbetert. Het aero-elastisch raamwerk convergeert naar tevredenheid voor alle gekozen waarden van het vermogen en is in rekentijd relatief goedkoop voor de verkregen betrouwbaarheid. Het raamwerk kan daarmee worden geïntegreerd in een ontwerpproces voor membraanvliegers en kan een waardevolle aanwinst zijn bij het evalueren van vliegerontwerpen.

# 1

## INTRODUCTION

Since the industrial revolution in the 18th century, human productivity has increased drastically through powerful machines driven by fossil fuels instead of human and other animal labor. Consequently, human work has freed up from essential industries, such as agriculture, to new, less critical industries and has allowed a continuous increase in the standard of living. The exponential growth, both in productivity and human population, has increased the human impact on the planet to a scale that humans harness nearly every corner of it, and the intensity keeps on growing. Consequently, the ecological systems have been altered up to a level that the risk of crossing one or more tipping points has become high. Exceeding these thresholds will lead to a series of irreversible events, leading to an undesirable environment for humans and other species. We are already facing many symptoms of environmental crisis, such as global warming, mass extinction events, soil erosion, and air and water pollution.

Humanity has faced environmental crises by developing green technology. The idea of growth has remained but through green growth, which aims to decouple the economic growth from resource use. The advancement of green technology has been rapid. The most important branch of green technology is energy production since it enables other activities and is the main contributor to carbon dioxide (CO<sub>2</sub>) emissions. The level of CO<sub>2</sub> in the atmosphere amplifies the greenhouse effect and increases the Earth's surface temperature, as predicted by Arrhenius already more than a century ago [1]. The development of renewable energy technology with low CO<sub>2</sub> emissions has been stunning. For instance, the wind energy levelized cost of energy (LCOE) has decreased 70 % from 0.14 USD/kWh in 2000 to 0.04 USD/kWh in 2020 [2]. The average unit size and the rotor diameter have increased dramatically and turbines reach higher altitudes with better wind conditions. Similar rapid advancements have also occurred in solar power [2]. Consequently, wind and solar power have become the cheapest form of energy in many places on the Earth, and therefore, their production has 80 folded from 30 TWh in 2000 to 2450 TWh in 2020 [3].

The efforts and the development of green energy technology have been enormous. However, despite the growth, the prevention and mitigation of the environmental crisis

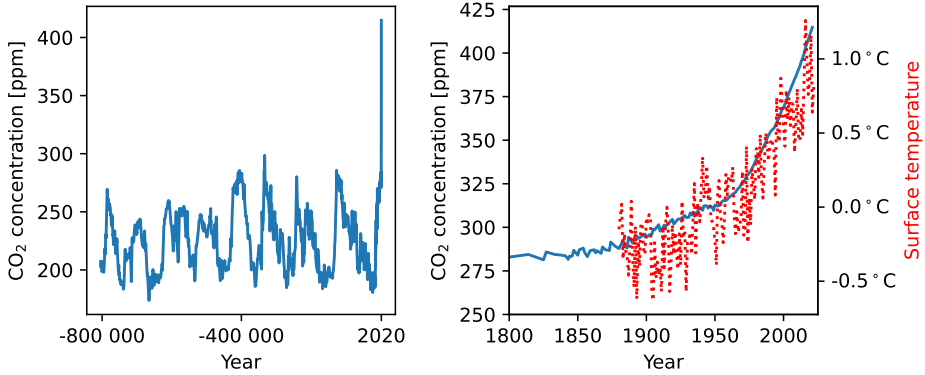


Figure 1.1: Time series of CO<sub>2</sub> levels in the atmosphere and surface temperature [4, 5].

has failed. Figure 1.1 shows a time series of CO<sub>2</sub> levels in the atmosphere and the surface temperature. Unfortunately, since the beginning of 2000, the yearly CO<sub>2</sub> emissions have increased by around 50 %, and the goal set up by the Paris agreement in 2015 to prevent the global average temperature from rising above 1.5 °C or at least limit the rise well below 2 °C since the pre-industrial levels seem already unreachable. The intermediate scenario in the latest United Nations report predicts a temperature rise of 2.7 °C with the current pledges [6]. Thus, while the amount of green technology has increased rapidly, consumption has grown even faster, and consequently, the human footprint on Earth has kept growing.

While it is clear that the transition to green growth is not enough and a more fundamental change is necessary, more resource-efficient ways to harness energy are still needed. Wind and solar power are the most promising energy sources with low carbon intensity, fast deployment and high scalability. However, they also come with challenges, such as power variability, and the plants are rather material intense.

## 1.1. AIRBORNE WIND ENERGY

Airborne wind energy (AWE) is a novel renewable energy technology that uses tethered flying devices to harness wind energy with minimal material input. One of the main advantages of airborne wind energy system (AWEs) over wind turbines is the significantly lower bulk material use due to three reasons: (1) the foundation is tiny because it has to only counteract the tether traction instead of the bending moment, (2) no tower is required, but the kite is attached to the ground by tethers and (3) the whole wing is exposed to high crosswind speed without the inefficient root of the wind turbine blade. Additionally, AWE systems can adjust their altitude to the best wind conditions and therefore, even small-scale systems could be economically feasible. Nevertheless, a long tether length induces inefficiencies, such as line drag and mass. The AWE technology is in its infancy because only the first commercial small-scale systems are beginning to emerge. Thus, the reliability and robustness of the technology pose uncertainties because the

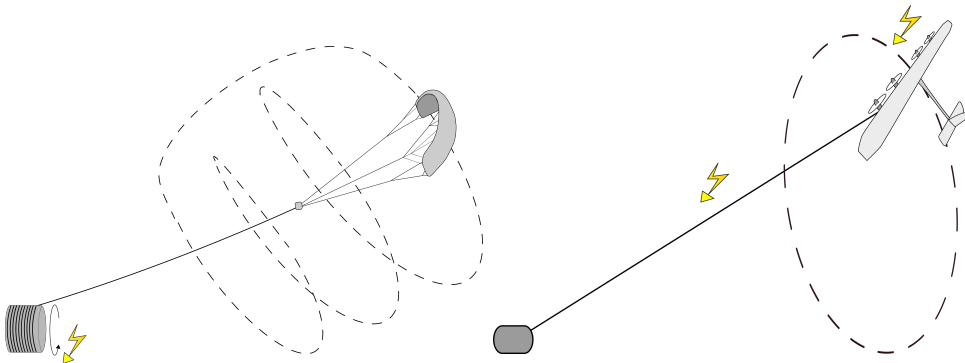


Figure 1.2: Illustration of ground gen system with a membrane kite (left) and a fly-gen system with a fixed wing kite (right) [7].

tests have only covered small-scale systems for relatively short time periods. From the technological point of view, the main uncertainties are durability, autonomous flight operations and the scalability to megawatt-scale. The first utility-scale systems are expected in the early 2030s.

Many different system designs exist, but the most common ones use crosswind flying wings to extract energy. Several different classifications exist for the AWEs. One of the common ways is based on the location of the generator, shown in Figure 1.2. The generator is either part of the ground station "ground gen" or mounted to the wing "fly-gen". The ground gen system operates in a pumping cycle, consisting of traction and retraction phases. The kite flies fast crosswind motion during the traction phase and reels out the tether with high tension from a winch connected to a generator. When the kite has reached a certain altitude, it is reeled back in with minimal tension, and a new traction phase begins. Another option is to mount the generators on the kite and transmit the electricity through a conductive tether. The advantage of a fly-gen system is that it has only one phase during operation, and therefore, it produces a more constant power output and uses a fixed tether length, which simplifies the flight operations.

Another way to classify the crosswind kite systems is by the wing design. Membrane kites are lightweight tensile structures composed of membranes and lines. The bridle lines support the membrane wing and merge to the control pod that hangs below the wing and connects to the tether. The control pod actuates the kite by changing the relative lengths of the bridle lines. The membrane kites typically use a ground generator. Another group is the fixed-wing kites that are built from stiff materials such as carbon fiber. The fixed-wing kite systems do not necessarily have bridles because the wing can resist compression, and the tether is directly attached to the wing. The aircraft is steered by actuating control surfaces.

Autonomous launching and landing is a critical operation for the AWE systems. Usually, the fly-gen kites use the generators as motors during the launching and landing, and the kite hovers to the required altitude. Also, some other fixed-wing ground generator systems have onboard motors for vertical taking-off and landing. Another launching concept by Ampyx Power for their fixed kite is to use a tiny runway that catapults

the wing during launching and actively uses the tether during landing. Some membrane kite launching concepts have the kite tail sitting downwind from the ground station. The tether is reeled in during the launch, which generates an apparent wind to lift the kite. Other membrane kite concepts use a telescopic mast for launching and landing.

## 1.2. THESIS GOALS AND OUTLINE

This work aims to build a methodology to study the aerodynamics of membrane kites, and the methodology should be a good compromise between model fidelity and computational cost. Also, the methodology should be robust and reliable to be integrated into the kite development process. Membrane kites are flexible structures, and therefore, to investigate aerodynamics, structural deformation has to be also considered. Consequently, the methodology is a multiphysics model, which includes two solvers, one for aerodynamics and another for structural mechanics. This work uses the methodology to study the aerodynamics of several membrane kite models. The thesis consists of the following chapters:

### Chapter 2 – State of the art of membrane kite aeroelasticity

Firstly, this chapter presents the fundamentals of membrane kite designs, aerodynamic characterization and the flight environment. Subsequently, the status quo of the research is presented, and based on it, the research goals and questions are formulated.

### Chapter 3 – Components of a steady-state aeroelasticity membrane kite model

This chapter presents the different building blocks of the aeroelastic model. The main blocks of the model are the aerodynamic and structural solver, but also the other blocks, such as the coupling approach with data exchange and mesh deformation, are presented. The coupled framework is verified with a test case from the literature.

### Chapter 4 – Aerodynamics of leading edge inflatable kite airfoils

This chapter focuses on the aerodynamics model of a rigid leading-edge inflatable kite airfoil. The model is validated with a wind tunnel experiment, and therefore the boundary layer transition has to be taken into account. Several flight conditions are presented by varying the Reynolds number and angle of attack.

### Chapter 5 – Aerodynamics of a leading edge inflatable kite

This chapter extends the work of the previous chapter to a complete rigid leading-edge inflatable kite wing. An additional parameter, sideslip angle, is also presented. The effect of chordwise inflatable beams on aerodynamics is also assessed.

### Chapter 6 – Aeroelasticity of a ram-air kite

In this chapter, the coupled model is used to study the aerodynamics of a flexible ram-air kite. The aeroelastic model is compared to a rigidized wing model to isolate the effect of flexibility on aerodynamics. Several power configurations are presented by trimming the bridle line system.

### Chapter 7 – Conclusions and recommendations

This chapter concludes the thesis by addressing the research questions and presents recommendations for future work.

# 2

## STATE OF THE ART OF MEMBRANE KITE AEROELASTICITY

The chapter begins with the fundamentals of the membrane kite powered airborne wind energy systems. The flight conditions and kite designs governing the system are presented. After the fundamentals, the relevant literature for the membrane kite aeroelasticity is discussed. Finally, based on the fundamentals and literature, the research goals and the research questions of the thesis are formulated.

### 2.1. MEMBRANE WING FLIGHT CONDITIONS

The membrane kites operate in pumping cycles that consist of alternating traction and retraction phases, as shown in Figure 2.1. During the traction phases, the kite flies close to the so-called power zone, downwind from the ground station, and the bottom surface of the wing faces the wind. The kite flies rapid crosswind maneuvers to increase the apparent wind velocity, aerodynamic forces, and ultimately the power output. During these maneuvers, the angle of attack is high to maximize the lift and traction force. The tether is reeled out at the ground station with high tension from a drum that drives the generator. During the retraction phases, the kite is depowered by lowering the angle of attack. The kite flies above the ground station without crosswind maneuvering, and the tether is reeled in with minimal tension.

The components of a membrane kite are shown in Figure 2.2. The main components are the wing, bridle line system and kite control unit (KCU). The wing converts the kinetic energy of the wind into aerodynamic loads. The loads are transmitted through the bridle line system to the tether that connects the kite to the ground station. The kite is steered by the KCU that hangs below the wing. The KCU has two winches that alternate the proportional line lengths of the bridle lines: one that controls the power setup and another one that steers the kite. Reeling the depower tape changes the pitch of the wing, which changes the angle of attack. The steering winch changes the relative length of the right and the left steering lines and the asymmetric actuation turns the kite through yaw

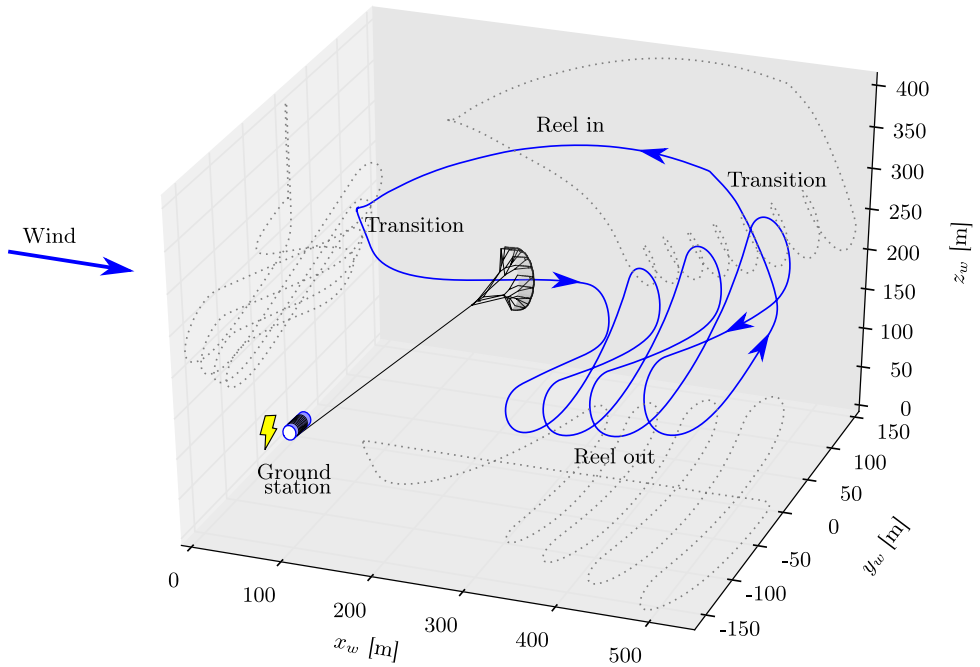


Figure 2.1: Pumping cycle flight path [8].

and roll.

The membrane kite is usually launched either with a winch or a telescope mast. In the winch launch, the kite is tail-sitting downwind from the ground station. The wing generates a lift force and the kite takes off. In low wind conditions, the ground station can reel in the kite to increase the apparent wind velocity and lift. During the landing, the kite soars slowly to the side of the ground station. For a relaunch, the kite has to be carried back to the downwind location. In the mast launch, the kite is elevated to a relatively high altitude, and the kite is released from the mast. The kite is reeled back close to the mast and fastened again during the landing. The mast launch allows a higher degree of autonomy than the winch launch because it requires less ground handling, and the wind conditions are better at high altitudes. The launching and landing are critical operations that greatly impact the wing design. The kite flies close to the ground with a short tether length that induces fast angular accelerations and turbulent wind conditions from the wind shear. The kite also has low tension, making it more vulnerable to disturbances due to their proportionally higher impact than for a tensioned wing. Consequently, the wing design cannot only be optimized for the highest aerodynamic efficiency, but it must also be robust, which is usually an opposite requirement to efficiency.

In addition to the wind, the kites are affected by precipitation and sunlight. The lightweight kites are sensitive to the rain, especially when depowered. The rainwater increases the weight of the wing, which has to be taken into account in the kite design and flight controller. The sunlight radiation poses another challenge to the durability

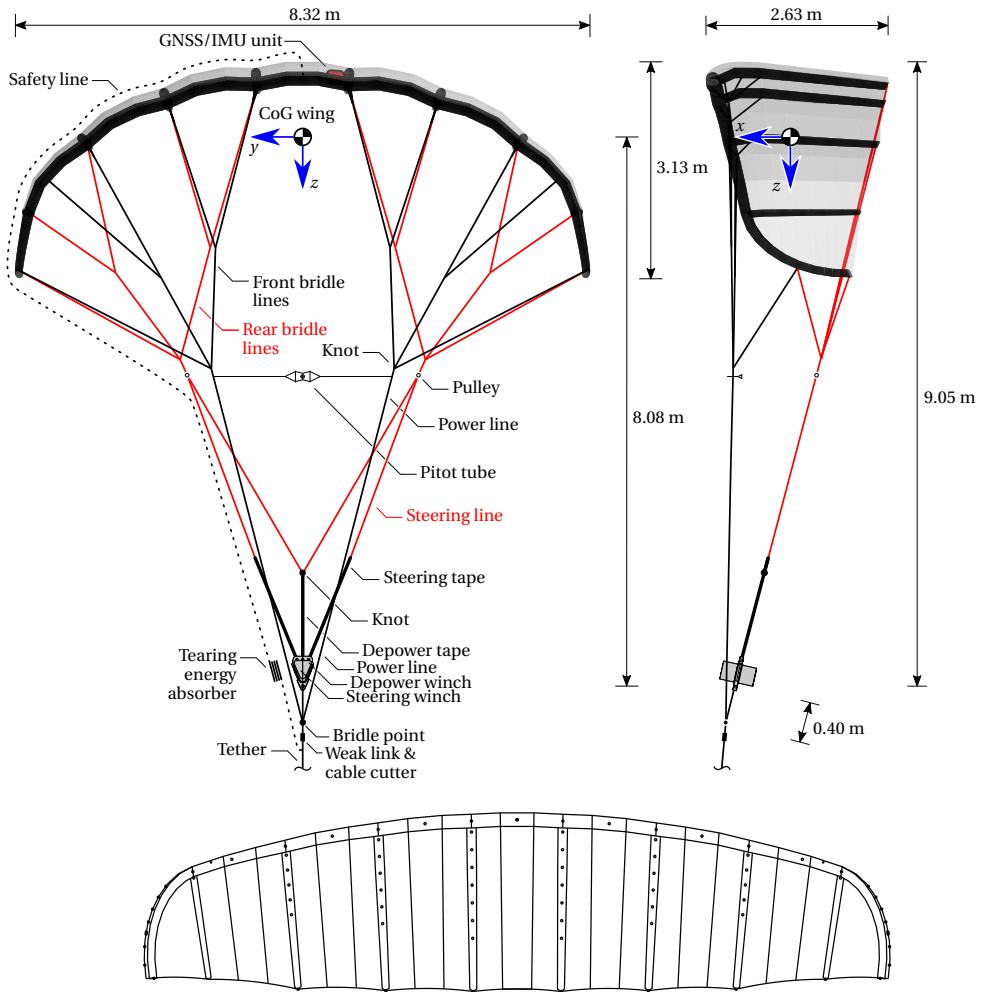


Figure 2.2: TU Delft V3 kite in front view (left), side view (right) and unrolled planform view (bottom) [9].



Figure 2.3: Membrane traction kite designs: leading edge inflatable (left)[9], ram-air (center) [10] and single skin (right)[11].

of the membrane kites. The radiation deteriorates the membranes rather quickly, and therefore the kites need to be replaced several times during the lifespan of the system. The use of hydrophobic and ultraviolet resistant materials can mitigate both disadvantageous effects.

## 2.2. MEMBRANE KITE TYPES IN AWE APPLICATIONS

The membrane kite designs in AWE systems are similar to the kite surfing designs. Figure 2.3 shows the common kite designs. The membranes are usually made of woven fabrics, such as Nylon and Polyester, because of their strength and durability [13]. The wings consist of several membrane sheets that are joined together. The woven fabrics are stitched together with straight and zig-zag seams and foldings. The typical membrane kite wing configurations share the following properties:

### 1. Low aspect-ratio

The ratio of the span to the average chord is called the aspect ratio of the wing. Compared to the conventional airplane wings, the aspect ratio of the membrane wings is relatively low. A high aspect ratio increases the efficiency of the wing by decreasing the relative effect of the wingtip vortices, especially in the case of traction kites, which operate with a high angle of attack and high lift coefficient. However, a low aspect ratio wing turns faster, is less prone to disturbances, and has a lower bending moment and torque in spanwise direction, requiring less spanwise reinforcements.

### 2. High anhedral

The anhedral angle is the curvature of the wing as looking from the front (Figure 2.2). The membrane kite designs usually have almost a half-circle arc. The anhedral arc maintains the spanwise tension by introducing a side force (local lift vector), which points outwards more and more towards the wingtip. The membranes do not have any compression strength, and therefore the anhedral is required to maintain the spanwise tension. Moreover, the efficient steering mechanism based on deforming the wing is dependent on the anhedral [14]. However,

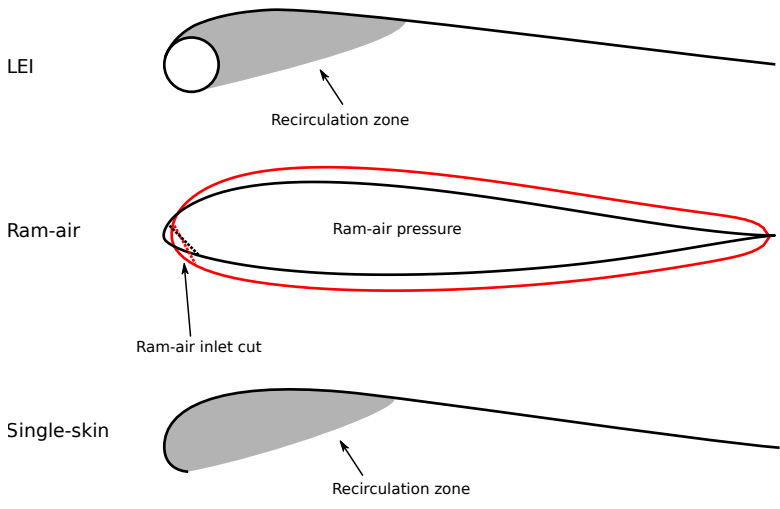


Figure 2.4: Kite airfoils. The black line shows the design shape and the red line shows the inflated (ballooned) shape of the ram-air airfoil in between ribs. Grey areas depict flow separation and recirculation zones.

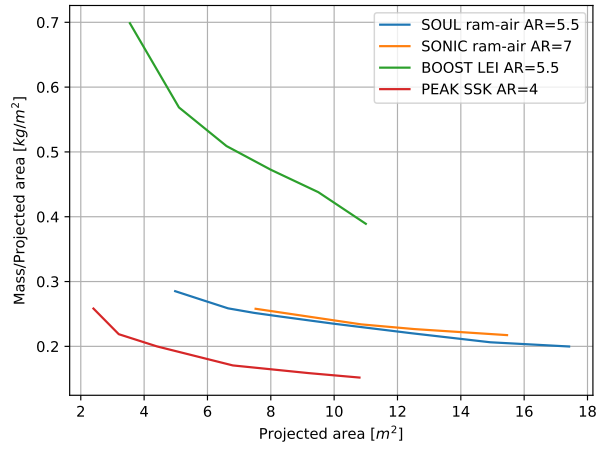


Figure 2.5: The mass per effective projected area of the Flysurfer's surf kites. The data is collected from Flysurfer's website [12].

the anhedral also reduces the effective projected area, which increases the form drag and the mass of the wing [15]. The lift force is proportional to the projected area, while the form drag is proportional to the wetted area of the wing.

### 3. Tapered/semi-elliptical

A common wing planform for membrane kites has a semi-elliptical shape which is straight at the trailing edge and elliptical at the leading edge. The tapering of the wing both improves the aerodynamic efficiency by reducing the lift-induced drag and the aerodynamic forces towards the wingtip.

The membrane kites contain a bridle line system that collects the forces from the wing and transfers them to the tether. The bridling reduces the magnitude of the stresses in the membranes. Consequently, the more bridle lines, the less anhedral is required, and the membranes can be thinner and lighter. However, the higher the number of lines, the higher the total line drag. The bridle lines also stabilize the wing in roll and pitch directions compared to fixed-wing single line traction kites. The bridle line system builds up a reaction moment to balance the roll and pitch moment. The bridle lines along the span balance the roll (front view in Figure 2.2) and the lines along the chord balance the pitch (side view in Figure 2.2).

The common membrane kite designs can be classified into three categories (Figure 2.3): leading edge inflatable (LEI), ram-air and single-skin. Figure 2.5 shows a comparison of the mass per projected area and the scaling of the commercial surf kites. Note that in kite surfing, the designed traction force of the kite remains approximately constant as the kite surface area grows. The larger kite designs are for lower wind velocities, and therefore the tensile forces in the membrane remain rather constant. While in AWE, scaling up aims to generate higher traction force, and therefore, the tensile forces increase linearly with the surface area. Then, the membrane thickness must increase, or more reinforcements and bridle lines are required. Hence, a similar downward trend for the specific mass can not be expected for the AWE kites when scaling up. Generally, a low specific mass is a desirable property as it allows operating the system at low wind speeds. However, lightweight wings are also more prone to disturbances such as rain and gusts, as mentioned earlier.

#### 2.2.1. LEADING EDGE INFLATABLE KITE

The LEI kite has a single skin membrane that is supported by an inflatable tubular frame, shown in Figure 2.2 and Figure 2.3 (left). The tubes are pre-inflated to high pressure and distribute the aerodynamic loads from the canopy into the bridle line system. The pre-inflated tubes of the LEI kite provide stiffness to the wing in addition to the tensile stresses by the anhedral. The inflation generates a tensile state in the membrane, and consequently, the wing can sustain bending and compressive loads. The added stiffness is essential during the low wind speeds (launching, landing and retraction phase) when the wing is more prone to disturbances.

The LEI kites have the highest mass per projected area out of the three types of kites. The tubes have to both resist the high-pressure load and be leakproof, and therefore they contain two membrane layers. The outer layer is the load-bearing woven fabric, and the inner layer is an airtight bladder. The diameter of the tubes is around 5-10% of the chord

length of the section to keep a reasonable airfoil shape.

At the junction of the leading edge tube and the canopy, the flow behind the tube separates and forms a recirculation zone on the pressure side. The outer flow reattaches further along the chord. These separation zones form for any normal angles of attack and the size of the zones depend on the angle of attack. On the suction side, the airfoil is smooth and similar to conventional double skin airfoils. The lift coefficient of an LEI kite airfoil is relatively high compared to a conventional airfoil, but the recirculation zone increases the drag coefficient, which results in lower glide ratios than the conventional double skin airfoil [16]. The flow around an LEI kite airfoil is further discussed in Chapter 4.

### 2.2.2. RAM-AIR KITE

Ram-air wings have cellular membrane structures inflated by the exterior flow through openings on the leading edge, shown in Figure 2.3 (middle). The distributed aerodynamic load on the top and bottom skin of the wing is collected by chordwise membrane ribs and transmitted to the main tether via fans of bridle lines. Ram-air wings do not have similar pre-tension as the LEI wings. Therefore, more bridle lines are required to prevent the wing from collapsing and retaining its flight shape [17]. Additionally, the lack of spanwise tension, especially when depowered, limits the aspect ratio of the wing [18].

The ram-air wing has a conventional double skin airfoil (Figure 2.4) with a relatively high thickness that is maximum at around 20% of the chord length [17]. In between the ribs, the airfoil balloons, which results in the typical cellular structure. Although the inflation pressure of the ram-air wing is low compared to the LEI kite tubes, the large cross-sectional area results in moderate bending stiffness. While the double-skin airfoil is superior in terms of glide ratio, the weight and the complexity of the wing are high compared to the single skin designs. Additionally, the leading edge cut and ballooning in between the ribs reduce the aerodynamic efficiency of the kite [19].

### 2.2.3. SINGLE-SKIN KITE

The single-skin kite shown in Figure 2.3 (right) is a pretty novel design in kite surfing and paragliding [11, 20], which has also received some interest in the AWE industry [21]. The single skin kite has only one skin on the suction side, which slightly extends to the pressure side at the leading edge (Figure 2.4 bottom). The minimal design of a single-skin kite saves material and weight. It is also easier to manufacture than the two other membrane kite designs.

Interestingly, the absence of the pressure side membrane increases the lift coefficient in comparison to the same airfoil with the two skins [21]. Similarly to the LEI kite airfoil, the recirculation zone behind the leading edge structure increases the drag coefficient, and therefore the glide ratio of a double skin airfoil is higher [16, 21]. Because of the minimal support structure, the single skin kites have less feasible options for the wing configuration. Moreover, single-skin kites are most prone to disturbances, which limits the depowering capability and may decrease the lifespan of the wing.

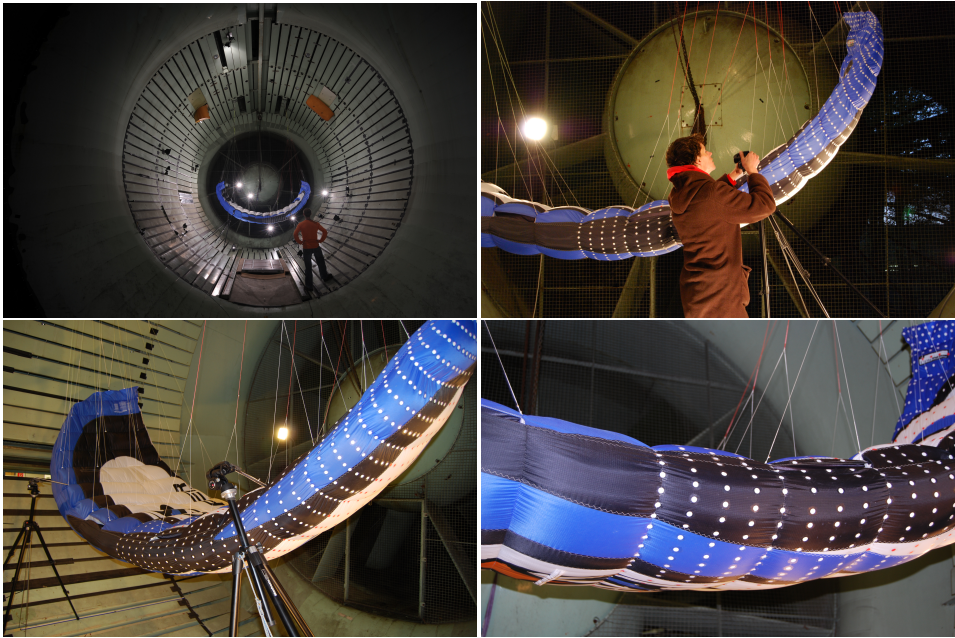


Figure 2.6: Experimental setup of the Pulse 2 ram-air kite in Böenwindkanal of the University of Stuttgart, Germany. The photos were shot by Max Dereta.

### 2.3. QUALITATIVE ANALYSIS OF THE FLOW AROUND INFLATABLE MEMBRANE KITES

In May 2008, a TU Delft team conducted wind tunnel tests of a commercial ram-air kite and an inhouse-developed kiteplane in the Böenwindkanal of the University of Stuttgart, Germany. The objective of these tests was to investigate the structural and aerodynamic characteristics of the two tethered lifting devices. The tests have been used as the basis of the MSc theses of Aart de Wachter [22] and Merlin Bungart [23] as well as the PhD thesis of Jeroen Breukels [14].

The Böenwindkanal is an open wind tunnel with the test section located upstream of a large propeller, which generates a maximum suction flow velocity of 17 m/s. The flow around the wing is visualized with a hand-held probe that is connected to a smoke generator. In a first series of tests, a Pulse 2 ram-air kite, manufactured by Flysurfer, was tested. The kite was suspended from the ceiling of the test chamber such that the lift force acted downwards. To ensure a static position of the wing, two points on the leading edge were attached to repurposed photo tripods that were anchored at the tunnel wall. One half of the wing was equipped with an array of 2000 circular marker stickers with the purpose to use photogrammetry to measure the deformed shape of the wing.

The photos in Figure 2.6 show the suspension of the wing in the test section (top, left), the attachment of the wing to one of the tripods (top, right), the finished test setup (bottom, left) and the leading edge of the wing in close-up (bottom, right). The close-



Figure 2.7: Kiteplane in Böenwindkanal of the University of Stuttgart, Germany. The photos were shot by Max Dereta.



Figure 2.8: Smoke flow visualization near the symmetry plane leading edge opening of the Pulse 2 ram-air kite wing.

up photo also shows how the inflatable wing is built from different textile patches that are sewn together. The wing sections are ballooned only slightly as the wing is not yet inflated. Once the wing is exposed to the relative flow, during test or flight operation, the ram-air inflation pressure that acts via two openings in the leading edge (bottom, left) and the inflatable structure stiffens, and the ballooning becomes more pronounced.

In a second series of tests, shown in Figure 2.7, a kiteplane was investigated, which was designed from inflatable tubes and canopy material similar to leading edge inflatable (LEI) tube kites. The aerodynamics of a wing section is identical to that of an LEI tube kite, with the difference that the kiteplane has a wing with positive dihedral and a tailplane for stabilization and steering [13, 24]. Also, the leading edge of the kiteplane is made of two parallel joined tubes to improve the aerodynamics (Figure 2.9). The photo on the left shows the free hanging wing with circular marker dots for photogrammetry on one half of the main wing, the photo on the right shows the fixation of the leading edge to one of the two tripods.

The two-dimensional flow over the wing can be best observed close to the symmetry plane of the wing because this area is least affected by the three-dimensional flow components that govern the flow field towards the wing tips. The following photos in Figure 2.8 show the flow over the suspended ram-air wing. In the left photo, the smoke

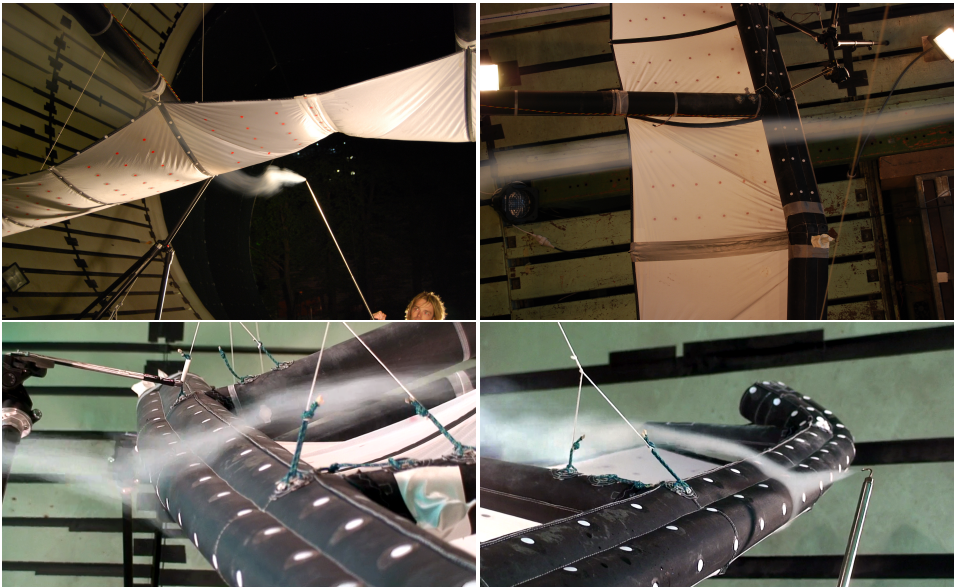


Figure 2.9: Smoke flow visualization around the kiteplane. The photos were shot by Max Dereta.

trail indicates the flow impinging on the leading edge of the wing, close to the stagnation point, and the subsequent flow along the suction side. The stagnation point splits the incident flow into two streams, one stream along the suction side and one stream along the pressure side. This is shown in the right photo, in which the smoke trail impinges on the opening of the wing. This opening is placed close to the stagnation point, the point in the flow field where the static pressure is maximum, to maintain the interior pressure of the wing. It is visible that this opening does not lead to a strong perturbation of the exterior flow. Not visible in these visualizations are the boundary layers that are evolving along the two sides of the wing. Because of the wrinkles in the textile material and the spanwise seams and construction features, it is commonly assumed that the boundary layers are turbulent very early on, i.e., there is no free transition from laminar to turbulent boundary layer.

The next series of photos in Figure 2.9 shows the flow over the inflatable main wing of the kiteplane. The two top photos visualize the flow along the suction side (left) and pressure side (right) at some distance from the wing. The two bottom photos visualize the flow splitting at the stagnation point into a stream along the suction side and a stream along the pressure side. The smoke trail on the pressure side indicates that the flow separates from the leading edge tube and passes over a recirculation zone, which we know from numerical simulations and other experimental methods. There is no noticeable entrainment of smoke into the recirculation zone.

In a next step, the three-dimensional flow phenomena are analyzed for the ram-air wing. The two photos in Figure 2.10 show the wingtip vortex that is part of the vorticity system generated by the wing. The pressure gradient from the pressure side to the suction side of the wing creates a transverse flow component around the wingtip, which



Figure 2.10: Smoke flow visualization near the wingtip of the Pulse 2 ram-air kite. The photos were shot by Max Dereta.

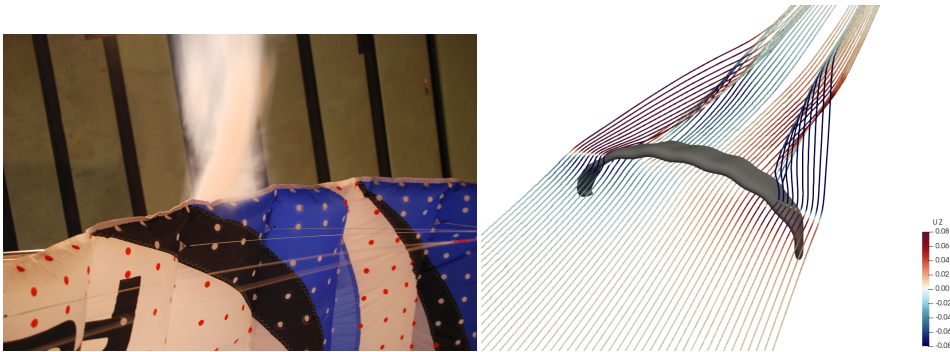


Figure 2.11: Smoke flow visualization behind the trailing edge (left) and streamlines extracted from CFD simulation (right) showing the twisted wake flow. The photos were shot by Max Dereta.

combines with the background flow into the characteristic tip vortex. Streamlines twisting up in the wake flow of the wing, visualizing the trailing vorticity generated by the spanwise lift distribution on the wing (Figure 2.11). The streamline visualization is taken from Demkowicz [25], in which streamlines are released from a straight transverse line upstream of the wing.

## 2.4. AERODYNAMIC CHARACTERIZATION

In addition to the wing shape, the main parameters to characterize the aerodynamics are the angle of attack, sideslip angle and the Reynolds number. The Reynolds number is the ratio between the inertial forces and the viscous forces and helps to categorize the flow. Low Reynolds number flows are laminar and dominated by viscous forces. High Reynolds number flows are turbulent and dominated by inertial forces. In a turbulent flow, the smallest time and length scales of the turbulent eddies are inversely proportional to the Reynolds number, while the largest scales mainly depend on the size of the wing. Consequently, the range of length scales increases with the Reynolds number. Moreover, the Reynolds number influences the boundary layer characteristics, such as

the boundary layer thickness, the wall friction, and the separation resistance in case of an adverse pressure gradient. In this work, two Reynolds numbers are used: one based on the center chord length ( $c$ ) and another one based on the leading edge tube diameter ( $d$ ),

$$\text{Re} = \frac{U_\infty c}{\nu} \quad (2.1)$$

$$\text{Re}_d = \frac{U_\infty d}{\nu} \quad (2.2)$$

where  $U_\infty$  is the apparent wind velocity, that is the sum of the wind speed and wing velocity, and  $\nu$  is the kinematic viscosity of the air.

The aerodynamic force is the sum of the pressure and shear distribution acting on the wing. It is commonly resolved in three components with respect to the apparent wind direction. The drag ( $D$ ) direction is parallel to the apparent wind direction, and the lift ( $L$ ) and the side-force ( $Y$ ) directions are perpendicular to the apparent wind direction. Lift is in the plane of symmetry, pointing up, and the side-force is positive in the opposite direction to the  $y$ -axis. The angle of attack ( $\alpha$ ) and the side-slip angle ( $\beta$ ) are the angles between the apparent wind velocity and the chord line when looking from side and top view, respectively. Drag, side-force and lift coefficients are calculated from the aerodynamic forces as follows:

$$C_D = \frac{D}{\frac{1}{2}\rho U_\infty^2 S} \quad (2.3)$$

$$C_S = \frac{Y}{\frac{1}{2}\rho U_\infty^2 S} \quad (2.4)$$

$$C_L = \frac{L}{\frac{1}{2}\rho U_\infty^2 S} \quad (2.5)$$

where  $\rho$  is the air density, and  $S$  is the projected (planform) wing area. For the two-dimensional airfoils, the chord length  $c$  is used as a characteristic length in place of the area, and the lift and drag coefficient are denoted as  $c_d$  and  $c_l$ . A common measure for the aerodynamic efficiency is the glide ratio

$$E = \frac{L}{D} = \frac{C_L}{C_D} \quad (2.6)$$

Additionally, two other non-dimensional coefficients are used, namely pressure and friction coefficient. Pressure coefficient is given by

$$C_p = \frac{p - p_\infty}{\frac{1}{2}\rho U_\infty^2} \quad (2.7)$$

where  $p$  is the static pressure and  $p_\infty$  is the freestream pressure. The friction coefficient is given by

$$C_f = \frac{\tau_w}{\frac{1}{2}\rho U_\infty^2} \quad (2.8)$$

where  $\tau_w$  is the wall shear stress.

Generally, the aerodynamic drag is divided into two categories, parasitic drag and lift-induced drag. Parasitic drag consists of form drag and skin-friction drag. Form drag arises from the pressure differences around the object as the flow passes around it. Skin friction drag is caused by the viscous forces in the boundary layer. The lift-induced drag is present for finite span wings with nonzero lift. It results from the air moving sideways from the high pressure side to the low pressure side and it is the most prominent at the wingtips where wingtip vortices are formed. This downwash is also present to some extent at the location of the wing and hence reduces the effective angle of attack, which in turn reduces the lift and increases the drag.

As shown in the previous section, in addition to the wingtip vortices, the altering spanwise shape of the wing leaves trailing vortices. Behind the peak suction on the upper side of the wing, the flow encounters an adverse pressure gradient that causes flow separation. The adverse pressure gradient increases with the angle of attack, and therefore, the separation location moves towards the leading edge with the increasing angle of attack.

## 2.5. AEROELASTIC CHARACTERIZATION

The membrane kites are tensile structures, mainly made from fabric sheets and lines that cannot resist compression or bending. The materials are stiff and extend only a little with the loading. Under compression, the tensile structures re-orient themselves to a tensile state, which in a non-design condition may lead to a collapse. Because of the tensile design, the membrane kites are lightweight, and they have a much lower mass than the fixed-wing kites. Fixed-wing kites resist bending and compression, and therefore they are built from relatively stiff and heavy materials. The larger surface area per mass of the membrane kites translates to a higher lift per mass, and therefore membrane kites can remain airborne in lighter wind conditions than the fixed-wing kites. Consequently, the membrane kites have the potential to have lower cut-in wind speeds. The disadvantages of the flexible airfoil are the more complex aerodynamics due to the aeroelastic coupling, and the elongation and the durability of the materials.

The flight shape of the membrane wings mainly depends on the layout of the bridle line configuration. The kite is controlled by altering the bridle line system with the two winches in the control pod. The steering winch changes the relative length of the steering lines on the two sides of the wing. This asymmetric actuation leads to the wing yaw and roll. An empirical correlation, called turn rate law, has been established, which couples the actuation of the bridle line system to the turn rate. The turn rate law, in its simplest form, is given by

$$\dot{\Phi} = gU_{\infty}\delta \quad (2.9)$$

where  $\dot{\Phi}$  is the turn rate,  $g$  is an empirical constant and  $\delta$  is the nondimensional steering input. Thus, the turn rate and steering input are linearly proportional. The turn rate law has been validated both experimentally [26–28] and numerically [29].

By alternating the power line setup, the kite wing pitches, which effectively changes the angle of attack and the flexible airfoil adapts itself to the flow. Boer [30] shows that the maximum camber of a sailing airfoil moves towards the leading edge when the angle of attack increases, which both extends the range of practical angles of attack and improves

the maximum glide ratio in comparison to a similar rigid airfoil. Also, the maximum glide ratio occurs with a high lift coefficient, which is beneficial for AWE systems that have to deal with additional tether drag [16].

During the traction phase, the kite is flying either circular or lemniscate crosswind maneuvers. Although the flight path is dynamic, it can be approximated as a transition through steady states if the flight and deformation time scales are substantially higher than the flow time scales. A characteristic flow time scale is the time that a fluid parcel travels from the leading edge to the trailing edge,  $t_f = c/U_\infty$ . The flight time scale depends on the chosen flight trajectory. In the case of a circular trajectory, the actuation changes only between the traction and retraction phases and the time scales are very large. In the case of lemniscate trajectory, the kite is actuated roughly four times when changing between the two circular and two straight paths. The deformation modes depend on the size and the design of the kite. Leuthold [31] studied the different time scales for the TU Delft V3 LEI kite during the traction mode with the lemniscate trajectory. The flow and the flight time scales are around 0.1 s and 20 s, respectively. Leuthold isolated numerous deformation modes during a typical flight without a collapse. The time scales of the global deformation modes are around 0.7 s. Lower time scale deformation modes also occur, such as the trailing edge flutter, but their effect is expected minor due to their local nature. Consequently, the flight and global deformation time scales are substantially higher than the flow time scales and therefore, the steady-state should be a fair assumption. During the retraction phase, the flow time scales are lower, while the deformation modes remain constant. Thus, the steady-state assumption may not hold well during the retraction phase. Additionally, turbulence and wind gusts cause dynamic aerodynamic loading.

Scaling up of the kite power system changes the time scales, but all the scales are expected to increase. The flow parcel time increases because the parcel has to travel a longer distance over the larger wing. A larger wing flies larger trajectories that increases the flight time scale. Moreover, a larger wing has higher inertia which increases the deformation time scales. Therefore, the validity of the steady-state assumption is expected to hold also for the larger wings in the traction phase.

## 2.6. MEMBRANE WING STUDIES

The membrane wings have been studied historically in sailing, kiting and parachuting. More recently, membrane wings have also been used as a lightweight and cheap wing design in several applications such as airplanes [32], hang gliders [33] and wind turbine blades [34]. In those applications, the single membrane is attached to a frame made of stiff material, such as steel, aluminum or carbon fiber. The development of fully flexible membrane wings started from parachutes, which evolved into modern steerable ram-air parachutes [35]. The applications of parachutes vary from recreation to transport to military use. Later on, the parachutes evolved into paragliders that could ascend using thermals or upward-directed wind by obstacles such as hills. Kite surfing started with ram-air kites, but the breakthrough design was the LEI kite. The pre-inflated tubes floated the kite and allowed to relaunch it from the water easily. The recent innovation in membrane wings is the single-skin design used as a very low-weight design in kite surfing and paragliding. The membrane wings enabled these applications due to their

beneficial properties of lightweight, compactness and safety.

Ram-air parachutes have been extensively studied experimentally, traditionally by drop tests, but full-scale wind tunnel tests also have a relatively long history [36, 37]. The wind tunnel experiments on the membrane wing designs are challenging because the thin canopy cannot be scaled down easily. Experimental studies for single and double skin sailing models are available at moderate Reynolds numbers [16, 30, 38]. The sailing models have a stiff bar at the leading edge and the sail is wrapped around it and the trailing edge is fixed to a little plate that rotates in the local membrane direction. More recently, field tests have also been performed for AWE kites. One option is to use tow tests, for which the wing is tethered to a moving vehicle, to measure both static flight performance and dynamic flight history [39–42]. However, this testing method is limited in terms of maximum traction force. There are also measurement uncertainties due to wind variations and limitations in measuring lift-to-drag ratios for dynamic maneuvers [43].

Alternatively, onboard sensors can measure the flow past the wing in situ. Oehler and Schmehl [44] mounted a pitot tube and wind vanes to measure the relative wind velocity on the TU Delft V3 kite. Together with the tether tension measured at the ground station, they derived the angle of attack and the aerodynamic coefficients from the measurements. The work was preceded by Roulier [28] who increased the number of measured samples and used a different model to derive the aerodynamic coefficients from the measurements. The lift coefficient of the two models agrees very well, although it shows suspiciously low sensitivity on the angle of attack in both cases. The drag coefficient showed a similar trend, but the magnitude is approximately two times higher in work by Roulier than in work by Oehler and Schmehl.

Numerical studies can be classified into two categories: inviscid and viscous methods. The inviscid methods are usually based on potential flow theory, and they are fast but require ad-hoc modeling. The viscous methods are based on solving the Navier-Stokes equations numerically on a three-dimensional grid. In the typical flight conditions, the equations are prohibitively expensive to resolve down to the smallest scales of the turbulent eddies, and therefore a turbulence model is required. A common approach is the Reynolds-averaged Navier-Stokes (RANS) approach, in which the mean flow is resolved, and the turbulence is modeled. An additional overhead compared to the inviscid methods is the generation of the volumetric grid that follows the unconventional shape of the membrane wings with nearly zero-thickness surfaces with bumps and sharp angles.

The past studies are mainly based on inviscid methods with viscous corrections. Breukels [14] developed a multibody model for membrane kites with inflatable tubes. The computational model is built from rigid one-dimensional wires, and the flexibility is taken into account with deformable joints. The wing is divided into chordwise sections, and the section forces are determined from airfoil data that depend on the local angle of attack, section camber and section thickness. The airfoil data are calculated with two-dimensional RANS simulations. The three-dimensional forces are calculated with the lifting line theory. Bosch [29] increased the fidelity of the model by Breukels by using a finite element method instead of the rigid multibody model for the wing. The canopy is modeled with shell elements, and the inflatable beams are modeled with beam elements for the inflatable tubes. The model shows an imbalance between the fidelity

of aerodynamics and structural mechanics. The FE model is computationally more expensive and presumably more accurate than the aerodynamic model. Leloup [45] also developed an aeroelastic model for LEI kites based on the lifting line method and an FE model with shell and beam elements. Duport [46] balanced the fidelity of the models by using only beams in the structural model and by adding a nonlinear extension to the lifting line model that accounted for part of the nonlinear regime of the lift coefficient versus angle of attack. Both the aerodynamic and the structural models were compared to a higher fidelity model. The lifting line model was compared with a RANS simulation on a typical membrane kite wing planform with a NACA airfoil. The aerodynamic model agrees well with low angles of attack but disagrees increasingly with higher angles of attack. The beam model was compared to a shell element model. The two models showed a significant disagreement, and Duport concludes that the beam model requires further calibration. Gaunaa et al. [47] present an efficient method for determining the aerodynamics of an elliptic and high anhedral wing planform with NACA airfoil by using the vortex lattice method coupled with 2D airfoil data to take into account the effects of airfoil thickness and fluid viscosity. The method achieved good agreement with a 3D RANS simulation, especially for the attached flow.

As expected with the inviscid methods, the correlation worsens as the flow undergoes severe separation, and the separation is specifically prominent for high-lift conditions such as traction kites in AWE systems. Leuthold [31] aimed to overcome this by developing a quasi-steady multiple wake vortex lattice method that she used to investigate the aerodynamics of the TU Delft V2 LEI kite wing. In addition to the standard bound vortex lattice, the model shed vortex lattices at known separation locations. The results were compared with steady-state RANS results by Deaves [48]. With a careful selection of parameters, the lift and drag coefficients differed by approximately 10%. Another limitation of the inviscid models is the ad-hoc modeling which requires a priori knowledge of the flow to take the viscous effects into account. Reliable aerodynamic data for unconventional wings such as the membrane kites is sparsely available, even for the two-dimensional LEI kite airfoil.

In light of the limitations of inviscid methods, CFD models with the RANS turbulence model have also been used. De Wachter [22] measured the aerodynamic forces and the flight shape of the ram-air surf kite and simulated the aerodynamics around the deformed wing with the RANS model. The simulations under-predicted both the lift and the drag forces by around 10% and 30%, respectively. Fogel [19] simulated the steady-state aeroelasticity of a single ram-air cell with a RANS solver coupled to a membrane FE model. The results were compared with the experiment by Ware and Hasell [36]. The study was extended to a straight wing with multiple cells [49]. Both numerical simulations showed moderate agreement with the experiments.

Piquee et al. [50] investigated the aeroelasticity of a tapered membrane wing both computationally and experimentally. The wing has a rigid leading and trailing edge and two highly elastic membrane skins. The computational framework couples a RANS solver with a membrane FE solver. While their model has time integration with unsteady RANS and dynamic FE, they use a high time step that prevents undesired unsteadiness. The agreement between the experiment and simulations was good. Thus, their study shows that by carefully designing the experimental and numerical setups, the

RANS model coupled with a membrane solver can accurately predict the aerodynamics of a membrane wing. RANS has also been used to study aerodynamics around the rigid shape of the TU Delft LEI kite models [48, 51]. The follow-up work [25, 52] compared simulation results to the experimental data obtained by Oehler and Schmehl [44] and Roullier [28]. The numerical simulations showed the well-known strong dependency of lift coefficient on the angle of attack, which was not captured in the experiments as mentioned earlier. Also, the drag coefficient in the simulations was remarkably lower than in the in-situ experiments.

In conclusion, the flow around membrane kites encounters constant flow separation, a viscous phenomenon. Therefore, the inviscid aerodynamic models require viscous corrections that are problem-dependent and require a priori knowledge of the flow. Unfortunately, reliable data on the kite wing aerodynamics are scarcely available. Therefore, the more physics-based viscous methods are more promising at present. These viscous methods are more computationally intense, especially at realistic Reynolds numbers. The RANS approach is widely used to overcome the computational expense, which resolves the mean flow field and models the turbulence. The RANS approach uses the entire three-dimensional shape of the wing, and a good choice for modeling the membrane structure is, therefore, a zero-thickness shell model. Since the RANS results in steady-state forces, an efficient static structural mechanics model is preferred. The models should be validated with the experiments that are currently available.

## 2.7. RESEARCH GOALS

The key research goals of this thesis are as follows:

1. **Develop a methodology to simulate the steady-state of an aeroelastically deformed membrane kite.**

The aim is further to bridge the gap between low-fidelity and high-fidelity aeroelastic models. The starting point is the viscous models based on resolving Navier-Stokes equations and shell FEM, but the computational expense is reduced by simplifications such as assuming the steady-state flow. The validity of the assumptions is assessed, but the focus is also on the robustness of the methodology. The method should be applicable to be integrated into the kite design process. For instance, an automated workflow for the mesh generation is required, and the mesh deformation should be robust during the coupled simulations.

2. **Use the methodology to improve the understanding of the aerodynamic loads on membrane kites used in AWEs**

The developed framework is used to study the characteristic flows governing the membrane kite flight. The membrane kites are very flexible, and therefore their flight shape differs from the initial design shape. The deformation effect on the aerodynamics is isolated by comparing the flexible shape to the rigid shape.

## 2.8. RESEARCH QUESTIONS

Based on the research goals, the following research questions arise:

**Model assumptions**

1. How much can we simplify high-fidelity aeroelastic model for the membrane kites without sacrificing too much their accuracy?
2. What is the optimal balance of fidelity between the aerodynamic and the structure model for membrane kites?

**Model robustness**

1. Is it possible to build a robust aeroelastic model for membrane kites that can be used as a part of the kite design process?
2. Can time-consuming CFD volume mesh generation around the membrane wing be automated?
3. Is there a robust way to deform the computational mesh around the highly flexible membrane kite?

**Physics**

1. What kind of flow phenomena are observed around wing planforms of the membrane kites, and how do they affect the practical use of kites in AWE?
2. How does the flexible structure of membrane kites affect the aerodynamic efficiency?
3. Can a steady-state model capture the recirculation zone and the flow separation around the non-smooth wing surface of a membrane kite?

# 3

## COMPONENTS OF A STEADY-STATE AEROELASTICITY MEMBRANE KITE MODEL

The steady-state aeroelasticity model is presented that comprises two solvers that are coupled in a partitioned manner with preCICE. The flow around the wing is solved by using CFD with RANS based turbulence model. The structural deformation is calculated with a finite element (FE) solver based on dynamic relaxation. The models are developed in this chapter.

### 3.1. AERODYNAMICS AND TURBULENCE MODELING

The simulations presented are based on the OpenFOAM toolbox developed by ESI [53]. OpenFOAM is an open-source CFD library written in C++ and has a high-level programming interface to solve partial differential equations. The Navier-Stokes equations are discretized on a polyhedral mesh using a cell-centered finite volume method. Several solvers and turbulence models are prepackaged in the default distribution. The aerodynamics considered in this work are low Mach number flows, and therefore the fluid can be assumed incompressible. Additionally, the flow is assumed to be steady-state because of the RANS turbulence modeling approach and computational efficiency.

One of the main uncertainties in CFD and aerodynamic modeling is turbulence modeling, which is required for flows at high Reynolds numbers. The most common approach is the use of RANS equations, in which the transport equations are solved only for the mean flow field, and a turbulence model represents the turbulent fluctuations. The RANS equations for the steady-state incompressible fluid are given by

$$\frac{\partial U_i}{\partial x_i} = 0, \tag{3.1}$$

$$U_j \frac{\partial U_i}{\partial x_j} = -\frac{1}{\rho} \frac{\partial P}{\partial x_i} + \nu \frac{\partial^2 U_i}{\partial x_j^2} - \frac{\partial \overline{u'_i u'_j}}{\partial x_j}, \quad (3.2)$$

where  $\overline{U_i}$  and  $P$  are the mean velocity in the  $i$  direction and pressure, respectively. The term  $\overline{u'_i u'_j}$  is the Reynolds stress term that represents the effect of the turbulent velocity fluctuations and which has to be modeled. Many RANS turbulence models have been developed for different applications, but none of them works universally for all types of flows. Thus, it is crucial to critically assess the suitability of a specific model for each application case.

The most widely used RANS-based turbulence models employ two transport equations for turbulence properties, generally one for the turbulence kinetic energy  $k$  and another one for the turbulence length or time scale. Popular for engineering applications is the shear stress transport (SST) model by Menter [54], which combines the  $k - \epsilon$  model by Jones and Launder [55] and the  $k - \omega$  model by Wilcox [56] to get the best of the two models. OpenFOAM uses a revised version of the SST model [57] with the turbulence specific dissipation rate production term formulated by Menter and Esch [58]. The term is limited similarly as in the transport equation for the turbulence kinetic energy, as described on the NASA webpages [59].

Common turbulence models such as SST cannot describe the transition from laminar to turbulent flow and assume that boundary layers are always turbulent. A similar effect can be achieved experimentally by tripping the boundary layer close to the leading edge, leading to a nearly immediate transition to the turbulent boundary layer. However, the effect of laminar-turbulent transition is important in many conventional aerodynamic flows over smooth surfaces and with a low level of turbulence.

### 3.2. TRANSITION MODEL

Boundary layer transition is a challenging topic that has been extensively studied. Three primary modes of laminar-turbulent transition are considered [60]

1. *Natural transition*: Perturbations from the exterior flow, such as turbulence, propagate into the boundary layer. The perturbations grow through Tollmien-Schlichting waves and turbulent spots. And eventually, the boundary layer becomes turbulent. In external aerodynamic flows around smooth surfaces, this is the usual mode of transition.
2. *Bypass transition*: Either the freestream disturbances are high (high turbulence intensity) and propagate directly into the boundary layer, or the surface is rough. Consequently, the turbulence is directly transported to the boundary layer, which triggers the transition. For example, the deforming membrane or the woven material of the kite may induce disturbances which trigger transition.
3. *Separation induced transition*: A laminar boundary layer cannot withstand much adverse pressure gradient, and therefore it separates relatively easily. Flow separation induces disturbances and transitions quickly. The turbulence enhances mixing, and therefore the formed turbulent shear layer may reattach again. The size

of separation bubbles varies heavily, and long laminar separation bubbles may affect the performance significantly. The laminar separation bubbles are observed around the airfoils with rather low Reynolds numbers.

For a more comprehensive review of the boundary layer transition, the reader is referred to literature [61, 62].

The presence of different transition modes is one reason for the complexity of modeling transition, especially within the RANS framework, because the transport equations are only resolved for the mean flow field and therefore do not contain intrinsic information on the disturbances. Moreover, common transition models rely on integral boundary layer values to predict transition, which is costly to compute on arbitrary unstructured meshes. The transition also does not have a clear definition in three dimensions. Therefore, general-purpose transition models for RANS simulations have not been available until recently. In particular, Langtry and Menter[63] developed the  $\gamma - \tilde{Re}_{\theta t}$  transition model on top of the SST turbulence model, but it has also been coupled with other turbulence models such as Spalart-Allmaras [64]. The transition model does not try to capture the actual physics of the transition but is based on empirical correlations. It has been successfully employed for several external aerodynamic problems such as flow around airfoils and turbine blades[60], as well as around a cylinder[65].

In Langtry and Menter's model, two additional transport equations are used to model the transition. The transported quantities are the intermittency  $\gamma$  and the transition momentum thickness Reynolds number  $\tilde{Re}_{\theta t}$ . The intermittency controls the transition by scaling the production and destruction terms of the turbulence kinetic energy  $k$  in SST (or another) turbulence model. The transition momentum thickness Reynolds number  $\tilde{Re}_{\theta t}$  is required to transport non-local freestream effects into the boundary layer. The Reynolds number  $\tilde{Re}_{\theta t}$  is connected to intermittency through empirical correlations and  $\tilde{Re}_{\theta t}$  itself depends on empirical correlations of turbulence intensity and streamwise pressure gradient.

### 3.3. MESH GENERATION

The mesh generation is often the most labor-intensive and challenging part of CFD simulations. A high-quality mesh is a prerequisite, as a low-quality mesh might compromise the subsequent steps of the simulation. A low-quality mesh may cause the CFD solver to converge slowly, not converge at all or diverge. Additionally, even if the solver converges, the solution may be inaccurate. The quality of the mesh can be viewed from two perspectives. On the one hand, it has to be refined enough to capture the relevant flow physics. On the other hand, the grid metrics, such as the mesh orthogonality and skewness, affect the discretization error and convergence behavior. The required mesh density is unknown prior to the simulation because it depends on the flow. Therefore, a mesh convergence study is usually needed to ensure that the results do not change significantly when refining the mesh. In Chapters 4 and 5 such a study is presented. One important parameter for the diagnosis of mesh quality is the dimensionless wall distance  $y^+ = u_* y / \nu$  where  $u_* = \sqrt{\tau_w / \rho}$  is the shear velocity and  $y$  is the distance to the wall. The dimensionless wall distance should be less than unity for wall-resolved boundary layers. For high Reynolds number flows such as in the present work, the wall-normal spacing is

in the order of  $10^{-6}$  chord lengths, and therefore, the mesh in the wall direction has to be highly stretched for acceptable computational costs. Generally, if the flow has a well-defined direction, as in boundary layers, quadrangles (2D) and hexahedra (3D) aligned with the flow are preferred to minimize the numerical dissipation and reduce the cell count.

The mesh generation algorithms vary from the user-demanding structured mesh algorithms to highly-automated unstructured algorithms. Structured mesh generation is highly problem-dependent and requires a lot of user time and knowledge to set up. However, the algorithms are relatively simple, and therefore, the computational time to generate the mesh is small. For instance, in multi-block structured mesh generation, the user decomposes the fluid domain manually into blocks and defines the grid resolution at each edge of the blocks. The structured algorithm calculates the interior points of the blocks with an interpolation, such as transfinite interpolation. By contrast, the unstructured algorithms require a more abstract definition of the mesh, such as merely defining the boundaries of the fluid domain. However, the algorithms required to generate unstructured meshes are computationally more intense. A common practice is to combine the two methods and use structured algorithm near the bodies to capture the steep velocity gradients in the boundary layers accurately and efficiently, and use an unstructured algorithm elsewhere.

A convenient way to generate the near body boundary layer mesh is to extrude it from a surface mesh. The extruded mesh naturally aligns with the boundary layer flow and gives excellent control for the important wall-normal spacing. Moreover, extrusion reduces the complexity of the mesh generation by one order. The user has only to design the surface mesh instead of the volume mesh. The surface mesh can be extruded up to the exterior boundary of the domain. However, as mentioned above, the structured boundary layer mesh is usually combined with an unstructured tetrahedral mesh for the rest of the domain.

### 3.4. STRUCTURAL MECHANICS

The structural simulations are based on the mem4py solver [66]. Mem4py is an open-source FE library written in Python programming language for tensile structures such as membranes and cables. Similarly to the aerodynamic model, only the steady-state structural mechanics are considered, and therefore the dynamic relaxation (DR) method is used for the form-finding. The dynamic relaxation method [67] uses the dynamic equations of motion to find the static shape by damping the dynamic terms. Only the final state of the system is of interest, and therefore the damping terms are fictitious and chosen to reach the static equilibrium as fast as possible. The equations are given by

$$M\ddot{u} = R - C\dot{u} \quad (3.3)$$

where  $M$  is the mass,  $\ddot{u}$  is the acceleration,  $\dot{u}$  is the velocity,  $R = f_e - f_i$  is the residual force between the external and internal forces, while  $C$  is the viscous damping. Mem4py uses kinetic dynamic relaxation, which traces the peak kinetic energy of an undamped system, while the viscous damping  $C$  is omitted. When the peak is detected, the nodal velocities are set to zero, and the process is repeated until most of the kinetic energy

has been dissipated. The advantage of using DR is its explicit nature, which is robust for highly nonlinear problems such as the present fabric membranes that easily wrinkle (buckle). Additionally, static methods usually require incremental loading techniques for non-linear problems. Dynamic relaxation may permit the use of full load directly or at least much larger load increments. Thus, DR is usually a faster, less memory intensive and more robust method for finding the static equilibrium than the implicit static methods or other dynamic methods [68].

The kite membranes are made of thin woven fabric that cannot resist any compression or bending. Under bending and compression, the membranes buckle almost immediately and form wrinkles. The wrinkles consist of tiny length scales, and therefore, their resolution requires a very fine mesh. For engineering applications, the interest is usually not in the exact shape of the wrinkles, but it is sufficient if the average influence of the wrinkles can be predicted. Consequently, simplified wrinkling models have been developed. The model is enabled in the elements with compressive stresses to result in an average smooth surface. The wrinkling model is usually used together with membrane elements without rotational degrees of freedom. Consequently, a coarser computational mesh with fewer degrees of freedom can be used, which reduces the computational expense. Additionally, the smooth shape eases the mesh deformation for the fluid mesh in the aeroelastic simulations.

### 3.5. AEROELASTIC COUPLING

The two solvers, OpenFOAM and mem4py, are coupled for the steady-state aeroelasticity simulations. At the interface between the two solvers, the preCICE [69] coupling tool is used. PreCICE uses a partitioned and non-intrusive approach to couple the codes and does not necessarily require any modifications to the solvers. Instead, a small independent piece of code is required for each solver to interface with preCICE. These so-called adapters are executed simultaneously to begin the partitioned multiphysics simulation. Another advantage of the non-intrusive approach is that the adapters can be developed in any of the most common scientific programming languages (e.g. Python, C++ and Fortran), and they can be executed in serial or parallel. After the adapters have been implemented, the coupling settings can be easily changed in a preCICE markup file. The most important settings are:

1. The solvers and exchanged data

PreCICE supports an arbitrary number of solvers, and each solver can have several meshes. The solvers, meshes and exchanged data are introduced by giving them a name as an identifier referred to in the adapter.

2. Mapping of the data

Often the mesh requirements for different physics are different, and therefore the meshes at the interface are not conforming. Consequently, the exchanged quantities must be mapped from one mesh to the other. PreCICE comes with three mapping algorithms: nearest neighbor, nearest projection and radial basis function. Each of the mapping algorithms comes with a conservative and consistent variant. Conservative mapping is typically used for integral quantities, such as forces,

to retain the total force acting on the interface. Consistent mapping is used for normalized quantities, such as pressure, and the quantities are mapped exactly.

### 3. Coupling algorithm

A coupling scheme can enhance the convergence of the partitioned simulation. PreCICE has three coupling schemes: constant under-relaxation, adaptive under-relaxation (Aitken) and several quasi-Newton variants. The scheme modifies the exchanged quantities to stabilize the solution process and to accelerate the convergence.

In fluid-structure interaction simulations such as aeroelastic simulations, the structure is moving and deforming. Therefore the volumetric fluid mesh around the body in CFD has to be altered to follow the new shape. Generally, there are two approaches: either generating a new mesh or deforming the old mesh to match the new shape. The latter mesh deformation methods propagate the displacements from the deforming structure to the volumetric mesh. Common methods to calculate the mesh deformation for the unstructured meshes are based on solving a partial differential equation on the mesh, such as the Laplacian for the displacement

$$\nabla \cdot (D \nabla u_i) = 0 \quad (3.4)$$

where  $D$  is the diffusivity coefficient, and  $u$  is the displacement. Choosing an appropriate diffusivity coefficient is problem-dependent. Usually, the coefficient is non-constant, and it depends on the distance to the moving boundary [70].

Another way to deform the mesh is by using the radial basis function (RBF). The RBF based mesh deformation methods do not use the connectivity of the mesh but they are based on point-to-point interpolation. The interpolation function is given by

$$S = \sum_{i=1}^N w_i \phi(r) \quad (3.5)$$

where  $N$  is the number of boundary points,  $w_i$  are the weighing coefficients,  $\phi$  is the radial basis function with respect to the Euclidean distance  $r = \|X - X_{b_i}\|$ . The distance is calculated between the nodal points  $X$  of the mesh and known deformed boundary mesh points  $X_{b_i}$ . Some of the common radial basis functions are Gaussian, thin plate spline and multi-quadric, i.e.

$$\phi(r) = e^{-\epsilon r^2} \quad (3.6)$$

$$\phi(r) = r^2 \ln r \quad (3.7)$$

$$\phi(r) = \sqrt{1 + (\epsilon r)^2} \quad (3.8)$$

where  $\epsilon$  is the shape parameter. The weighing coefficients are determined from the condition

$$S(X_{b_i}) = \Delta X_{b_i} \quad (3.9)$$

where the  $\Delta X_{b_i}$  are the known boundary point displacements. RBF mesh deformation is a robust method that preserves the mesh quality and the boundary layer refinements. However, for practical three-dimensional problems, the basic RBF is computationally too expensive because the costs scale cubically with size and the memory requirement quadratically to the number of boundary points. [71] Consequently, several

methods have been developed to select only a subset of the boundary points. Rendall and Allen [72] proposed a method based on greedy algorithm to create a subset of control points. The greedy algorithm iteratively finds an optimal subset of points that interpolates the full set of points and reduces the computational cost remarkably without losing accuracy [72]. RBF with the greedy algorithm mesh deformation is robust, preserves the mesh quality, and is computationally efficient.

### 3.6. PRESENT COMPUTATIONAL SETUP

OpenFOAM's pimpleFoam solver is used to simulate the aerodynamics of the membrane kite. PimpleFoam is an incompressible solver designed for transient flows with large time steps. The transient solver is used because it supports moving meshes, unlike the steady-state solver. In the present steady-state simulations, the time integration is disabled, and the solver runs only for one time step. Within the time-step, the solver uses the SIMPLE algorithm until convergence is reached. Second-order schemes are used for all the other derivatives besides for the advection of the turbulence quantities, which are discretized with first-order upwind scheme. The boundary conditions are as follows:

- Wing surface

No-slip condition without wall function is enforced. The turbulence quantities are set to zero besides for  $\omega$  which approaches infinity at the wall. For  $\omega$ , Menter [54] recommends using following condition

$$\omega_{wall} = \frac{6\nu}{\beta_1 y^2}, \quad (3.10)$$

where  $\beta_1 = 0.075$ . Pressure is set to zero-gradient at the wall.

- Far-field

A mixed boundary condition is applied depending on whether the flow enters or leaves the computational domain. For inflow, uniform values are imposed for the velocity and the turbulence quantities, while the pressure gradient is set to zero. Uniform pressure is imposed for outflow, while the gradients of velocity and turbulence quantities are set to zero. The inlet values for the turbulence quantities are calculated from the exterior flow velocity ( $U_\infty$ ), the turbulence intensity (Tu) and the eddy viscosity ratio ( $\nu_t/\nu$ ). The inlet boundary condition for  $\gamma$  is unity and the other turbulence quantities are estimated as

$$k = \frac{3}{2} \left( U_\infty \frac{Tu}{100} \right)^2, \quad (3.11)$$

$$\omega = \frac{k}{\nu} \left( \frac{\nu_t}{\nu} \right)^{-1}, \quad (3.12)$$

and for  $\tilde{Re}_{\theta t}$  with zero acceleration in streamwise direction [63]

$$\begin{aligned} \tilde{Re}_{\theta t} &= 1173.51 - 589.428 Tu + \frac{0.2196}{Tu^2}, & Tu \leq 1.3, \\ \tilde{Re}_{\theta t} &= 331.5(Tu - 0.5658)^{-0.671}, & Tu > 1.3, \end{aligned} \quad (3.13)$$

where  $Tu$  is the turbulence intensity in percentages.



Figure 3.1: LEI kite airfoil. Original airfoil (red), filled-in airfoil with thickness (black contour with gray fill).

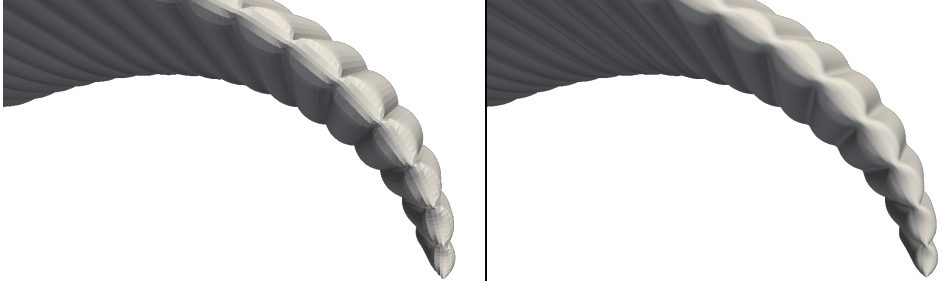


Figure 3.2: Pre-inflated ram-air kite wingtip. The pre-inflated shape calculated by mem4py (left), the pre-inflated shape mapped on the fluid mesh with elliptic smoothing (right).

- Symmetry  
The simulations without side-slip are symmetric in the middle of the wing. All the gradients are set to zero on the symmetry plane.
- Front and back faces in the two-dimensional simulations  
OpenFOAM works only with three-dimensional meshes, and therefore even in two-dimensional simulations, the mesh has a thickness of one cell. An empty boundary condition is applied on the extruded planes to disable the solution calculation in the third dimension.

The two kite wings to be investigated in this work are LEI and ram-air. They both require geometrical simplifications before the CFD mesh generation. Acute angles are formed between the inflatable tubes and the membrane for LEI kites and at the rib locations for inflated ram-air kites. Extruding the mesh on these sharp corners leads to an immediate self-intersection. Therefore, the corners are partially filled-in before the volume mesh generation as shown in Figure 3.1 and 3.2. The CFD mesh is generated for the inflated shape of the ram-air kite. Consequently, the structural solver firstly calculates the inflated shape, and the surface is deformed accordingly. The sharp corners are smoothed slightly with elliptic smoothing (Figure 3.2, right).

For wings, the mesh is usually generated by lofting through the (filled-in) airfoils. The wingtip requires additional treatment. The last cross-section of a ram-air kite is usually simply a line segment. In the present work, a small, one element thickness is given for the last section, and the upper and lower skins have the same cell count. The mesh sim-

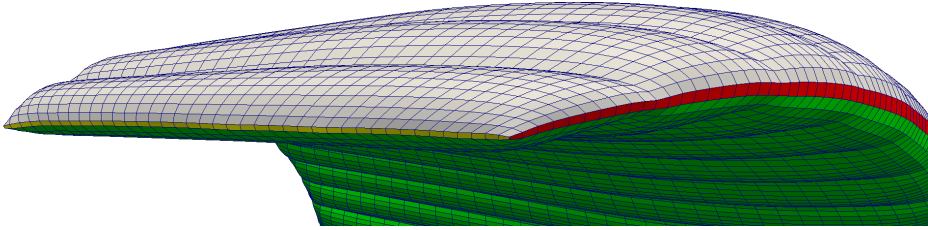


Figure 3.3: Ram-air kite wingtip with structured algorithm. The colors indicate the different blocks of the structured mesh.

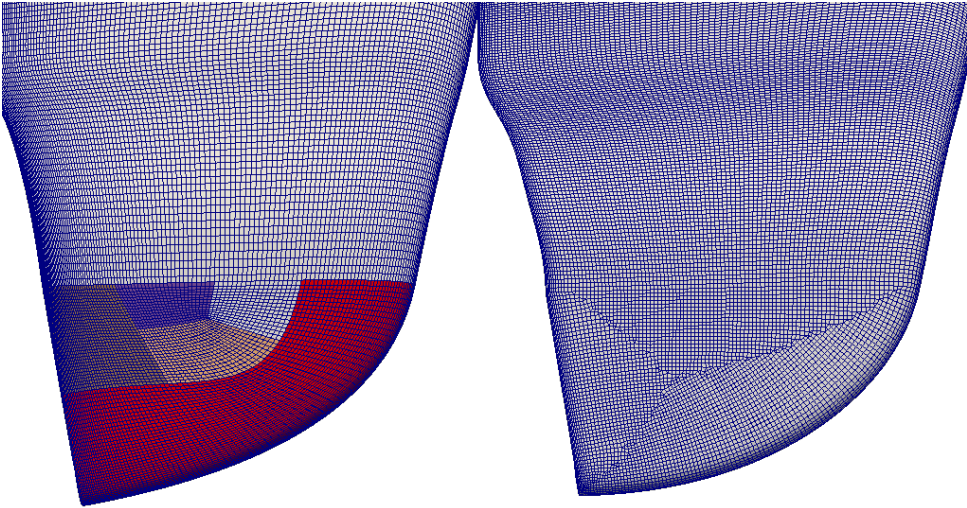


Figure 3.4: LEI kite wingtip with structured (left) and unstructured (right) algorithm. The colors indicate the different blocks of the structured mesh.

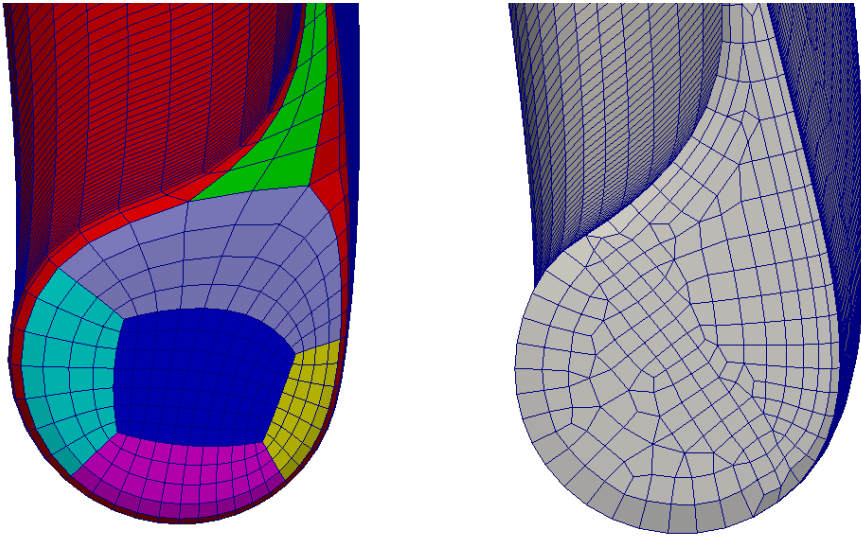


Figure 3.5: The leading edge of LEI kite wingtip with structured (left) and unstructured (right) algorithm. The colors indicate the different blocks of the structured mesh.

ply goes around wingtip (Figure 3.3). In the case of an LEI kite, the leading edge tube sweeps around the wingtip to the trailing edge. Figure 3.4 shows the structured (left) and unstructured (right) surface meshes of the TU Delft V3 LEI kite. The structured mesh is divided into several blocks. The leading edge is swept around the wingtip (red color) to the trailing edge, and the gap between the last airfoil and the sweep is filled with a few additional blocks. The trailing edge also requires additional handling (Figure 3.5). The tube end forms a circle, and therefore an o-grid topology is used. The structured surface mesh is extruded with the hyperbolic grid generation scheme [73]. In Chapter 4 and Chapter 7, a two-dimensional and three-dimensional structured mesh is presented, respectively. The unstructured mesh is generated with the T-REX algorithm of commercial Pointwise software [74] and the mesh is presented in more detail in Chapter 5.

Once a suitable mesh topology for the structured mesh is found, the mesh distribution is fast and easy to change. Also, the underlying geometry can be altered as long as the topology of the wing remains the same. A fully structured mesh topology for the ram-air kite and LEI kite wing without struts is found in this work. The unstructured mesh generation requires less expert knowledge and allows generating meshes for more complicated geometries than the structured mesh generation. The structured algorithms initially require much more time and experience to set up. However, once a good blocking topology is found, the mesh is fast to generate, the user has good control of the mesh resolution, and the resulting meshes are of high quality.

The Laplacian-based mesh deformation that comes with OpenFOAM is initially used in the aeroelastic simulations in Chapter 7. The simulations crashed because the mesh deformation resulted in inverted cells. The inverted cells were consistently near the trailing edge with high aspect-ratio cells and large deformations. Consequently, another

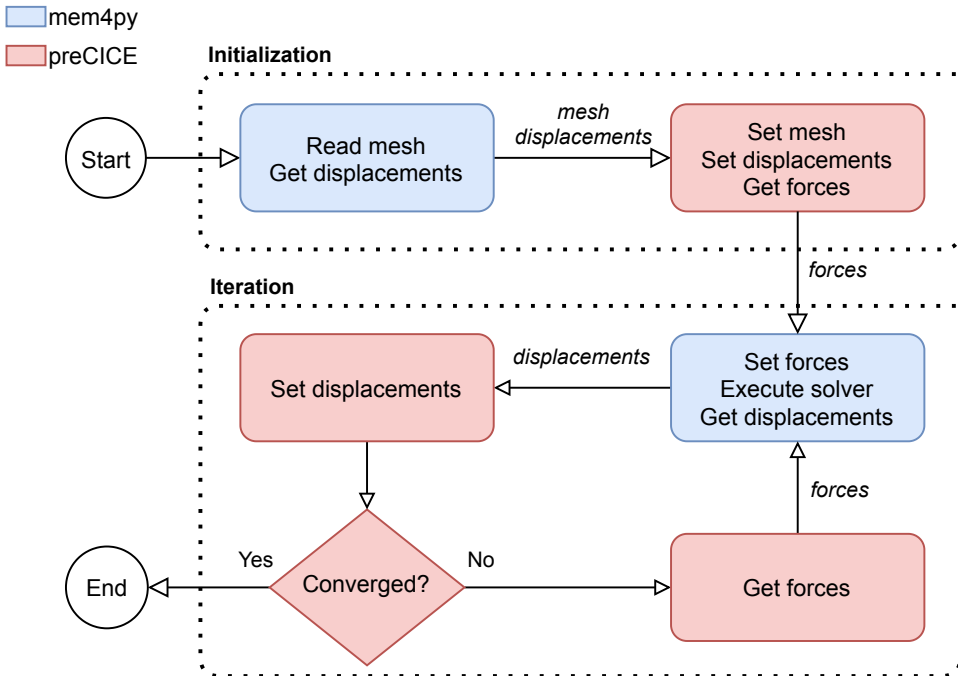


Figure 3.6: Diagram showing the main actions of the mem4py adapter that couples mem4py and preCICE.

more robust method had to be found. The RBF mesh deformation library included in the FOAM-FSI package [75] was modified to work with OpenFOAM [76]. The library uses greedy algorithm for selecting a subset of the surface nodes that increases the computational efficiency.

The structural deformation is calculated with the FE solver mem4py with the kinetic dynamic relaxation method. The FE model consists of triangular membrane elements with Jarasjarungkiat wrinkling model [77] and two-node cable elements for the bridge line system and the tether. The material model for the membrane and the cable elements is isotropic linear elastic.

A preCICE adapter already exists for OpenFOAM [78], and it is used in the present work. The preCICE adapter for the mem4py solver is implemented in Python. The main functionality of the adapter is described in Figure 3.6. The blue color indicates the mem4py actions, and the red color indicates preCICE actions. The code of the adapter starts by importing mem4py and preCICE interfaces. During the initialization, mem4py reads the FE model and passes the interface mesh and the initial displacements to preCICE. PreCICE gets the initial forces from the OpenFOAM adapter and passes them to mem4py. During the iteration, mem4py calculates the displacements from the forces and passes them to preCICE and preCICE checks if the coupled simulation has converged. If not, preCICE reads new forces from the OpenFOAM adapter and passes them to mem4py. The iteration continues until convergence is reached. The adapter is less

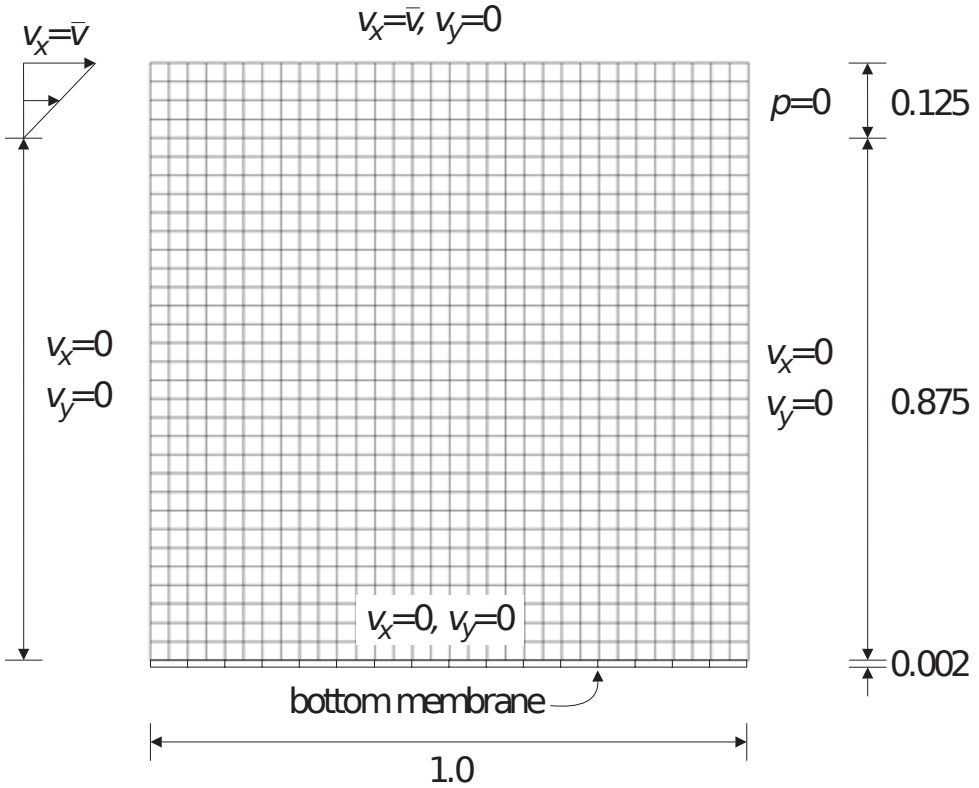


Figure 3.7: Cavity with membrane bottom. [79]

than 100 lines of Python code.

### 3.7. VERIFICATION: CAVITY WITH MEMBRANE BOTTOM

The coupled solver is verified by simulating a cavity flow with a membrane, shown in Figure 3.7. The traditional cavity flow has three fixed walls and a top wall, moving with a constant velocity. In this modified problem, the bottom wall is made of a membrane, and the top wall velocity fluctuates sinusoidally  $\bar{v} = 1 - \cos(2\pi t/5)$ . Also, the problem contains a small inflow and outflow at the top of the side walls. The velocity at the inlet increases linearly from zero to the top wall velocity. The fluid viscosity is  $\nu = 0.01 \text{ m}^2/\text{s}$  and the density is  $\rho = 1 \text{ kg}/\text{m}^3$ . Consequently, the Reynolds number is low, and the flow is laminar; therefore, no turbulence model is used. The initial condition for the velocity and the pressure is zero. The fluid mesh has isotropic hexahedral distribution with  $32 \times 32 \times 1$  cells. The nodes of the membrane mesh match the fluid mesh, and consequently, it has 32 quadrangles split into 64 triangles. The properties of the membrane are the following: Young's modulus  $E = 250 \text{ Pa}$ , Poisson's ratio  $\nu = 0$ , density  $\rho_s = 500 \text{ kg}/\text{m}^3$  and thickness  $t = 0.002 \text{ m}$ . The time-step of both the structure and the fluid solver is  $\Delta t = 0.01$  and the simulation is carried for  $t = 70 \text{ s}$ . The RBF mesh deformation is used.

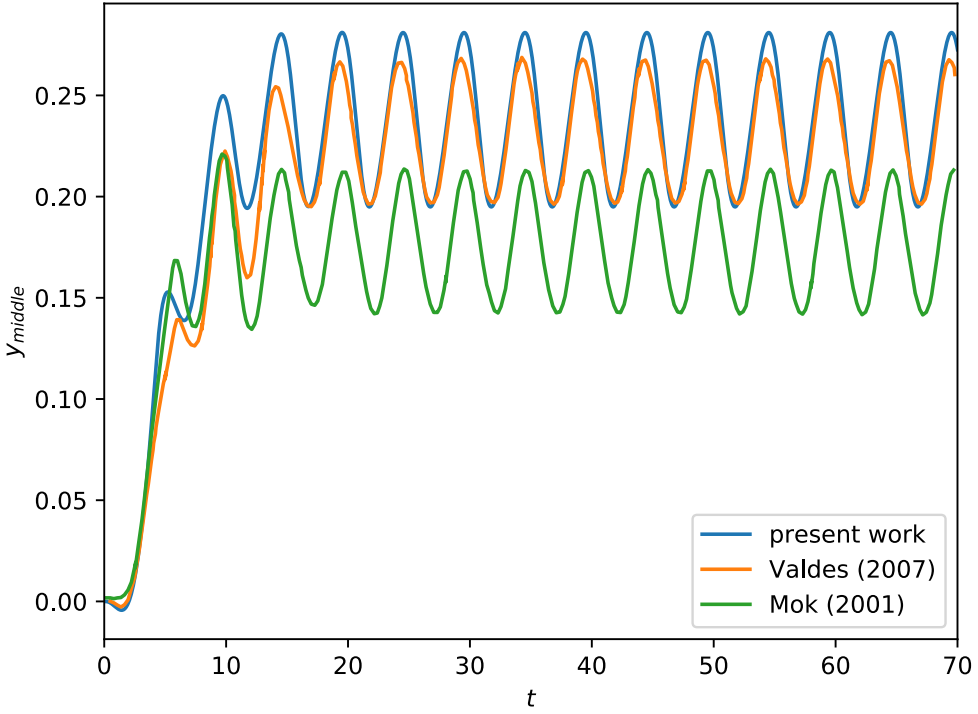


Figure 3.8: The middle node displacement of the membrane.

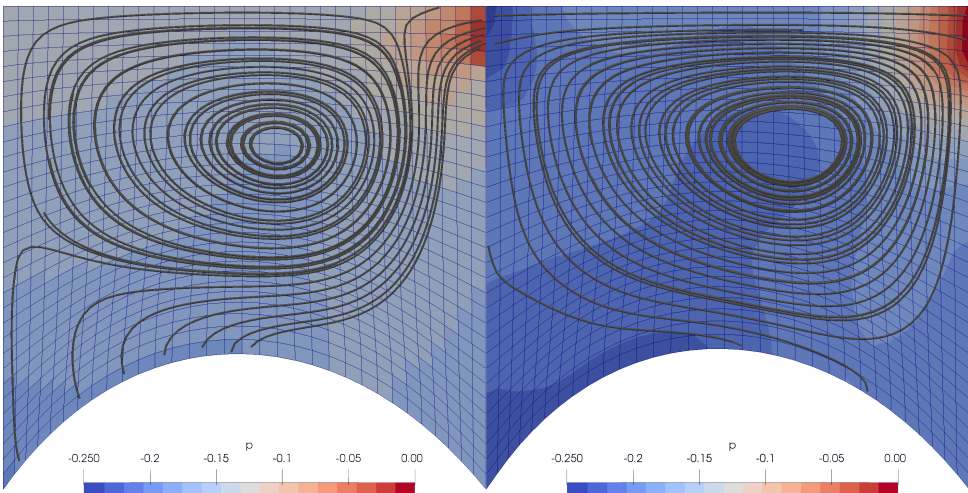


Figure 3.9: Mesh deformation, streamlines and pressure contour at  $t = 15$  s (left) and  $t = 17.5$  s (right).

Although this test case has transient boundary conditions and requires a transient solver, it can be used to verify parts of the coupled simulation framework, such as the aeroelastic coupling and the mesh deformation. Figure 3.8 shows the middle node displacement of the present work and the results of Valdes [79] and Mok [80]. The oscillating inflow leads to oscillatory motion for the membrane. The displacement reaches steady oscillations after approximately three periods ( $t = 15$  s). The results agree well with the work by Valdes, who used similar boundary conditions to the present work. Figure 3.9 visualizes the flow at the lowest and highest inflow velocity. In conclusion, the mem4py for preCICE adapter works as intended. The forces and displacements are exchanged correctly between the two solvers, and the two solvers converge at each time step. Moreover, the deforming mesh maintains high quality.

### 3.8. CONCLUSIONS

This chapter presents the key features of the numerical framework used in this work. The framework was also partially verified with the cavity flow problem. In the following chapters, this framework will be applied to simulate the aerodynamics of an LEI kite airfoil, an LEI kite wing and a ram-air kite.

# 4

## AERODYNAMICS OF LEADING EDGE INFLATABLE KITE AIRFOILS

*A two-dimensional analysis of the phenomena governing the flow around leading edge inflatable membrane wings is presented. The airfoil has a tubular leading edge and a single skin membrane canopy. On the suction side, the leading edge tube smoothly connects with the canopy, but on the pressure side, the lack of the second skin leaves the airfoil open, and therefore the flow separates behind the tube and forms a recirculation zone. This chapter uses the results from a rigid curved plate experiment to validate the computational model. A boundary layer transition model is required to computationally simulate the low Reynolds number experiment with smooth surface metal. The results computed with the transition model agree well with the experiment over a large range of angles of attack. While the effect of the laminar boundary layer and flow transition in the wind tunnel experiment is significant, the real operating conditions of kite power systems have many disturbances arising, for instance, from the turbulence in the wind, high Reynolds number and rough surface. Therefore, the boundary layer transition has a minor role in aerodynamics. The validated computational model simulates the aerodynamics around a rigid leading edge inflatable kite airfoil. The simulations are carried out with and without the transition model. The suction side flow is similar to a conventional airfoil, and the transition model can capture the boundary layer transition characteristics. On the pressure side, the recirculation zone mainly depends on the angle of attack and the relative size of the tube diameter to the chord length. Generally, the aerodynamic performance of the airfoil is good, and the maximum lift coefficient is relatively high, which has additional importance for kite power systems that have the extra drag from the lines and control pod. The Reynolds number has a significant effect on the boundary layer characteristics. With low and moderate Reynolds numbers, the separation behind the leading edge tube on the pressure side occurs from a laminar boundary layer. With the higher end of the Reynolds numbers considered in this work, the transition occurs before the separation, which both delays the separation and accelerates the reattachment.*

Parts of this chapter have been published as a journal paper in [81].

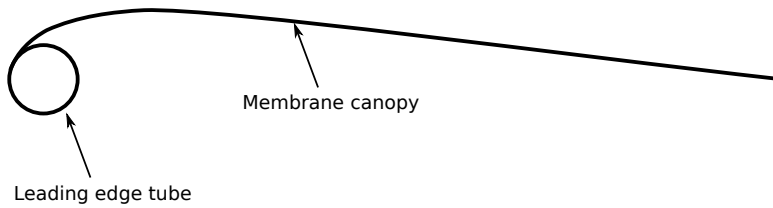


Figure 4.1: Leading edge inflatable (LEI) kite airfoil.

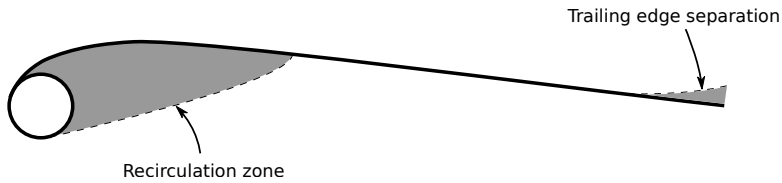


Figure 4.2: Flow topology around the LEI kite airfoil.

## 4.1. INTRODUCTION

In order to understand the complex flow around wings of finite span, it is useful first to analyze the 2D aerodynamics of a characteristic airfoil of the wing. A characteristic airfoil for leading edge inflatable kite (LEI) airfoil is shown in Figure 4.1. Single skin sailing airfoils, which usually have a similar circular leading edge structure, have been studied in the past as lightweight, cheap and good aerodynamic performance alternatives to the conventional airplane wings. The difference between LEI kite airfoil and sailing airfoil is the leading edge structure. The sailing leading edge tube is made of stiff material such as steel, wood or aluminum, and the membrane is wrapped around the tube. By contrast, the LEI kite tube itself is made of a membrane, and the tube is pre-inflated to rather high pressure before the flight. The pre-inflation makes the tube rather stiff.

Under normal flight conditions, i.e. positive lift and no large-scale separation, the shape of the suction side of the airfoil is similar to conventional airfoils. The leading edge has a constant radius and connects smoothly to the canopy, and the trailing edge is sharp. With these important characteristics similar to well-performing airfoils, a good performance is also expected from LEI kite airfoils. Figure 4.2 shows the flow topology around the airfoil. With small angles of attack, the flow remains attached and leaves the sharp trailing edge smoothly. With higher angles of attack, the flow encounters increasingly higher adverse pressure gradients, and the flow begins to separate near the trailing edge. The separation location moves towards the leading edge as the angle of attack is increased further. The lift coefficient increases with the angle of attack until the critical point at which the airfoil stalls. The lift coefficient reduces sharply in stall conditions, and large-scale flow separation is present.

In contrast to a typical wing, the pressure side of the airfoil does not have a second skin and therefore shows an open area behind the leading edge tube. The flow separates behind the tube, and the separated flow forms a recirculation zone. The size of the recirculation zone mainly depends on the angle of attack and the ratio between the chord length and the leading edge tube diameter. The zone is larger with smaller angles of at-

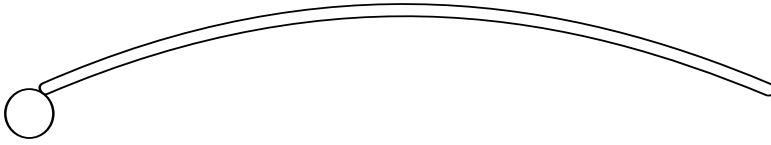


Figure 4.3: Curved plate airfoil used in the experiment by Bruining [82].

tack and reduces gradually towards higher angles of attack. The recirculation zone gives the airfoil a virtual second skin for part of the pressure side.

Unfortunately, only a few experimental studies on the aerodynamics of airfoils with circular leading edge and attached membrane canopy exist. Bruining [82] performed wind tunnel measurements of the flow around a rigid curved plate airfoil, which is geometrically similar to an LEI tube kite airfoil and therefore suitable for validation of the computational approach. The experiment of Bruining was carried out in the low-speed and low-turbulence wind tunnel of Delft University of Technology. The experimental model was made of polished steel. The laminar boundary layer and the transition are expected to significantly affect aerodynamics because of the smooth surface, low Reynolds number, and low turbulence conditions. Consequently, in the present numerical model, in addition to the commonly used fully turbulent turbulence model (SST), the transition model described in Chapter 3 is employed to achieve similar conditions as in the experiment. Note that in actual operating conditions of the kite wing, the boundary layers are expected to be primarily turbulent because of the high level of disturbances in the flow. The woven membrane skin roughness with many seams, the turbulent wind and the high Reynolds number induce an early transition to turbulent boundary layers.

The simulations are carried out for a wide range of angles of attack and Reynolds numbers to identify the most important flow effects that impact the aerodynamics of the LEI kite airfoil. For simplicity, the airfoil is assumed to be rigid. This chapter is organized as follows. Section 4.2 presents the numerical model and a mesh convergence study. The validation study is detailed in Section 4.3. Section 4.4 presents the main results of the simulations around the LEI kite airfoil. Finally, the chapter is concluded in Section 4.5.

## 4.2. NUMERICAL MODEL

The cross-section of the experimental model by Bruining [82] is shown in Figure 4.3. The model is made of two components, an arc-shaped steel plate and a cylinder. The two components are not materially joined, and therefore, there is a tiny hole between the components. The leading edge tube diameter is  $D = 0.0633c$ , and the thickness of the plate is  $t = 0.02c$ . The experiments were carried out in the low-speed, and low-turbulence (LLT) wind tunnel of Delft University of Technology, which has a turbulence intensity of the order of 0.02% and two values of the Reynolds number based on the chord length of the arc plate were considered, namely  $Re = 60000$  and  $Re = 100000$ .

The LEI kite computational model is the symmetry plane of the TU Delft V2 kite, shown in Figure 4.1. The tube diameter is  $D = 0.093c$ , and it smoothly connects with the suction side membrane. The thickness of the membrane is in the order of  $t = 10^{-5}c$ .

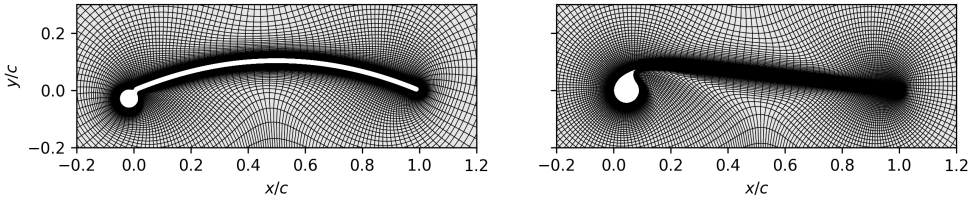


Figure 4.4: Reference meshes around the curved plate airfoil (left) and the LEI kite airfoil (right) with the mesh resolution of  $191 \times 144$  and  $255 \times 211$ , respectively.

Table 4.1: Sensitivity of computed aerodynamic coefficients with respect to mesh resolution along the airfoil surface ( $Re = 10^6$ ).

Mesh Resolution	$C_l$			$C_d$		
	$\alpha = 0^\circ$	$\alpha = 10^\circ$	$\alpha = 15^\circ$	$\alpha = 0^\circ$	$\alpha = 10^\circ$	$\alpha = 15^\circ$
$170 \times 211$	0.116	1.55	2.01	0.0387	0.0216	0.0323
$255 \times 211$	0.155	1.63	2.07	0.0396	0.0208	0.0340
$383 \times 211$	0.172	1.60	2.04	0.0399	0.0198	0.0329
$575 \times 211$	0.183	1.62	2.06	0.0402	0.0201	0.0334
$863 \times 211$	0.194	1.61	2.04	0.0403	0.0201	0.0333

The meshes around the airfoils are shown in Figure 4.4. The mesh is generated by defining a spline curve around the airfoil and discretizing the spline by clustering the points near the leading and trailing edges. The spline is extruded with a hyperbolic extrusion algorithm. To assess the effect of the mesh resolution on the simulation results, a sensitivity analysis is conducted using the  $\gamma - \tilde{Re}_{\theta_t}$  transition model. The investigated parameters are the number of discretization points along and normal to the airfoil surface. The resolution is increased in each direction consecutively by a factor of 1.5. The computed lift and drag coefficients for increasing resolution along the airfoil surface are given in Table 4.1. Three values for the angle of attack are investigated, namely  $\alpha = 0^\circ$ ,  $10^\circ$  and  $15^\circ$ . The mesh-dependency of the results decreases for increasing angle of attack, probably due to the larger recirculation zone on the pressure side, leading to instabilities and higher mesh sensitivity. Nevertheless, the results are well converging for higher angles of attack ( $\alpha = 10^\circ$  and  $15^\circ$ ) and satisfactorily when the airfoil is aligned with the flow ( $\alpha = 0^\circ$ ). Thus, the mesh with 575 cells along the surface of the airfoil is considered to be adequate. In the wall-normal direction, two different Reynolds numbers are studied to ensure that the first cell size requirement  $y^+ < 1$  is met for high Reynolds numbers. The resulting lift and drag coefficients are given in Table 4.2, indicating that 211 points in the wall-normal direction are sufficient for convergence. Therefore, the  $575 \times 211$  mesh is chosen for the subsequent computational analysis of the LEI kite airfoil. A similar sensitivity analysis is conducted for the curved plate airfoil to be used in the subsequent validation study. The analysis leads to a computational mesh with 287 cells along the airfoil surface and 215 cells normal to the surface.

Table 4.2: Sensitivity of computed aerodynamic coefficients with respect to mesh resolution normal to the airfoil surface ( $\alpha = 10^\circ$ ).

Mesh Resolution	$C_l$		$C_d$	
	$Re = 10^6$	$5 \times 10^7$	$Re = 10^6$	$5 \times 10^7$
575×63	1.61	1.65	0.0199	0.0161
575×94	1.62	1.66	0.0200	0.0159
575×141	1.62	1.66	0.0199	0.0158
575×211	1.62	1.67	0.0201	0.0158
575×317	1.63	1.67	0.0202	0.0159
575×475	1.63	1.67	0.0202	0.0158

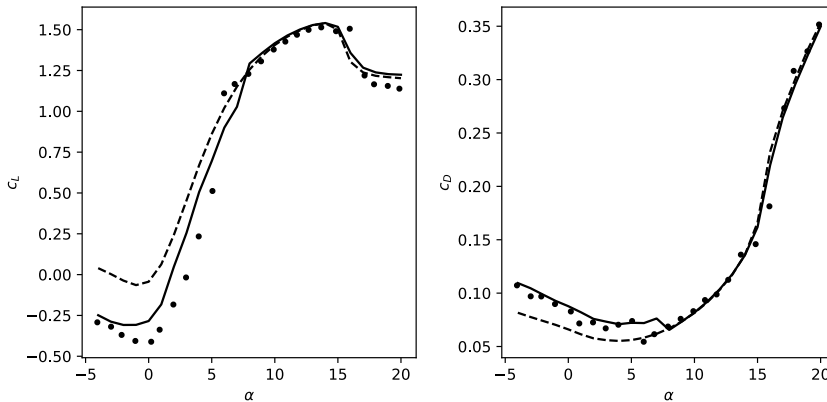


Figure 4.5: Lift (left) and drag (right) coefficients of the curved plate airfoil as functions of the angle of attack. The experimental results[82] are shown as marker symbols, the simulation results with transition model are shown as solid line and the results without transition model as dashed line.

### 4.3. VALIDATION ASSESSMENT

The numerical simulations are compared with the experiment by Bruining [82] for  $Re = 10^5$ . The measured and computed aerodynamic coefficients are shown in Figure 4.5. The simulations with the transition model are closer to the experimental results than those without the transition model. This is expected since the Reynolds number is rather low, and the surface of the wind tunnel model is smooth. Furthermore, the numerical results for a low angle of attack show a negative lift coefficient when using the transition model and a positive coefficient for a fully turbulent boundary layer. This is consistent with the measurements of Bot et al. [83] of the flow around a two-dimensional curved plate. Note that the pressure side of the leading edge is sharp, unlike in the curved plate airfoil model. In Figure 4.6 these measurements are compared with the present curved plate airfoil simulations for zero angle of attack. For  $Re < 2 \times 10^5$ , the measured lift coefficient is negative because the flow separates early from the laminar boundary layer. For  $Re > 2 \times 10^5$ , the boundary layer transitions to turbulence while still being fully attached to the airfoil. The intensified turbulent mixing has the well-known effect of delaying flow

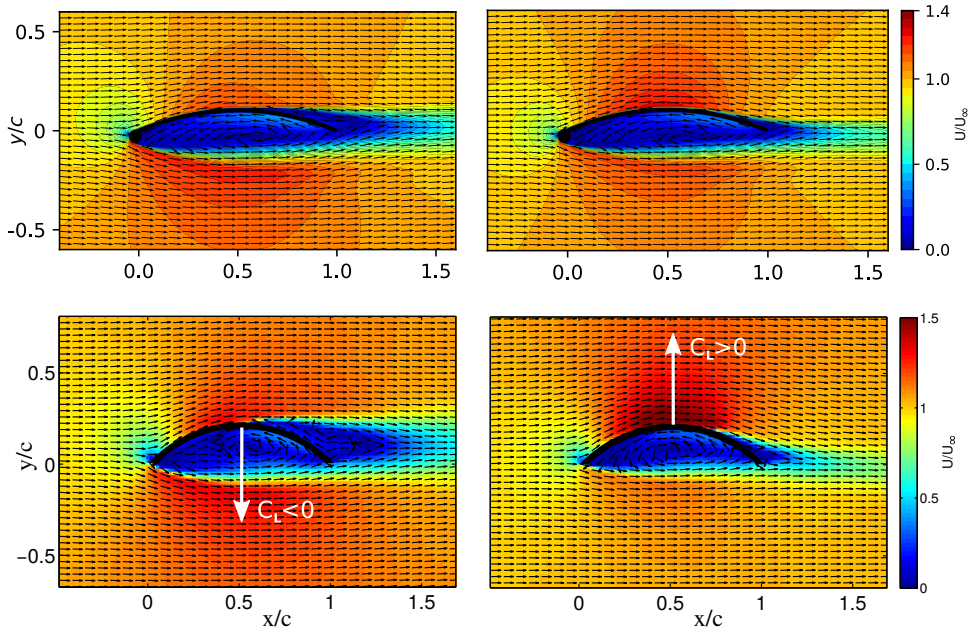


Figure 4.6: Comparison of the present numerical simulation with the experiment of Bot et al.[83] Top row: simulation with (left) and without (right) transition model. Bottom row: experiment for  $Re < 2 \times 10^5$  (left) and  $Re > 2 \times 10^5$  (right).

separation. As a result, the measured lift of the plate increases abruptly to a positive value at around  $Re = 2 \times 10^5$  while the drag decreases. A similar effect can be observed in the numerical simulations of the curved plate airfoil. With the transition model, the laminar boundary layer separates from the airfoil, while without the transition model, the boundary layer is always turbulent and therefore, the separation is delayed.

Figure 4.5 shows that with increasing angle of attack, the measured aerodynamic coefficients change abruptly at around  $\alpha = 6^\circ$ . A similar abrupt change can be identified for the computed coefficients of the curved plate airfoil at  $\alpha = 8^\circ$ . For higher angles of attack, the boundary layer encounters the adverse pressure gradient increasingly earlier with the effect that also transition is triggered earlier. Because a turbulent boundary layer can better sustain an adverse pressure gradient, the effect on aerodynamics is generally positive. Figure 4.7 shows the computed pressure field and streamlines around the airfoil for  $\alpha = 7^\circ$  and  $8^\circ$ , which is the angle of attack range in which the lift suddenly increases. The hole on the suction side of the airfoil, where the two wing elements are joined, is occupied by a small separation bubble. At  $\alpha = 0^\circ$ , this bubble does not disturb the primary flow over the airfoil. With increasing angle of attack, the hole-induced separation bubble enlarges but still reattaches without transition. At  $\alpha = 8^\circ$ , the transition also occurs within the separation bubble and therefore, the lift coefficient sharply increases and the drag coefficient decreases. This explains why the simulations with and without transition models lead to very similar results with angles of attack larger than  $8^\circ$ . Overall, the simulations with the combination of turbulence and transition models

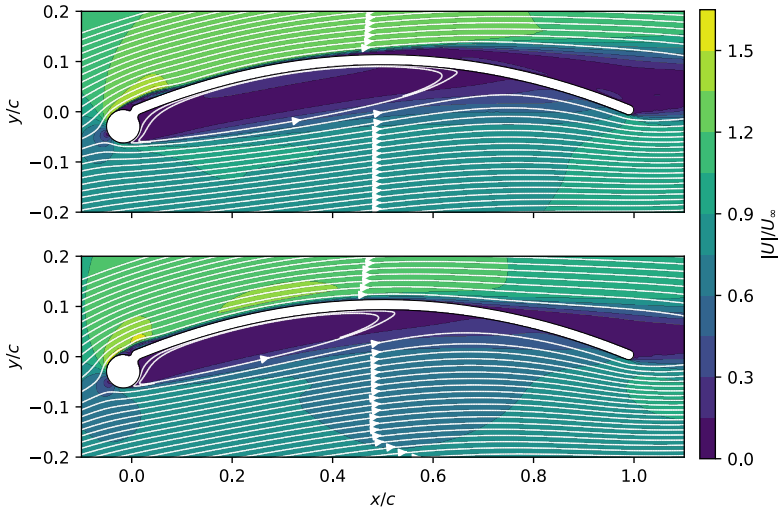


Figure 4.7: Computed streamlines and normalized flow velocity around the curved plate airfoil, using the transition model, at  $7^\circ$  (top) and  $8^\circ$  (bottom) angle of attack.

agree well with the experiments, even at large angles of attack.

#### 4.4. RESULTS

The verified and validated simulation setup is used to analyze the aerodynamics of LEI kite airfoil for a wide range of angles of attack and Reynolds numbers that represent the traction and retraction phases of AWE systems. The angle of attack is varied up to the critical value at which the stall occurs. The configurations beyond this point are not considered because the steady-state solver is not suitable for the inherently unsteady post-stall flow conditions. The Reynolds number is varied from  $Re = 10^5$  to  $5 \times 10^7$ . Results are presented for simulations with and without transition modeling.

The aerodynamic coefficients computed without transition modeling are presented in Figure 4.8. The general trends are in line with those for conventional airfoils. With increasing Reynolds number, the lift coefficient increases and the drag coefficient decreases, leading to improved aerodynamic performance. Also, the critical stall angle increases resulting in higher maximum lift coefficients. Figure 4.9 shows the streamlines and the normalized velocity magnitude around the airfoil at  $Re = 10^6$  for several values of the angle of attack. As the angle of attack increases, the recirculation zone on the pressure side of the airfoil decreases in size, which increases lift and decreases drag.

Taking laminar-turbulent transition into account significantly affects the flow simulation. Figure 4.10 shows the aerodynamic coefficients computed with the transition model. At the lowest considered Reynolds number,  $Re = 10^5$ , the aerodynamic performance is worse than computed without transition model. The lower lift and higher drag are caused by a longer laminar separation bubble on the suction side, as indicated by Figure 4.11. Although the flow still reattaches, the airfoil stalls at much lower angles of attack, i.e.  $\alpha = 6^\circ$ , because the flow separates relatively early from the laminar boundary

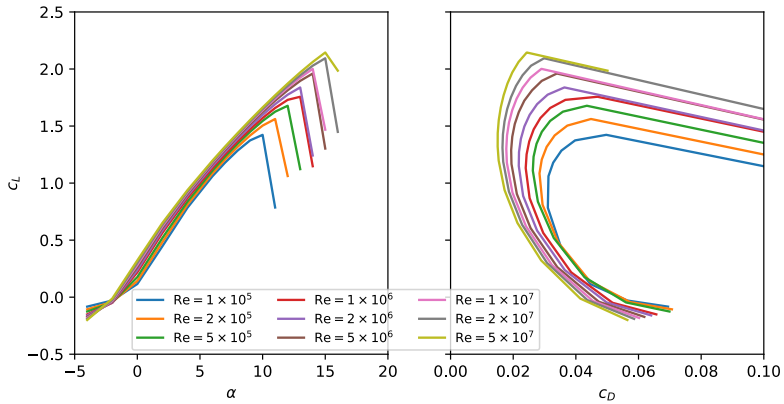


Figure 4.8: Lift coefficient as function of angle of attack (left) and drag polar (right) for the LEI kite airfoil at various Reynolds numbers, computed without transition model.

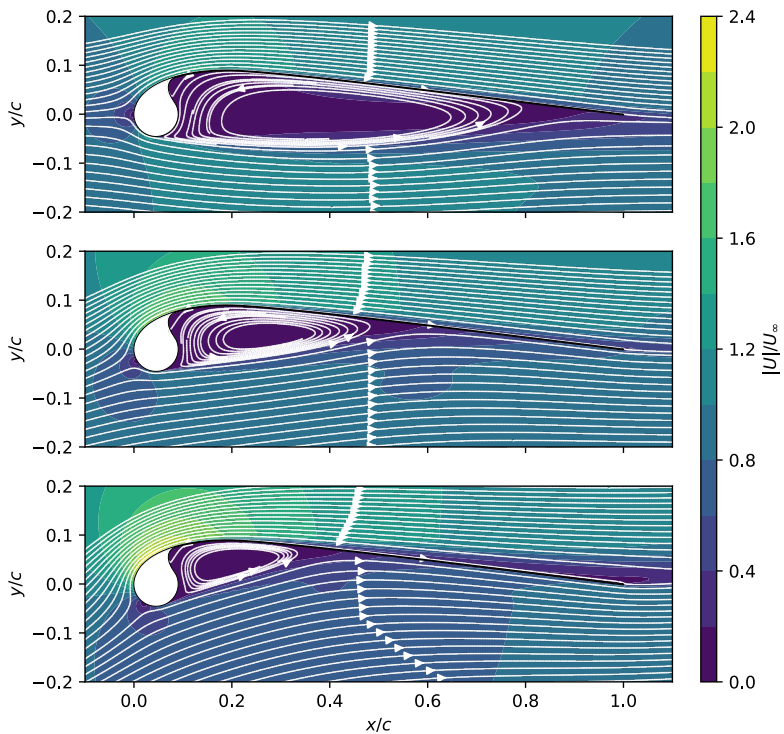


Figure 4.9: Streamlines and normalized flow velocity around the LEI kite airfoil, computed without transition modeling at  $Re = 10^6$  for  $\alpha = 0^\circ$  (top),  $\alpha = 6^\circ$  (center) and  $\alpha = 12^\circ$  (bottom).

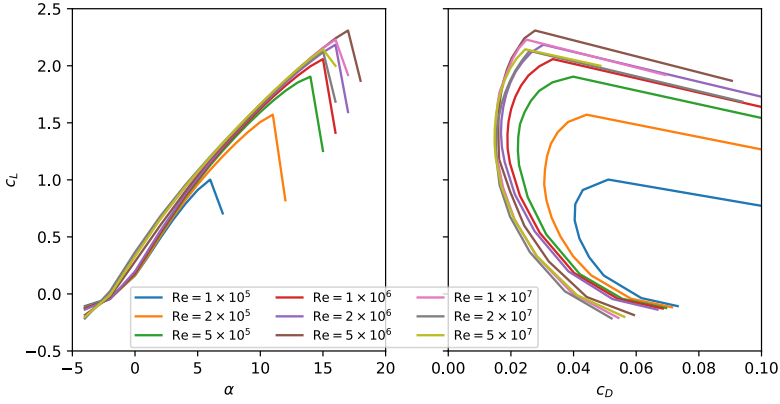


Figure 4.10: Lift coefficient as function of angle of attack (left) and drag polar (right) for the LEI kite airfoil at various Reynolds numbers, computed with transition model.

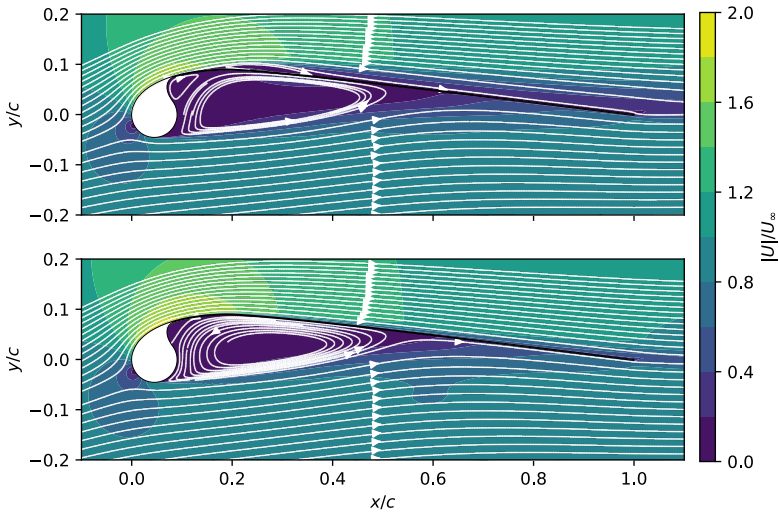


Figure 4.11: Streamlines and the normalized flow velocity around the LEI kite airfoil, computed with transition modeling at  $\alpha = 6^\circ$  for  $Re = 10^5$  (top) and  $Re = 5 \times 10^5$  (bottom).

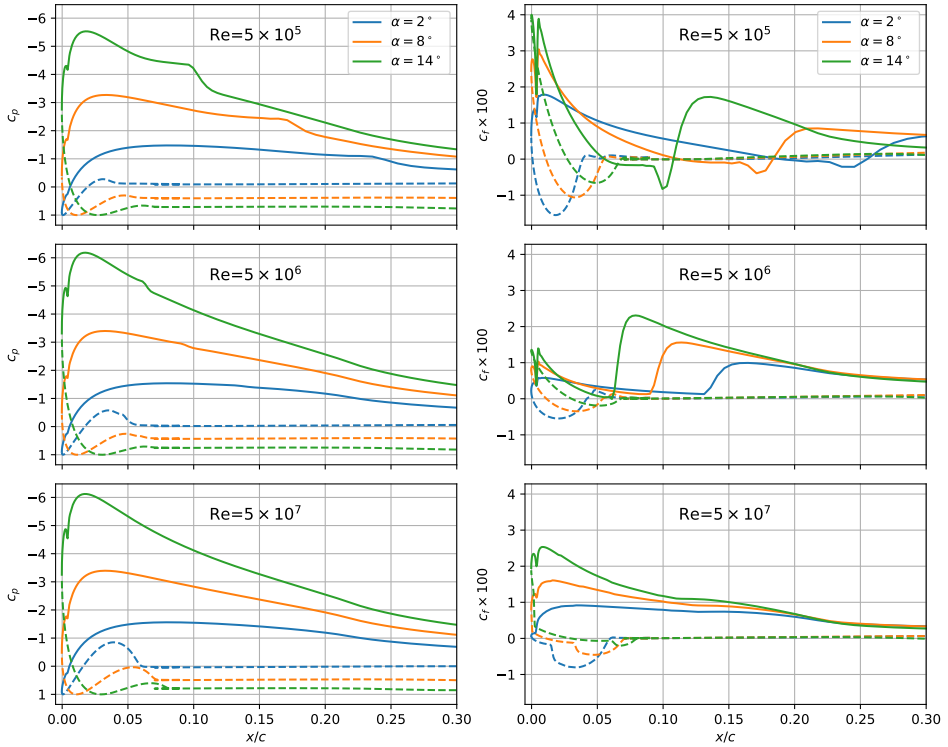


Figure 4.12: Pressure coefficient  $c_p$  (left) and friction coefficient  $c_f$  (right) near the leading edge, computed with transition modeling. Solid line is the suction side and dashed line is the pressure side.

layer. Increasing the Reynolds number from  $Re = 1 \times 10^5$  to  $2 \times 10^5$  leads to an increase of the stall angle from  $6^\circ$  to  $11^\circ$  because the boundary layer now transitions to turbulent before the flow separates, which therefore the separation is delayed. Increasing the Reynolds number further, the stall angle increases consistently until reaching the maximum lift coefficient at  $Re = 5 \times 10^6$ . Above  $Re = 5 \times 10^6$ , the stall angle first decreases and beyond  $Re = 2 \times 10^7$ , the stall angle and maximum lift coefficient begin to increase again.

The transition, separation and reattachment regions can be identified based on the skin friction coefficient  $c_f$ . The minimum and maximum values of this coefficient are used to define the onset and end of the transition region. Figure 4.12 shows the skin friction and pressure coefficients at various angles of attack and Reynolds numbers. On the suction side (solid line), the pressure coefficient shows consistent behavior with conventional airfoils. The peak suction strongly depends on the angle of attack, and the Reynolds number has a significant effect on the boundary layer transition. When increasing the Reynolds number from  $Re = 5 \times 10^5$  to  $5 \times 10^6$ , the shape of the pressure distribution and the magnitude of it is altered. At  $Re = 5 \times 10^5$  (top panels), the flow transitions through a laminar separation bubble that can be seen as a plateau in the pressure coefficient and a negative friction coefficient. The bubble moves towards the

leading edge when the angle of attack is increased. By increasing the Reynolds number to  $Re = 5 \times 10^6$ , the transition occurs without separation bubble (no negative friction), and therefore the effect of transition is minor on the pressure coefficient. The transition is not anymore visible in the pressure distribution with  $Re = 5 \times 10^7$ , and hence the pressure curve is smooth.

On the pressure side (dashed line), the stagnation point ( $c_p = 1$ ) moves towards the trailing edge when the angle of attack increases. The increment in the angle of attack also delays the formation of the recirculation zone. Like the laminar separation bubble on the suction side, the recirculation zone causes the pressure coefficient to plateau and the friction coefficient changes sign. The location of the reattachment of the recirculation strongly depends on the angle of attack, as shown before in Figure 4.9. The recirculation zone formation occurs directly from the laminar boundary layer in the case of  $Re = 5 \times 10^5$  and  $Re = 5 \times 10^6$ . With  $Re = 5 \times 10^7$ , the boundary layer transitions to turbulent before the recirculation zone is formed, and the transition causes a steep increase in the magnitude of the friction coefficient. The transition onset locations on the pressure side are in reverse order compared to the suction side. The transition onset occurs earlier with the lower angles of attack than for the higher angles of attack.

## 4.5. CONCLUSIONS

Previous studies on airfoils with circular leading edge focused only on low Reynolds numbers. However, leading edge inflatable kites used for AWE systems also encounter high Reynolds numbers. In this chapter, a wide range of angles of attack and Reynolds numbers were investigated for an LEI kite airfoil with a fixed shape. The computational setup was verified by conducting a mesh uncertainty assessment and validated by comparing the simulation results with a low Reynolds number experiment on a geometrically similar curved plate airfoil. Because of the low level of turbulence, low Reynolds number and smooth steel airfoil in the experiment, a transition model was needed in the simulation model.

For the curved plate airfoil, it is shown that the numerical model that includes the boundary layer transition model agrees well with the experimental results over the whole range of angles of attack. By contrast, the results without transition modeling differ significantly from the experimental data, especially at small angles of attack. The drag coefficient was under-predicted without transition modeling. For angles of attack larger than  $8^\circ$ , both approaches showed similar results because the boundary layer transitions early on with the transition model. By contrast, for  $\alpha < 8^\circ$ , the flow does not transition before the separation, and therefore the laminar boundary layer separates earlier than the turbulent boundary layer without using the transition model.

The simulations on the LEI kite airfoil were performed with a wide range of angles of attack and Reynolds numbers. It was found that the aerodynamic phenomena on the suction side are similar to conventional airfoils. On the pressure side, the size of the recirculation zone is highly dependent on the angle of attack, with the zone getting smaller at higher angles of attack. The Reynolds number has a minor effect on the aerodynamics, especially without the transition model. The turbulent boundary layers become thinner with increasing Reynolds number and therefore the aerodynamic performance is improved. Higher Reynolds numbers result in higher lift and lower drag coefficients with

stall occurring at higher angles of attack. On the pressure side, the separation behind the tube occurs directly from a laminar boundary layer with low and moderate Reynolds numbers. At large Reynolds number, the flow transitions along the tube before separation, which leads to a smaller recirculation zone.

This chapter has provided a better understanding of the aerodynamics of an LEI kite airfoil. The next chapter will extend the investigation to a three-dimensional LEI kite wing.

# 5

## AERODYNAMICS OF A LEADING EDGE INFLATABLE KITE

*The previous chapter focused on the aerodynamics of two-dimensional leading edge inflatable kite airfoils. This chapter extends the work to the whole three-dimensional wing. The same steady-state methodology is applied for a fixed V3 leading edge inflatable kite wing shape. A wide range of Reynolds numbers, angles of attack and sideslip angles are considered, representing the real operating conditions of the systems. The aerodynamic coefficients of the wing show similar trends to those of the two-dimensional airfoil, though the aerodynamic performance is lowered by the low aspect ratio and high anhedral wing configuration. Additionally, the effect of chordwise inflatable struts is investigated by creating two computational models, one with struts and the other without. The aerodynamic coefficients do not show a significant dependence on the struts, which allows using simplified geometric kite models in future studies.*

## 5.1. INTRODUCTION

A leading edge inflatable (LEI) kite wing has a C-shape wing planform that transfers the aerodynamic forces from the tensile wing to the tether via the bridle line system. Consequently, the high anhedral and low aspect ratio wing induces three-dimensional flows and its aerodynamic efficiency is substantially lowered from the idealized infinite length straight LEI kite airfoil in Chapter 4. In addition to the inflatable bow-shaped leading edge tube, the LEI kite wing also has inflatable strut tubes in the chordwise direction on the pressure side for chordwise reinforcement. During the traction phase of the kite power system, the kite flies in a crosswind motion, and the weight of the kite leads to sideslip. The resulting side force balances the weight of the kite. Consequently, the sideslip angle is considered in addition to the Reynolds number and angle of attack. The V3 kite has the same wetted surface area of  $25 \text{ m}^2$  as the previous V2 design, but the aerodynamic efficiency is improved by flattening the wing and increasing its aspect ratio [9]. The unique characteristic of the wing is the wavy leading edge tube that preforms the wing into a loaded state and therefore reduces the wing deformations.

In this chapter, the same methodology is used as for the two-dimensional wing section in Chapter 4. The wing shape is kept fixed, and no deformations are considered. In some of the previous CFD studies on the LEI kite wings, the struts of the LEI kite were removed to simplify the mesh generation step [25, 48]. In the present work, the aerodynamics of the wing, with and without the struts, are compared. The chapter is organized as follows. Section 5.2 presents the numerical model, including the geometric simplifications and mesh generation. Section 5.3 presents the results with flow visualizations to identify the characteristic flows for different Reynolds numbers, angles of attack and sideslip angles. Finally, Section 5.4 summarizes the main observations of the study. This chapter is based on the work of Viré et al.[84], Demkowicz [25] and Lebesque [52]. The author of this thesis developed the numerical model with the MSc thesis workers and also supervised both thesis works.

## 5.2. METHODOLOGY

The wing geometry considered is the geometry of the LEI V3 kite wing that is introduced in Chapter 2. The shape is kept fixed without taking any deformations into account. As described in Chapter 3, mesh generation for the LEI kite is a challenging task. The LEI kite wing consists of an inflatable tube frame and a canopy. The components are connected by seams that result in sharp corners. In the computational model, the wedge-shaped fluid volumes formed at the connections between the tubes and the canopy are filled to extrude the boundary layer mesh without intersecting cells. In this work, two wing models are built: one with inflatable streamwise tube struts and another without them to assess the effect of the struts on the wing aerodynamics. Apart from this, the geometries are the same. The geometries of the two models are shown in Figure 5.1.

Figure 5.2 shows the surface mesh topology. The mesh is generated by using the commercial software Pointwise which allows combining structured, and unstructured mesh generation algorithms [74]. The major part of the surface mesh is generated by lofting through sections along the span of the wing. Near the wingtip and at the ends of the struts, Pointwise's T-Rex unstructured algorithm is used to generate the surface mesh

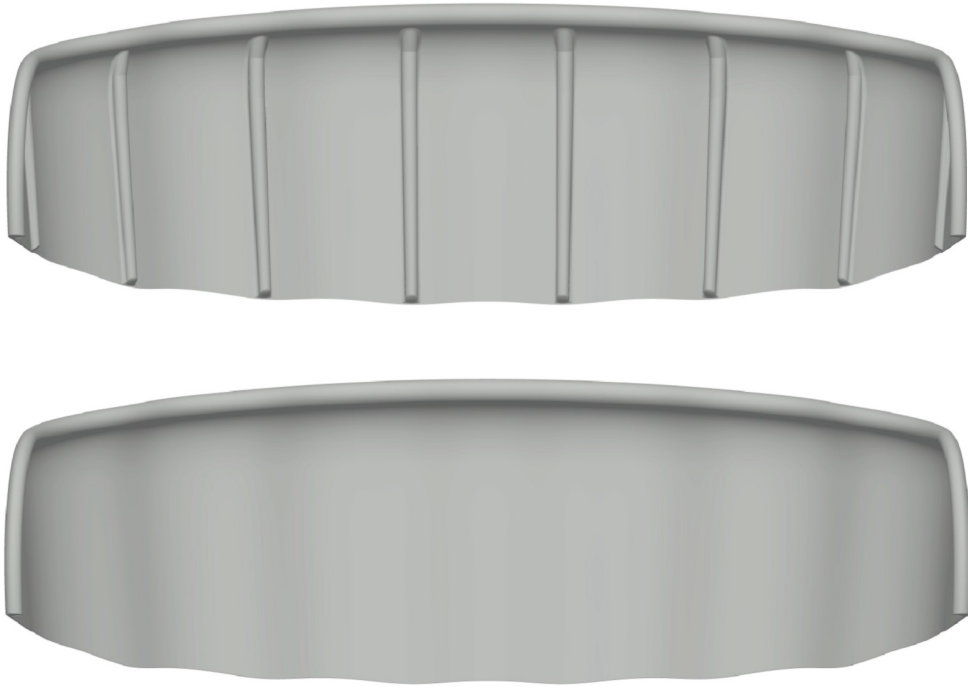


Figure 5.1: The pressure side of the V3 kite computational geometry with struts (above) and without struts (below). Figures taken from [52].

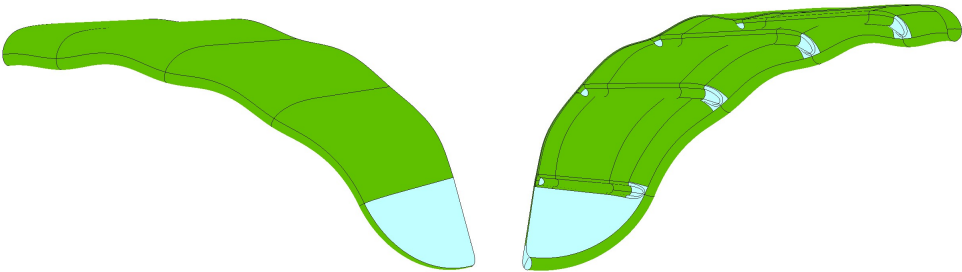


Figure 5.2: The partitioning of the surface mesh on the suction side (left) and on the pressure side (right). Green color indicates the structured blocks and blue the unstructured blocks. Figures taken from [52].

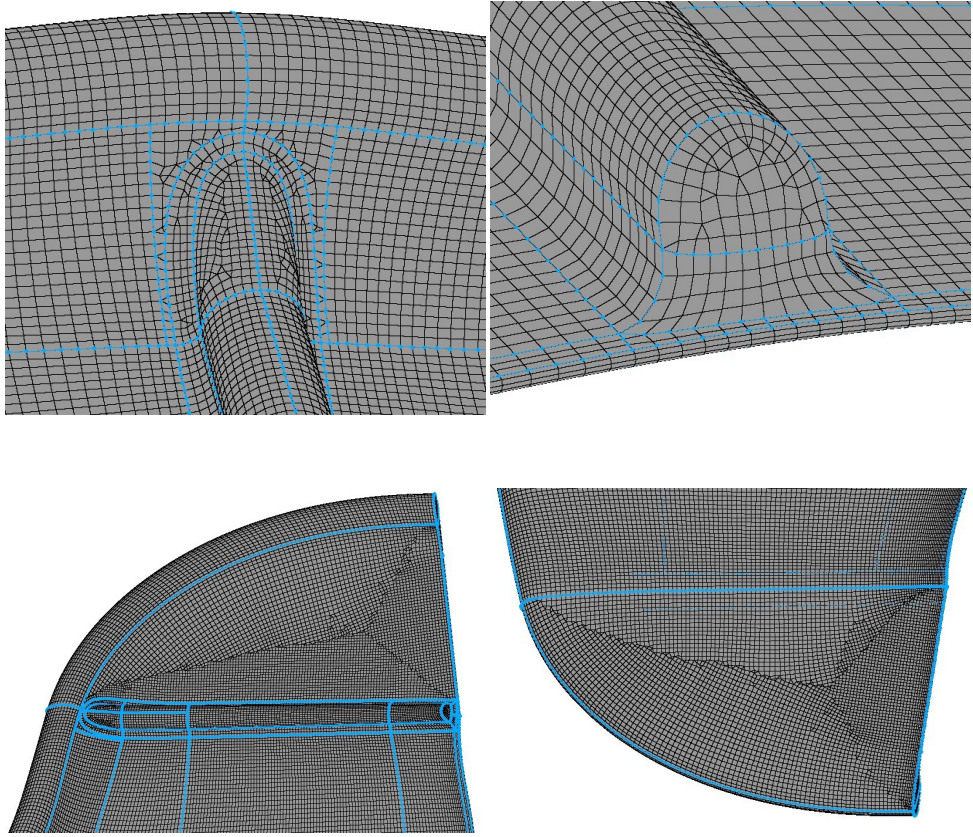


Figure 5.3: The unstructured regions of the surface mesh. Figures taken from [52].

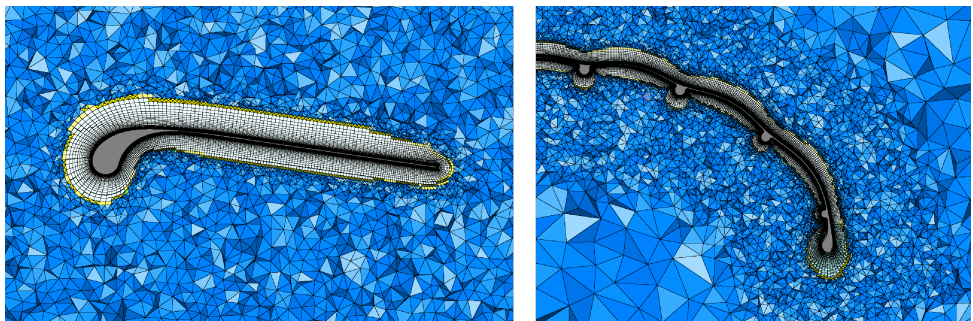
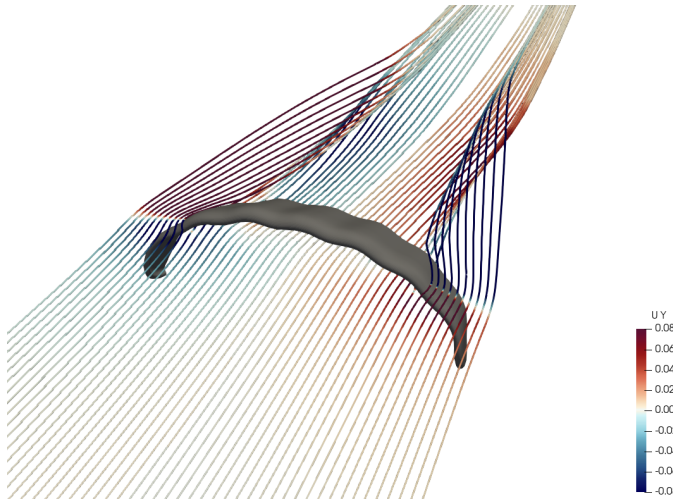


Figure 5.4: The volume mesh near the symmetry plane (left) and on a chordwise plane at  $x = 0.3$  (right). Grey color indicates the extruded boundary layer mesh with hexahedra and prisms, yellow color indicates the interface layer consisting of pyramids and blue color indicates the farfield mesh with tetrahedra. Figures taken from [52].

Table 5.1: Sensitivity of computed aerodynamic coefficients to the mesh resolution for  $Re = 3 \times 10^6$  and  $\alpha = 12^\circ$ .

Level	1	2	3	4	5
Cell count [ $10^6$ ]	5.67	6.78	8.10	9.54	10.9
Simulation time [hours]	4.3	4.9	5.7	6.5	9.5
$C_L$ [-]	1.052	1.055	1.0532	1.0503	1.0515
$C_D$ [-]	0.111	0.112	0.110	0.111	0.109

Figure 5.5: Streamlines around the wing for  $Re = 3 \times 10^6$  and  $\alpha = 12^\circ$ . The streamlines are colored by the spanwise velocity. Figures taken from [25].

(Figure 5.3). The T-REX algorithm is also used to extrude the volumetric mesh from the surface mesh (Figure 5.4). The mesh generation process has been described in more detail in Chapter 3.

The mesh sensitivity is assessed by a mesh refinement study. Table 5.1 shows the mesh sizes, simulation time on a computer with 20 CPU cores and the resulting aerodynamic coefficients. The refinement level 3 is chosen because it shows a good compromise between simulation time, mesh independence and geometric quality, such as high orthogonality. All the simulations were run for between 4000 and 6000 iterations. The normalized residuals and the force coefficients were monitored. Generally, all normalized residuals fall below  $10^{-6}$  besides in the case of the stall. In the stall condition, the largest residuals remained at approximately  $10^{-5}$ . Nevertheless, already after 2000 iterations, the force coefficients showed an adequate level of convergence without significantly changing anymore. Due to the moderate level of convergence and the use of a steady-state flow solver, the results with large-scale separation are indicative and should be used with an appropriate level of criticism.

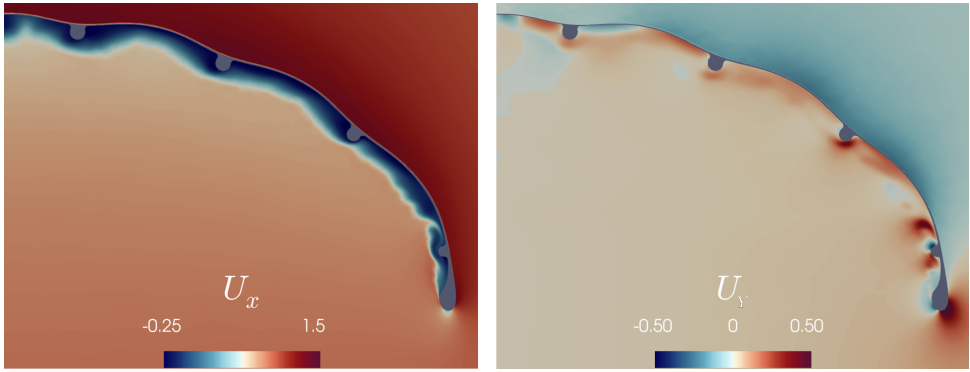


Figure 5.6: Velocity in chordwise (left) and spanwise direction (right) on a plane normal to the chordwise direction at  $x = 0.3$  with  $Re = 3 \times 10^6$  and  $\alpha = 12^\circ$ . The velocity is normalized by  $U_\infty$ . Figures taken from [52].

## 5

### 5.3. RESULTS

Figure 5.5 shows the streamlines around the wing for  $Re = 3 \times 10^6$  and  $\alpha = 12^\circ$ . The streamlines originate from a horizontal line located upstream of the wing. The vertical location is chosen such that the streamlines hit the wing at approximately at the quarter span of the wing. Behind the wing, the streamlines tangle, which indicates trailing vortices. The spanwise velocity component indicates that the flow is pushed towards the center of the wing on the suction side and outwards on the pressure side.

The wavy spanwise profile of the wing leads to complex flows, especially on the pressure side of the wing. Figure 5.6 shows the velocity in  $x$ - and  $y$ -direction on a plane normal to the chordwise direction at  $x = 0.3c$ . The blue color in the left panel marks the separated flow in the recirculation zone behind the leading edge tube. The right panel shows the crossflow induced by the wavy  $c$ -shape of the wing. Towards the wingtip, the flow is pushed more and more sideways along the surface by the pressure difference between the two sides. The crossflow is mostly outwards on the pressure side, except in the recirculation zones around the chordwise tubes. On the suction side, the velocity is consistently directed towards the center of the wing. The bumpy shape causes the magnitude of the crossflow to oscillate.

Figure 5.7 shows the lift and drag coefficient of the wing for a range of Reynolds numbers  $10^5 \leq Re \leq 15 \times 10^6$  and for angles of attack varying between  $-5^\circ$  and  $24^\circ$ . The results are consistent with the two-dimensional LEI kite airfoil in Chapter 4. With the lowest Reynolds number of  $Re = 10^5$  the flow separates directly from a laminar boundary layer, and the wing stalls already at an angle of attack of  $\alpha = 6^\circ$ . The highest lift coefficient from the Reynolds numbers considered in this work is achieved at  $Re = 10^6$ . The maximum lift coefficient is at around  $C_{L,max} = 1.3$ , which is significantly lower than for the idealized infinite length airfoil ( $c_{L,max} = 2.3$ ) presented in Chapter 4. The stall angle and the maximum lift coefficient decrease when increasing the Reynolds number further. Moreover, the lift coefficient increases and the drag coefficient decreases abruptly with the lower range of angles of attack when the Reynolds number is increased from  $Re = 5 \times 10^6$  to  $Re = 10^7$ . The flow transition mechanism can explain this behavior.

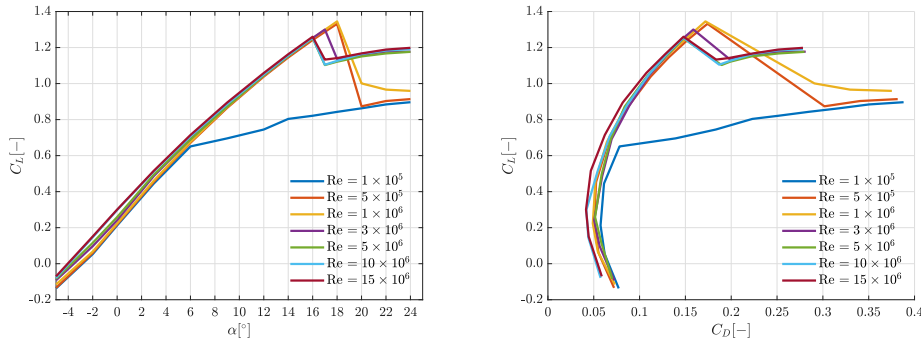


Figure 5.7: Lift (left) and drag (right) coefficient for the LEI wing computed at various Reynolds numbers. Figures taken from [25].

Figure 5.8 shows the friction coefficient, for three Reynolds numbers (increasing from left to right) and an angle of attack of  $\alpha = 12^\circ$ . Negative values of  $C_f$  indicate regions of flow recirculation, while a sudden increase in skin friction represents laminar to turbulent transition. At the lowest Reynolds number, the suction side surface plots show a distinct laminar separation bubble across the whole span of the wing. This bubble vanishes at  $Re = 3 \times 10^6$ , where the boundary layer transitions without a separation bubble. At  $Re = 10^7$ , the transition occurs almost immediately when the flow approaches the wing. The recirculation zone is clearly marked with a negative friction coefficient on the pressure side. The increment in Reynolds number leads to earlier reattachment and, therefore smaller recirculation zone. By looking closely at the leading edge tube, the high friction region is partially extended in the chordwise direction. At the same locations, the recirculation zone has shrunk due to boundary layer transition occurring before flow separation from the leading edge tube. The white chordwise traces on the pressure side show the footprints of the spanwise flow structures resulting from the wavy shape.

Sideslip together with dihedral introduce a side force that balances the weight of the kite during crosswind flight. Figure 5.9 shows the aerodynamic coefficients with a sideslip angle. Like the angle of attack, the sideslip angle increases the wing's frontal area and leads to a (nonlinear) drag increment. Also, as expected, the side force increases with the sideslip angle. The dependency is similar to the lift dependency on the angle of attack. Thus, the side force depends linearly on the sideslip angle until the flow separates. The wing is stalled with the lowest Reynolds number and the highest angle of attack ( $Re = 10^6$  and  $\alpha = 12^\circ$ ). Note that the results are only shown with four sideslip angles ( $0^\circ$ ,  $4^\circ$ ,  $8^\circ$  and  $12^\circ$ ) and, therefore, the curve abruptly changes from the linear region to the stall at  $Re = 10^6$ . The glide ratio ( $L/D$ ) decreases with the sideslip angle because of the decreased lift and the increased drag.

Figure 5.10 shows the velocity in  $y$ -direction at two chordwise planes with (above) and without (below) the chordwise struts. The upper two planes are near the leading edge, and the lower two are near the trailing edge. A positive sideslip angle means that the  $y$ -component of apparent velocity is aligned from left to right. On the suction side, the left side of the wing is facing the wind and, therefore, aligned with the pressure gra-

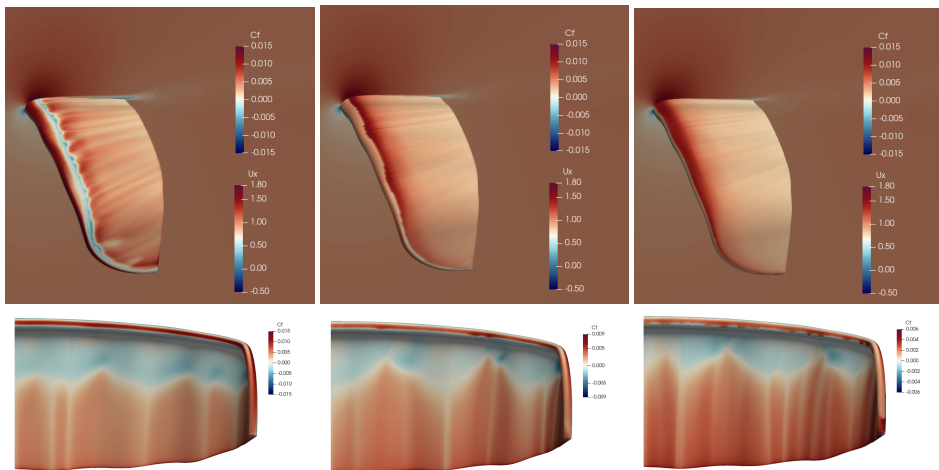


Figure 5.8: Friction coefficient of the wing at the suction side (top) and pressure side (bottom) for an angle of attack of  $\alpha = 12^\circ$  and three Reynolds numbers:  $Re = 5 \times 10^5$  (left),  $Re = 3 \times 10^6$  (centre), and  $Re = 10^7$  (right). Figures taken from [25].

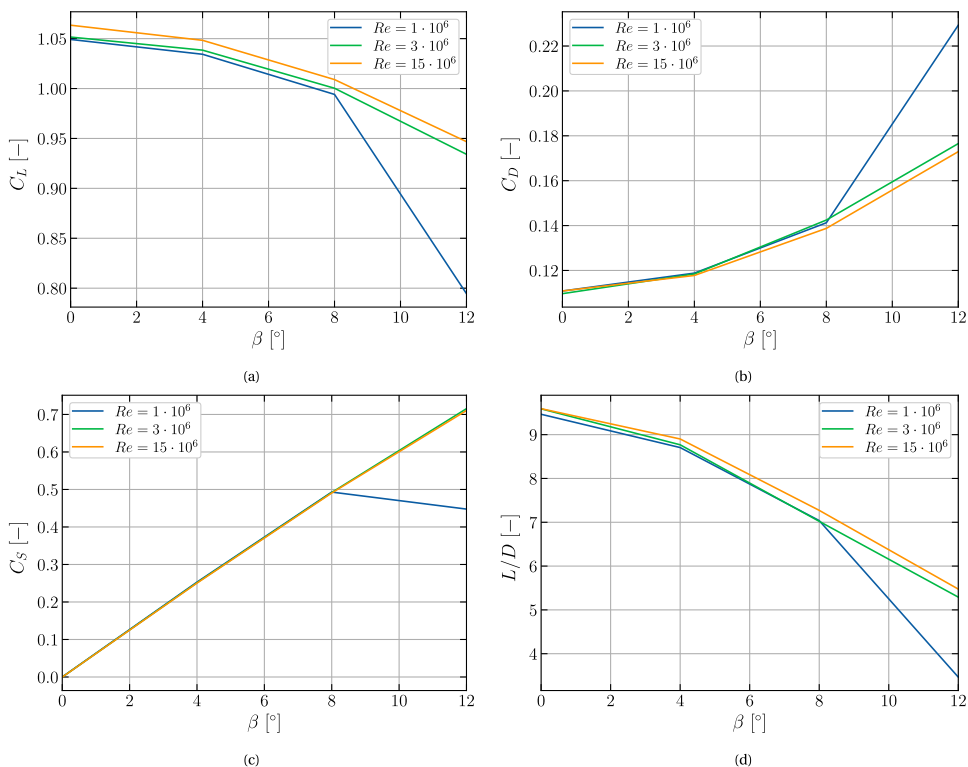


Figure 5.9: (a) lift, (b) drag and (c) sideforce coefficient, and (d) glide-ratio as a function of sideslip angle with  $\alpha = 12^\circ$ . Figures taken from [52].

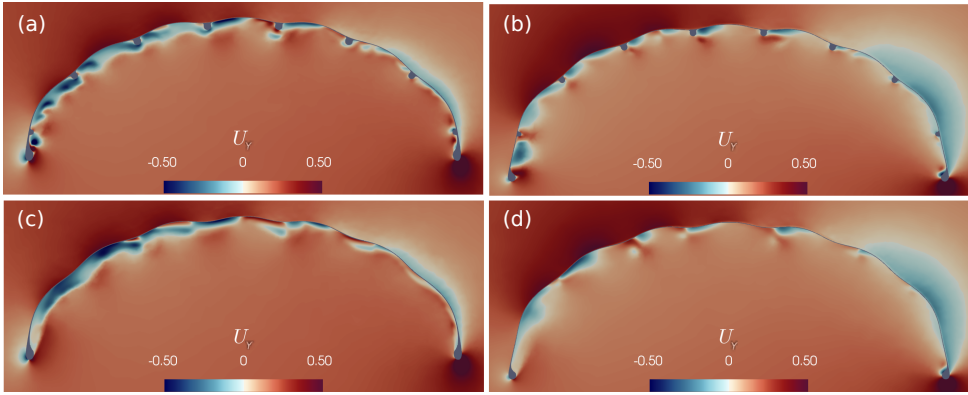


Figure 5.10: The velocity in spanwise direction on chordwise planes at  $x = 0.3c$  (left) and  $x = 0.6c$  (right) with  $\beta = 12^\circ$ ,  $\alpha = 12^\circ$ ,  $Re = 3 \times 10^6$ . The planes above are with and below without the inflatable struts. Figures taken from [52].

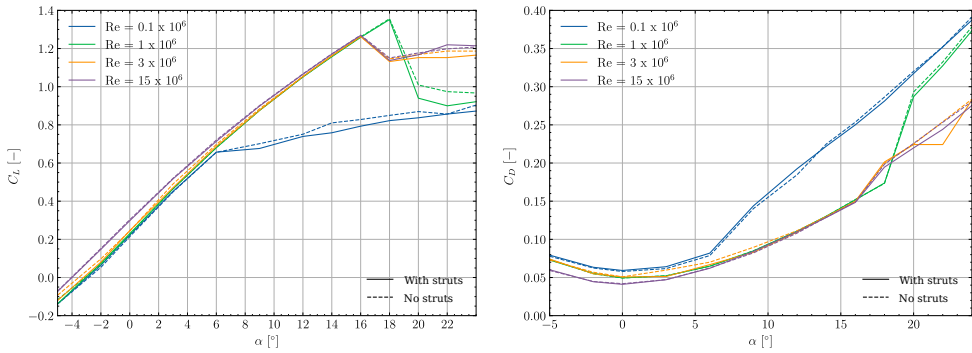


Figure 5.11: The lift and drag coefficient with and without struts. Figures taken from [52].

dient in the  $y$ -direction. Consequently, the velocity is accelerated in comparison to the case with zero slip in Figure 5.6. On the right side of the wing, the flow encounters an adverse pressure gradient in the  $y$ -direction, and therefore, the flow is pushed back towards the center of the kite near the wingtip. The opposite is true for the pressure side of the wing. The influence of slip is more prominent near the leading edge than closer to the trailing edge. Generally, the flow around the wing with and without struts looks similar, although some local differences are observed on the pressure side. This is further confirmed in Figure 5.11 that shows the lift and drag coefficients with and without the inflatable struts. The lines are nearly overlaid with each other, and therefore, the effect of the struts on the force coefficients is almost negligible. Thus, the spanwise flow and the aerodynamic performance are dominated by the wing topology rather than the inflatable tube struts.

## 5.4. CONCLUSIONS

This work extends the two-dimensional LEI kite airfoil results of the previous Chapter 4 to the complete three-dimensional wing. Some of the observations of the flow along the airfoil are also seen on the wing. For example, a large recirculation is present on the pressure side in both cases. Also, at low  $Re$ , the wing stalls at a small angle of attack due to the bursting of a laminar separation bubble on the suction side. Overall, as expected, the aerodynamic performance of the wing is inferior to the infinite airfoil wing due to the highly three-dimensional wing planform with a low aspect ratio and a high anhedral angle. In this chapter, the influence of a non-zero sideslip angle is investigated. It is found that the side force and the drag dependency on the sideslip angle show similar behavior to the lift and the drag dependency on the angle of attack. Finally, the effect of the inflated chordwise struts on the flow around the wing is investigated. Flow visualizations show minor differences in the local flow topology in the vicinity of the struts compared to the wing without struts. However, the struts do not influence the overall aerodynamic performance. It is therefore concluded that the influence of the struts on the aerodynamic coefficients is negligible for all the operating conditions considered in this work. In particular, the aerodynamic coefficients and the flow characteristics depends more on the wing configuration than on the struts. This conclusion is important for future studies in the field, as the omission of struts greatly simplifies the meshing process and the mesh deformation in aeroelastic simulations.

# 6

## AEROELASTICITY OF A RAM-AIR KITE

*This chapter focuses on the computational approach to simulate the steady-state aeroelastic deformation of a ram-air kite for airborne wind energy applications. The approach is based on a computational fluid dynamics (CFD) solver that is two-way coupled with a finite element (FE) solver. All components of the framework, including the meshing tools and the coupling library, are available open-source. The flow around the wing is described by the steady-state Reynolds-averaged Navier-Stokes (RANS) equations closed by an SST turbulence model. The FE model of the cellular membrane structure includes a wrinkling model and uses dynamic relaxation to find the deformed steady-state shape. Each simulation comprises four distinct steps: (1) generating the FE mesh of the design geometry, (2) pre-inflating the wing, applying a uniform pressure on the inside, (3) generating the CFD mesh around the pre-inflated wing, and (4) activating the exterior flow and two-way coupling iterations. First, the results for the aerodynamics of the pre-inflated rigid ram-air wing are presented and compared to the leading edge inflatable (LEI) kite results of the previous chapter 5. Both wings are characterized by a high anhedral angle and low aspect ratio, which induce spanwise flows that reduce the aerodynamic performance. The comparison shows a better performance for the LEI wing, which can be attributed to its higher aspect ratio. The aeroelastic deformation of the ram-air wing further improves the aerodynamic performance, primarily because of the increasing camber, which in turn increases the lift force. A competing aeroelastic phenomenon is the formation of bumps near the leading edge, which increase the drag.*

### 6.1. INTRODUCTION

In this chapter, the focus is on flexible ram-air kite aerodynamics. The aerodynamic solver is coupled to the structural solver to account for the deformation. The problem is assumed to lead to a steady flow and deformation state. The flow inside the wing is not simulated, but constant internal pressure is assumed. A pre-simulation is carried

out with the structural solver to calculate the inflated shape of the wing. The present simulation model includes the entire three-dimensional shape of the kite, including the wing, bridle lines and a small part of the tether. Several angles of attack are studied by altering the trim of the bridle lines.

The chapter is organized as follows. Section 6.2 presents the geometry and how the numerical mesh is generated for the structural and aerodynamic model. Also, the Section describes how the bridle line is altered to change the powering setup. Section 6.3 presents the results of the chapter. Firstly, the rigidized ram-air wing results are presented and compared to the LEI kite wing. Subsequently, the results of the flexible wing are presented and compared to the rigid wing. Finally, the chapter is concluded in Section 6.4.

## 6.2. METHODOLOGY

The computational methodology comprises four successive steps. First, surface and line meshes are generated from the design geometry and bridle line system of the wing. In a second step, the inflated shape is determined in a pre-simulation, applying a uniform pressure inside the cellular membrane structure. In a third step, the volume mesh is generated around the surface mesh, and in the last step, the full aeroelastic problem is solved by two-way coupled iterations alternating between FE and CFD solvers until a steady converged wing shape, and flow field is reached. The design geometry of the wing and the bridle lines, as well as the surface mesh, are illustrated in 6.1. Key geometry parameters are listed in Table 6.1.

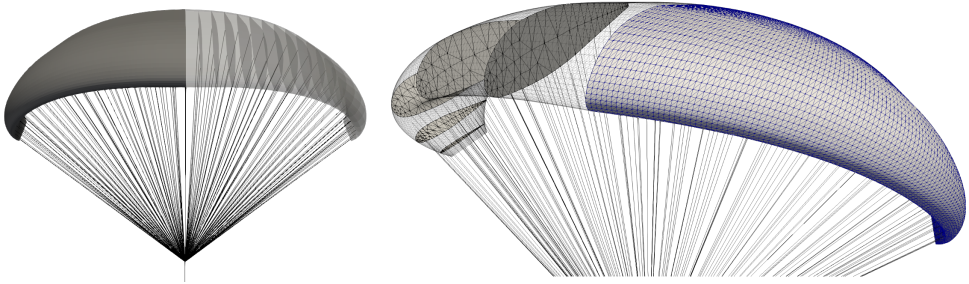


Figure 6.1: Initial design shape of the kite (left) and surface mesh discretizing the cellular wing structure, consisting of top and bottom skin and membrane ribs (right).

Table 6.1: Key geometry parameters of the kite.

Parameter	Symbol and definition	Value
Total surface area	$A$	160 m <sup>2</sup>
Projected surface area	$S$	125 m <sup>2</sup>
Projected span	$b$	15.2 m
Projected aspect ratio	$AR = b^2/S$	1.86
Maximum chord	$c_{\max}$	9.26 m

Table 6.2: Key parameters of the CFD simulation.

Parameter	Symbol and definition	Value
Reynolds number	$Re = Uc_{\max}/\nu$	$5 \times 10^6$
Dynamic pressure	$p_0 = \frac{1}{2}\rho_f U^2$	540 Pa
Turbulence intensity	$I$	2%
Eddy viscosity ratio	$\nu_t/\nu$	10

Table 6.3: Key parameters of the structural simulation.

Parameter	Symbol and definition	Value
Inflation over pressure	$p_i$	540 Pa
Membrane Young's modulus	$E_m \times t$	10 kN/m
Membrane Poisson's ratio	$\nu_m$	0.3
Bridle line Young's modulus	$E_c$	83.6 GPa
Bridle line diameter	$d$	2.5 mm

The geometry of the kite is illustrated in Figure 6.1. The wing is partitioned into 38 individual cells, defined by 39 ribs covered by a top and bottom skin membrane. The airfoil-shaped ribs define the aerodynamic shape of the wing, and accordingly, the wing geometry is generated by lofting through the rib airfoils. The top and the bottom skin of the wing and the ribs are made from the same membrane material. At the pressure side, each rib is supported by four bridle lines which converge into the main tether at the bridle point. The position of the bridle point relative to the wing and thus the lengths of the bridle lines control the trimming of the kite. Because of the expected low flow velocities, the flow inside the ram-air wing is not modeled, but a uniform inflation pressure is applied. Moreover, the main tether and the gravitational forces are not taken into account.

Firstly, a structured surface mesh is generated for the design shape of the wing with the Cassiopee pre- and post-processing tool [85]. The mesh is converted into a triangular mesh for the mem4py solver by splitting each quadrangle into two triangles. Additionally, the ribs are triangulated, which results in a total of 17504 triangle elements. The structural solver calculates the pre-inflated shape using the triangular mesh, and the computed displacements are mapped to the structured surface mesh. The structured surface mesh is further refined and stretched near the leading and the trailing edges to capture the high curvature for the requirements of the CFD simulation.

Secondly, the volume mesh close to the wing (red in Figure 6.2) is generated with the PyHyp [86] tool by extruding the surface mesh. PyHyp uses a hyperbolic extrusion algorithm for the extrusion, resulting in a nearly orthogonal mesh that is highly stretched in the wall-normal direction to accurately capture the boundary layer flow with a minimal cell count. The deformed CFD mesh is smoothed slightly at the ribs of the wing to prevent self-intersection. The mesh is extruded up to a thickness where the aspect ratio of the cells at the extrusion front are approximately unity. Thirdly, the rest of the domain is filled with a Cartesian mesh (gray in Figure 6.2) generated by the tool cfMesh, which is included in the OpenFOAM toolbox. The Cartesian mesh is refined near the wing and snapped at the interface of the boundary layer mesh with a layer of polyhedrons. The

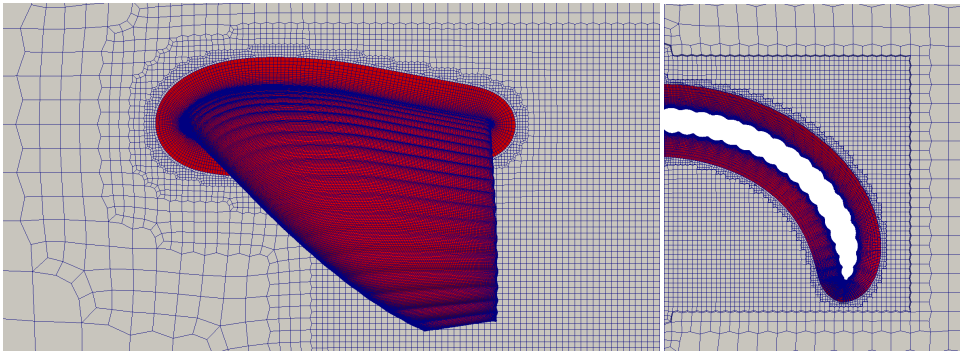


Figure 6.2: Volume mesh at the symmetry plane and at the the wing surface (left) and in streamwise direction at  $x/c = 0.75$  (right). The colors show the two different regions of the mesh.

two meshes are not conforming at the common interface, and therefore, OpenFOAM's arbitrary mesh interface (AMI) is used to transport the quantities from one mesh to the other. The final volume mesh has around 5.7 million cells.

In the aeroelastic coupling simulations, the angle of attack of the wing is controlled by trimming the bridle line system, moving the bridle point in the streamwise direction and adjusting the lengths of the bridle lines accordingly. The effect of the initial streamwise position  $\delta_x$  of the bridle point on the initial bridle geometry and the resulting equilibrium flight state is illustrated in Figure 6.3 for two different trim configurations. Trim configuration 1, with position  $\delta_{x,1}$  results in a low value  $\alpha_1$  of the steady-state angle of attack while configuration 2, with the bridle point shifted downstream to  $\delta_{x,2}$ , leads to a higher value  $\alpha_2$ .

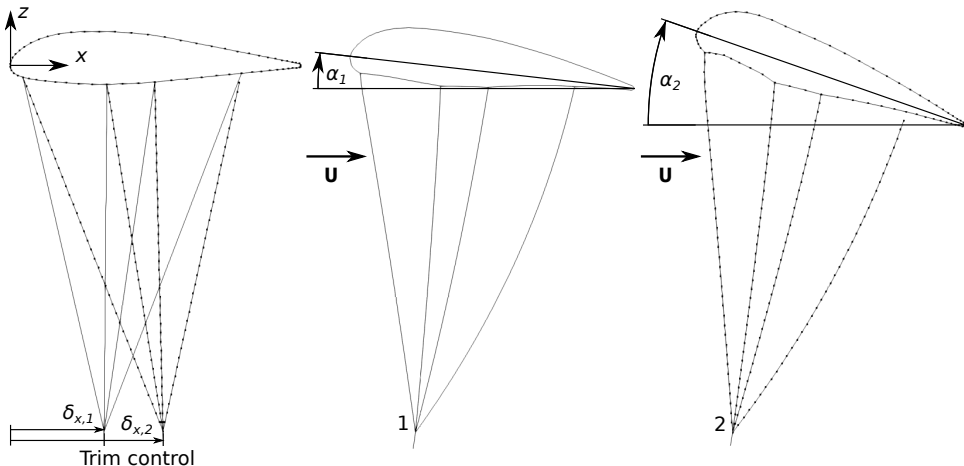


Figure 6.3: Trim configurations 1 and 2 for the design shape of the kite (left), and steady-state flight equilibrium (center & right) for the symmetry plane section of the kite.

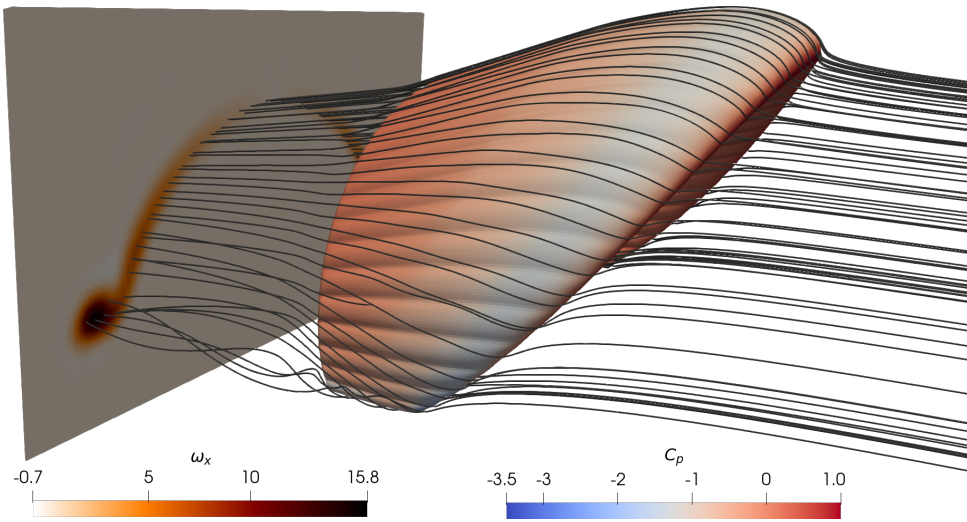


Figure 6.4: Streamlines along the suction side and vorticity component  $\omega_x$  on a plane normal to the streamwise direction at  $x = 1.5c$  and  $\alpha = 10^\circ$ .

## 6.3. RESULTS

The wing is first inflated, and the flow around this pre-inflated shape is computed. Subsequently, the aeroelastic results are presented and compared against the rigid pre-inflated shape results to isolate the effect of the flexibility.

### 6.3.1. RIGID PRE-INFLATED KITE

The inflated shape of the kite is calculated with the structural solver by imposing a uniform inflation pressure inside the wing. The cellular membrane structure balloons and forms the typical shape of a ram-air wing (Figure 6.1). The neighboring ribs move closer to each other, and the upper and lower skin billow outwards, which reduces the wingspan. The membranes are made from relatively stiff material with negligible stretch. The CFD simulations are carried out for this rigid pre-inflated shape.

Figure 6.4 shows streamlines along the suction side of the rigid pre-inflated wing and the vorticity component  $\omega_x$  in the wake flow. The low aspect ratio and the high anhedral angle of the wing lead to high spanwise flows and corresponding wingtip losses. The air flows from the high-pressure side to the suction side, which decreases the pressure difference between the two sides and reduces the lift force. On the upper skin of the wing, the spanwise flow pushes the streamlines towards the center of the wing. Additionally, wingtip vortices are formed in the wake, which increases the drag force. The vortices are illustrated by the twisted streamlines and the peak in vorticity downstream of the wingtip.

The simulation results are compared with the results obtained in the previous Chapter 5 for the flow around a fixed leading edge inflatable (LEI) kite wing at similar relative flow conditions. The lift and drag coefficients for both rigid wing shapes are shown in Figure 6.5. The aerodynamic performance of the LEI kite is consistently better across

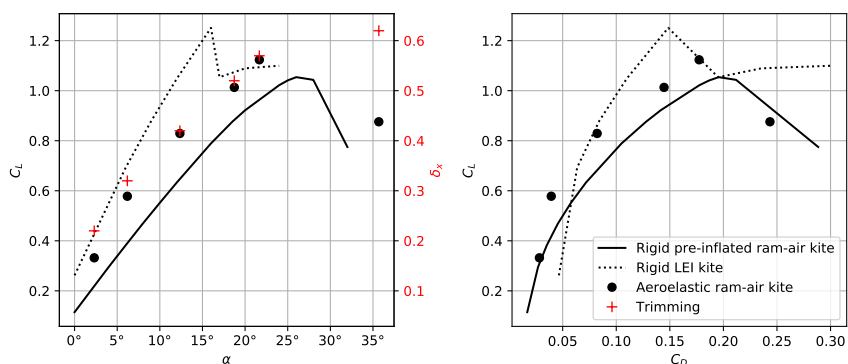


Figure 6.5: Lift coefficient as function of angle of attack (left) and drag polar (right) for the present ram-air kite and the LEI kite by Viré et al. [84].

the entire range of angles of attack. Figure 6.6 shows the front and planform views of the two different wings. Both wings have an anhedral angle of approximately  $90^\circ$  but the projected aspect ratio  $AR = 3.49$  of the LEI kite is nearly two times higher than the aspect ratio  $AR = 1.86$  of the ram-air kite. This geometric parameter generally increases the aerodynamic performance of a complete wing by decreasing the relative effect of the wingtip losses. This appears to be the main reason for the better aerodynamic performance of the LEI kite.

### 6.3.2. FLEXIBLE KITE

The two-way coupling iterations are continued until the computed aerodynamic coefficients converge on constant values. The coefficients after each coupling step are shown in Figure 6.7. The coupled solver requires approximately ten coupling steps to converge. A faster convergence could likely be achieved by using a more sophisticated coupling scheme than the explicit coupling scheme used in this work. The simulations are carried out on a high-performance computer using eight cores. Each simulation takes around 10 hours of wall time resulting in 80 hours of total process time. The results for the aeroelastic kite are included in the diagrams in Figure 6.5. The angle of attack is measured as the angle between the freestream velocity and the center chord line of the kite, as illustrated in Figure 6.3. The results show that the aerodynamic performance of the aeroelastic kite is better than that of the rigid pre-inflated kite. The lift is increased for the studied range of angle of attacks, and the drag is decreased for a given lift coefficient, which results in higher glide ratios, a common measure for the aerodynamic performance of a wing. However, in airborne wind energy systems, the bridle lines and the tether create additional drag, which favors high-lift wing designs to maintain a high overall aerodynamic performance of the system. The drag coefficients shown in this work show the wing drag contribution only without the bridle line or tether drag.

Figure 6.8 shows the cellular structure of the half wing, including the outlines of five representative ribs, for the pre-inflated and the aeroelastic kites, both at  $\alpha = 18.5^\circ$ . Note that the aeroelastic kite is moved back to its initial position for comparison. For high

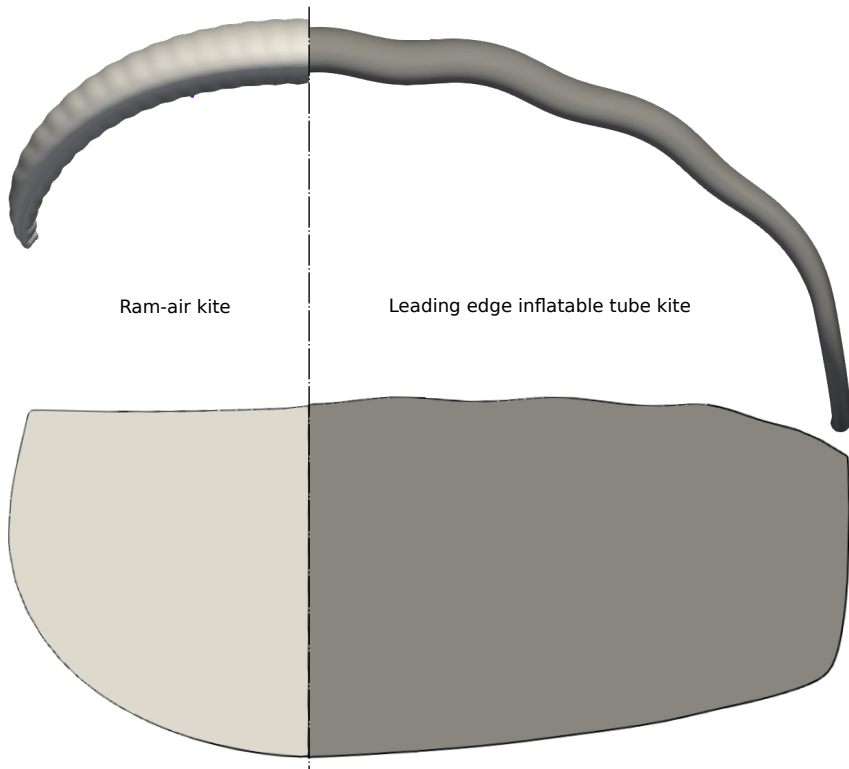


Figure 6.6: Front view (top) and planform view (bottom) of the pre-inflated ram-air kite investigated in this study and the LEI tube kite investigated by Viré et al. [84], fitted at the center chord.

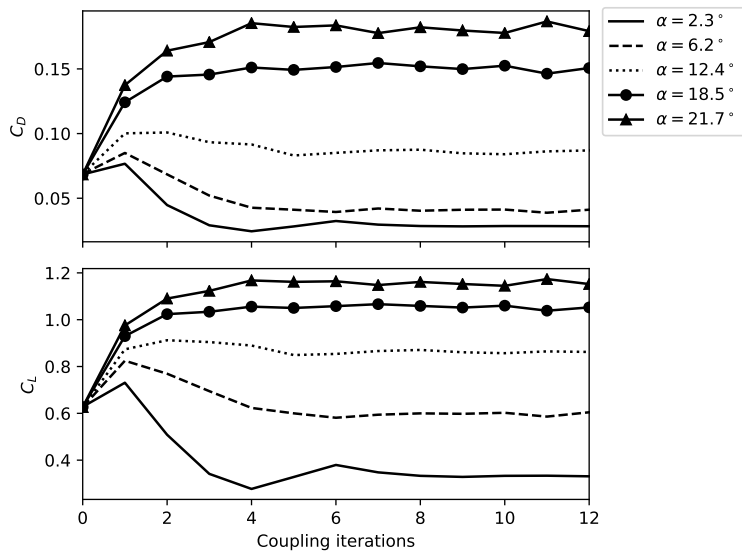


Figure 6.7: Evolution of the aerodynamic coefficients along the aeroelastic coupling iterations.

6

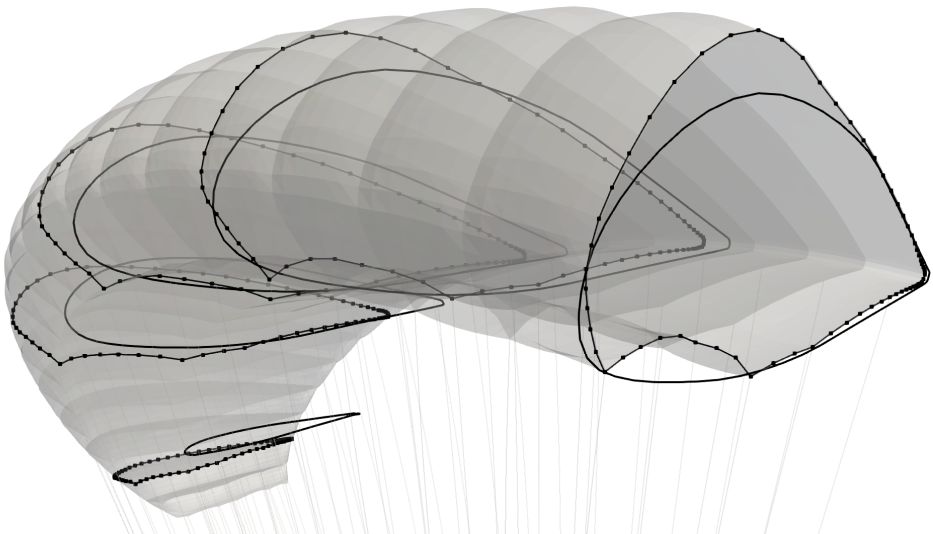


Figure 6.8: Half wing and five representative rib shapes for a steady-state angle of attack  $\alpha = 18.5^\circ$ . The rib shapes outlined by a solid line are for the pre-inflated rigid wing, while the rib shapes outlined by a line with dots are for the aeroelastic wing.

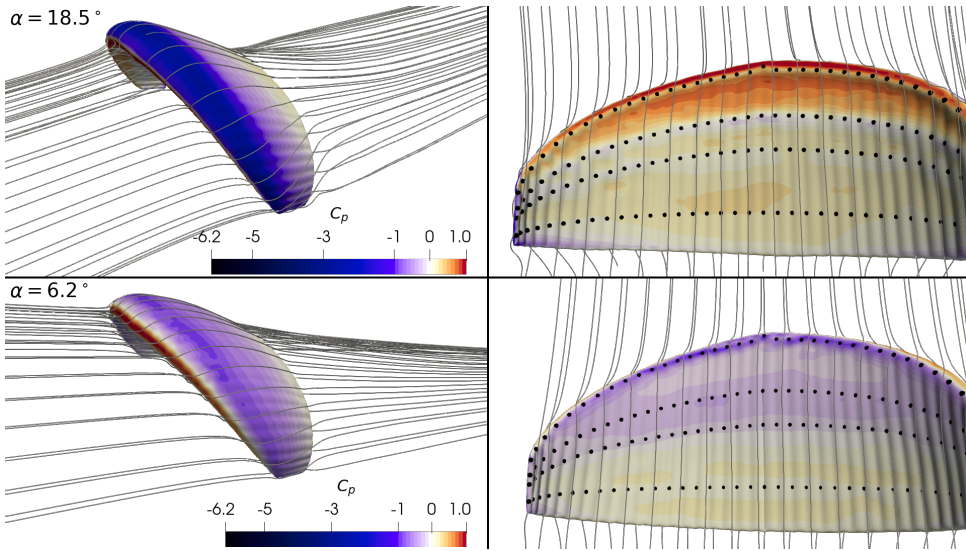


Figure 6.9: Streamlines along the wing and distribution of the surface pressure coefficient and bridle line attachment points on the wing surface.

angles of attack, the center of pressure moves towards the leading edge, which shifts the aerodynamic load to the front bridle lines of each rib. This effect can also be observed in Figure 6.3, which shows that the two front bridle lines are taut while the two rear lines are looser and, for this reason, deflected stronger by the aerodynamic drag. The high tension in the two front lines distorts the airfoil contour locally, generating two bumps at the line attachment points. The aerodynamic surface pressure indents the lower skin between the line attachments. On the other hand, the upper skin is pulled away by the high suction pressure. Moreover, a relatively planar region is formed at the stagnation region and the wingtips are bent forwards compared to the pre-inflated wing.

Figure 6.9 shows the distribution of the pressure coefficient on the wing surface and the streamlines along the wing for two different angles of attacks. Black dots indicate the bridle line attachment points on the lower skin. The pressure difference between the lower and upper skin of the wing increases with the angle of attack, resulting in a stronger crossflow on the upper skin, pushing the streamlines towards the center. The lower skin does not indicate a significant crossflow. However, the bridle line attachment points clearly trace a rapid change in the streamwise pressure coefficient.

The bumpy profile and the resulting change in the pressure coefficient can also be seen in Figure 6.10 which shows the rib contour and the pressure coefficient in the symmetry plane. For the high angle of attack ( $\alpha = 18.5^\circ$ ), the surface pressure exhibits two local minima at the two front bridle lines. A third minimum can be observed for the lower angles of attack, and the amplitudes exceed those for the high angle of attack. However, the pressure loss is approximately compensated by a higher pressure coefficient between the bumps. The increase in pulling force with the angle of attack is amplified by the increasing camber of the aeroelastic wing. On the other hand, an increasing angle of attack

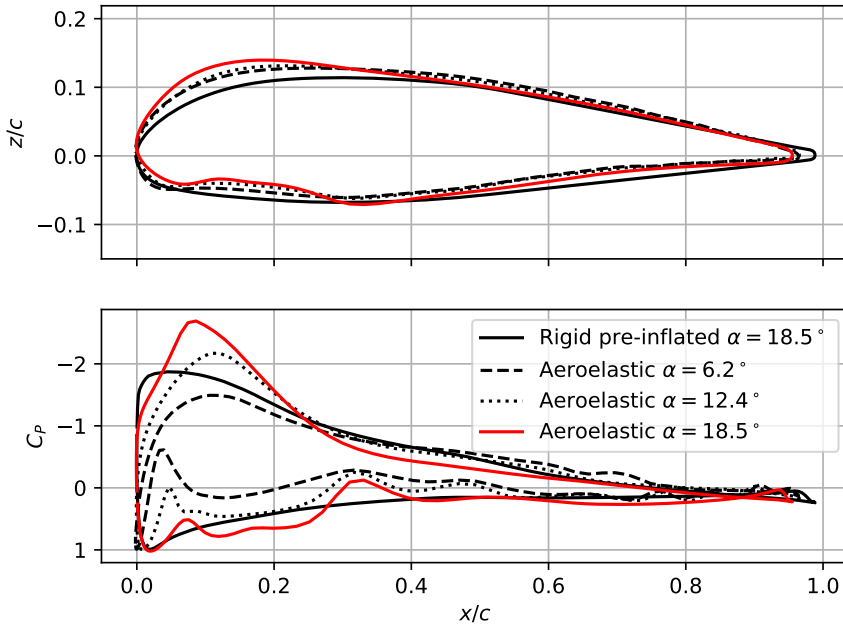


Figure 6.10: The symmetry plane wing contour (above) and the pressure coefficient distribution (below).

Table 6.4: Section aerodynamic coefficients at the symmetry plane rib

	$\alpha$	$c_d$	$c_l$
Rigid pre-inflated	$18.5^\circ$	0.13	0.87
Aeroelastic	$18.5^\circ$	0.15	0.93

gradually shifts the peak camber towards the leading edge. The section lift and drag coefficients are listed in Table 6.4 for  $\alpha = 18.5^\circ$ . We can conclude that the aeroelastic wing has higher lift and drag section coefficients than the rigid pre-inflated wing. The increased drag can be attributed to the bumpy lower skin, while the higher lift can be attributed to the increased camber.

## 6.4. CONCLUSIONS

This work presents a computational approach to simulate the steady-state aeroelastic deformation of a ram-air kite for airborne wind energy applications. The open-source toolchain uses the coupling library preCICE to combine the CFD solver OpenFOAM to simulate the flow around the wing with the FE solver mem4py to simulate the deformation of the membrane structure. The tools used for meshing the initial geometry are Cassiopee, PyHyp and cfMesh, while mesh deformation is handled with a radial basis function (RBF) method.

To assess the importance of aeroelasticity, a pre-inflated and then rigidized kite is compared with a flexible kite. The results show that the aeroelastic deformation of the cellular membrane structure and the bridle line system significantly affects the aerodynamic characteristics of the kite. The wing exhibits local deformation phenomena, such as billowing of the membrane or ballooning of the individual wing sections, as well as global deformation phenomena, such as spanwise contraction and bending. The flow field shows the typical flow phenomena for a wing with a low aspect ratio and a high anhedral angle, such as strong spanwise flow and distinct wingtip vortices.

The developed toolchain converges rapidly and is robust and capable of capturing the relevant physics of a wind energy harvesting ram-air wing. This steady-state simulation framework is considered a good compromise between model fidelity and computational cost and is thus suitable for efficiently analyzing and improving new kite designs. Future work could ensure mesh independence of results and perform a thorough validation. Also, partitioned coupling schemes, which are already included in the preCICE coupling tool, could be used to accelerate the convergence of the coupling iterations.



# 7

## CONCLUSIONS AND RECOMMENDATIONS

With the scientific evidence of the existence of climate change, there is an urgent need to lower our environmental footprint when producing and using energy. Wind energy is one of the key renewable energy sources for achieving the transition to a low carbon-emission economy. However, existing commercial wind turbines still contribute to material footprint with large and heavy structures for the foundation, tower and rotor. They are also subjected to wind variability at relatively low altitudes. The field of airborne wind energy (AWE) aims to tackle these limitations by producing wind energy at higher altitudes and with a much lower environmental footprint. AWE systems are still at an early stage of development, and better models are needed to make them more robust. In this thesis, the focus is on flexible membrane wings for which the aerodynamic performance is strongly coupled to the deformation of the wing. A steady-state aeroelastic methodology is implemented, which couples an aerodynamic solver to a structural mechanics solver. The methodology used to study the aerodynamics of a rigidized LEI kite airfoil and LEI kite wing, and a flexible ram-air kite

The main findings of this work and outlook for future research are summarised in this chapter.

### 7.1. MAIN FINDINGS OF THIS WORK

This work answers the following research questions.

#### Model assumptions

1. How much can the high-fidelity aeroelastic model for the membrane kites be simplified without sacrificing too much accuracy?

The model's primary assumption is that the membrane kite flying in an airborne wind system can be modeled with steady-state snapshots along the trajectory with-

out memory from the past. The steady-state simulations reduce the computational expense greatly, because no advancing in time is required. The CFD setup uses a RANS-based turbulence model to resolve the averaged flow field and model the chaotically varying turbulence. The structural mechanics model uses dynamic relaxation to calculate the steady-state.

The structural model is further simplified by considering the negligible bending stiffness of the membranes and lines. These tensile structures buckle immediately under compression. The structural model uses a two-dimensional membrane and one-dimensional cable finite elements with only translational degrees of freedom. The membranes wrinkle with compressive stresses, which is a small-scale phenomenon that requires a fine mesh to capture. Consequently, the membrane elements are augmented with a wrinkling model that models the wrinkles and resolves only the average mean surface without wrinkles. The smooth surface allows using a coarser mesh and therefore reduces the computational expense.

Additionally, this work shows that some geometrical details of the wing can be omitted. Simulations on a three-dimensional rigid LEI kite model with and without chordwise inflatable tubes on the pressure side showed that the effect of the tubes on the flow is only local. The aerodynamic forces have minimal dependency on the struts, and therefore they can be left out, which greatly simplifies the mesh around the wing.

2. What is the right balance of fidelity between the aerodynamic and the structure model for membrane kites?

The natural representation of membrane structures is a surface model, such as the membrane elements in the present work. Also, the body-conforming CFD model is a natural way to represent and couple the structure through a no-slip boundary condition. Both solvers operate in steady-state mode, which significantly reduces the computation time. The ram-air simulations in Chapter 7 show that the steady-state evaluations of the structural model are approximately eight times faster than the aerodynamic model. However, the aerodynamic model runs parallel, and therefore the computational times of the models can be balanced by using parallel architectures.

### Model robustness

1. Can the time-consuming CFD volume mesh generation around the membrane wing be automated?

The main overhead for using the present aeroelastic model is mesh generation, a well-known problem in computational fluid dynamics. A highly stretched boundary layer mesh is required to capture the steep velocity gradient close to the body. The shape of the membrane kites poses a challenge with the bumpy surface and unconventional wingtip. This work found automated strategies for leading edge inflatable and ram-air kite designs. Nevertheless, expert knowledge is needed to implement a new mesh generation strategy for a new kite design. A high-quality mesh is a prerequisite for the aeroelastic model because it increases the robustness of the model and speeds up the convergence.

2. Is there a robust way to deform the CFD mesh around the highly flexible membrane kite?

The volumetric mesh around the kite deforms with the kite in the present body-conforming aeroelastic simulations. An initial high-quality mesh helps with the mesh deformation, but still, the conventional mesh deformation methods in OpenFOAM fail in the regions of high curvature and highly stretched cells. Consequently, another method based on the radial basis function and the greedy point selection is employed, which proves to be robust and efficient. Moreover, the average surface representation of the wrinkling model helps to eliminate the unnecessary wiggles that could cause the mesh deformation to fail.

3. Is it possible to build a robust aeroelastic model for membrane kites that can be used as a part of the kite design process?

With the proper CFD mesh building strategy, the developed toolchain converges rapidly, is robust, and captures the relevant physics of membrane kites. The steady-state simulation framework is considered a good compromise between model fidelity and computational cost and is thus suitable for analyzing and improving new kite designs.

## Physics

1. What kind of flow phenomena is observed around the unique wing planform of the membrane kites, and how does it affect the practical use of kites in AWE?

The structural reinforcements required for membrane traction kites result in a non-smooth surface. The bumpy surface of the wings causes the flow to separate in several locations, which is particularly prominent behind the leading edge tube of the leading-edge inflatable kite wings. The flow forms recirculation zones behind the tubes, and the size of the zones depends on the flight conditions. However, the chordwise tubes only have local flow effects and do not significantly impact the wing's aerodynamic efficiency. Nevertheless, this work shows that the unconventional airfoil has a decent aerodynamic performance. The structural integrity has a significant impact on the wing planform of the membrane kite. The low aspect ratio and the high anhedral cause relatively strong three-dimensional flows that dramatically reduce the aerodynamic efficiency of the idealistic two-dimensional performance. However, those characteristics allow fast maneuvering and the low-weight wing to resist the high loading.

The simulations show a strong dependency on the transition model. The conventional RANS models assume that the boundary layers transition immediately to a fully turbulent state without the transition model. The results of the transition model agree well with the experiment in a wind tunnel. The transition significantly affects the aerodynamic forces even with relatively high Reynolds numbers. However, in the actual disturbed operating conditions, the boundary layer transition plays a minor role because of the rough texture of the membrane with many seams and the wind turbulence.

2. How does the flexible structure of membrane kites affect the aerodynamic efficiency?

Although the tensile design of a membrane wing decreases the conventional measure of aerodynamic efficiency, glide ratio, the flexible design also has advantages. The lightweight wing is expected to have a lower cut-in speed, which increases the capacity factor of the system and the revenue of the energy in a wind energy saturated market. The flexible airfoil automatically adapts to the incoming flow in several ways. For instance, the peak camber moves with the angle of attack and therefore extends the valid range of angles of attack and improves the aerodynamic performance.

3. Can the steady-state model capture the recirculation zone and the flow separation around the non-smooth wing surface?

The two-dimensional simulations on the LEI kite airfoil in Chapter 4 agree well with the experimental results, even with large angles of attack, which indicates that the model can capture the effect of separated flows. However, a more elaborate validation study with higher Reynolds numbers is required because it is well known that CFD with the RANS modeling approach becomes inaccurate for large-scale separated flows.

## 7.2. RECOMMENDATIONS FOR FUTURE RESEARCH

The present work showed several verification and validation cases for the parts of the implemented methodology. However, future work should extend the cases to the full framework. The first step would be to find a test case with minimal complexity but still relevant to the kite aeroelasticity. One option could be an inflatable membrane wing section, which was also explored as a sidetrack in the present work [87]. The convergence of the framework could be accelerated further by using dynamic under-relaxation or quasi-Newton coupling schemes, which are already available in the preCICE coupling tool used in the present work. The coupling schemes could decrease the number of required coupling iterations. Also, finding a good end criterion for the coupled simulation could be assessed to find a good balance between accuracy to computation cost.

The aeroelastic model was used to simulate a flexible ram-air kite. The simulations on the LEI kite focused only on a rigidized wing, and future work could extend the work on a flexible kite. The structural model for the LEI kite requires further consideration, mainly on how to model the inflatable beams. The most straightforward option could be to model the beams with the same membrane elements as the canopy, but a beam element model could be a more robust and efficient approach. In both cases, the fluid model does not match the structural model at the interface. With the membrane elements, the fluid mesh does not match the structure mesh around the tubes because of the fillet required to generate the boundary layer mesh. However, the effect of the fillet is expected to be minimal because the pressure is rather constant for separated flow, and a simple mapping scheme could suffice. The mapping of displacements may require special consideration to retain the high quality of the grid. In a beam model, the forces have to be lumped from the surface to the line and the displacements from the line to the surface.

In this work, the power setting for the aeroelastic kite is varied by trimming the bridle line system. Future work could vary the wind speed and study the effect on aerodynamic performance and the shape of the wing. The present work shows the impact of asymmetric inflow for a rigid membrane kite wing by changing the sideslip angle. Future work could extend the study to the cornering of the kite by trimming the steering lines. The steady-state model would require an axisymmetric description of the problem, or a transient model could be used.



# REFERENCES

1. Arrhenius, S.: On the Influence of Carbonic Acid in the Air upon the Temperature of the Earth. Publications of the Astronomical Society of the Pacific **9**, 14 (1897)
2. Agency, I. R. E.: Renewable Power Generation Costs in 2020, 2021. [https://www.irena.org/-/media/Files/IRENA/Agency/Publication/2021/Jun/IRENA\\_Power\\_Generation\\_Costs\\_2020.pdf](https://www.irena.org/-/media/Files/IRENA/Agency/Publication/2021/Jun/IRENA_Power_Generation_Costs_2020.pdf)
3. BP: Statistical Review of World Energy 2021, 2021. <https://www.bp.com/en/global/corporate/energy-economics/statistical-review-of-world-energy.html>
4. Tans, P.: Trends in Atmospheric Carbon Dioxide. <https://gml.noaa.gov/ccgg/trends/>. Accessed Apr 5, 2022
5. Keeling, R.: Scripps CO2 Program. <scrippsco2.ucsd.edu/>. Accessed Apr 5, 2022
6. Climate Change, T. I. P. on: IPCC Sixth Assessment Report. <https://www.ipcc.ch/report/ar6/wg3/>. Accessed Apr 5, 2022
7. Malz, E.: Airborne Wind Energy - to fly or not to fly? Ph.D. Thesis, Chalmers University of Technology, 2020
8. Fechner, U.: A Methodology for the Design of Kite-Power Control Systems. Ph.D. Thesis, Delft University of Technology, Nov 23, 2016. doi: [10.4233/uuid:85efaf4c-9dce-4111-bc91-7171b9da4b77](https://doi.org/10.4233/uuid:85efaf4c-9dce-4111-bc91-7171b9da4b77)
9. Schmehl, R., Fechner, U.: KitePower Data 2010–15. TU Delft (2020)
10. SkySails: <https://www.skysails-group.com/media-yacht-division.html>. Accessed: 30 October 2020
11. Flysurfer: <https://flysurfer.com/project/peak4/>. Accessed: 30 October 2020
12. FLYSURFER Kiteboarding: Flysurfer products. <https://flysurfer.com/products/>. Accessed June 1, 2020
13. Verheul, R., Breukels, J., Ockels, W.: Material selection and joining methods for the purpose of a high-altitude inflatable kite. 50th AIAA/ASME/ASCE/AHS/ASC Structures, Structural Dynamics, and Materials Conference, Palm Springs, California, USA, 4-7 May, 2009 (2009). doi: [10.2514/6.2009-2338](https://doi.org/10.2514/6.2009-2338)
14. Breukels, J.: An Engineering Methodology for Kite Design. Ph.D. Thesis, Delft University of Technology, Jan 21, 2011. <http://resolver.tudelft.nl/uuid:cdece38a-1f13-47cc-b277-ed64fdda7cdf>
15. Gohl, F., Luchsinger, R. H.: Simulation Based Wing Design for Kite Power. In: Ahrens, U., Diehl, M., Schmehl, R. (eds.) Airborne Wind Energy, Green Energy and Technology, Chap. 18, pp. 325–338. Springer, Berlin Heidelberg (2013). doi: [10.1007/978-3-642-39965-7\\_18](https://doi.org/10.1007/978-3-642-39965-7_18)
16. Maughmer, M. D.: A comparison of the aerodynamic characteristics of eight sailing airfoil sections. In: Proceedings of the 3rd International Symposium on the Science and Technology of Low Speed and Motorless Flight, pp. 155–176, NASA Langley Research Center, Hampton, VA, USA, Mar 29–30, 1979

17. Dunker, S.: Ram-Air Wing Design Considerations for Airborne Wind Energy. In: Ahrens, U., Diehl, M., Schmehl, R. (eds.) *Airborne Wind Energy, Green Energy and Technology*, Chap. 31, pp. 517–546. Springer, Berlin Heidelberg (2013). doi: [10.1007/978-3-642-39965-7\\_31](https://doi.org/10.1007/978-3-642-39965-7_31)
18. Paulig, X., Bungart, M., Specht, B.: Conceptual Design of Textile Kites Considering Overall System Performance. In: Ahrens, U., Diehl, M., Schmehl, R. (eds.) *Airborne Wind Energy, Green Energy and Technology*, Chap. 32, pp. 547–562. Springer, Berlin Heidelberg (2013). doi: [10.1007/978-3-642-39965-7\\_32](https://doi.org/10.1007/978-3-642-39965-7_32)
19. Fogell, N. A.: Fluid-structure interaction simulations of the inflated shape of ram-air parachutes. PhD thesis, Imperial College London, 2014
20. Ozone: <https://ozonekites.com/products/land-snow-kites/explore-v2/>. Accessed: 30 October 2020
21. Coenen, R.: Single Skin Kite Airfoil Optimization for AWES. M.Sc.Thesis, Delft University of Technology, Dec 21, 2018
22. Wachter, A. de: Deformation and Aerodynamic Performance of a Ram-Air Wing. M.Sc.Thesis, Delft University of Technology, 2008. <http://resolver.tudelft.nl/uuid:786e3395-4590-4755-829f-51283a8df3d2>
23. Bungart, M.: Fluid-Struktur Kopplung an einem RAM-Air-Kiteschirm. M.Sc.Thesis, University of Stuttgart, 2009
24. Terink, E., Breukels, J., Schmehl, R., Ockels, W.: Flight Dynamics and Stability of a Tethered Inflatable Kiteplane. *Journal of Aircraft* **48**(2), 503–513 (2011). doi: [10.2514/1.C031108](https://doi.org/10.2514/1.C031108)
25. Demkowicz, P.: Numerical analysis of the flow past a leading edge inflatable kite wing using a correlation-based transition model. M.Sc.Thesis, Delft University of Technology, 2019. <http://resolver.tudelft.nl/uuid:c53aa605-1b2e-47a7-b991-c1917d7463b4>
26. Fagianio, L., Huynh, K., Bamieh, B., Khammash, M.: On sensor fusion for airborne wind energy systems. *IEEE Transactions on Control Systems Technology* **22**(3), 930–943 (2014). doi: [10.1109/TCST.2013.2269865](https://doi.org/10.1109/TCST.2013.2269865)
27. Jehle, C., Schmehl, R.: Applied Tracking Control for Kite Power Systems. *Journal of Guidance, Control, and Dynamics* **37**(4), 1211–1222 (2014). doi: [10.2514/1.62380](https://doi.org/10.2514/1.62380)
28. Roullier, A.: Experimental analysis of a kite system's dynamics. M.Sc.Thesis, EPFL, 2020
29. Bosch, A., Schmehl, R., Tiso, P., Rixen, D.: Dynamic nonlinear aeroelastic model of a kite for power generation. *Journal of Guidance, Control and Dynamics* **37**(5), 1426–1436 (2014). doi: [10.2514/1.G000545](https://doi.org/10.2514/1.G000545)
30. Boer, R. G. den: Low speed aerodynamic characteristics of a two-dimensional sail wing with adjustable slack of the sail. Report LR-307, Delft University of Technology, Delft, Netherlands, 1980. <http://resolver.tudelft.nl/uuid:18ae2cc6-434e-49c8-9296-d3fa450850a5>
31. Leuthold, R. C.: Multiple-Wake Vortex Lattice Method for Membrane Wing Kites. M.Sc.Thesis, Delft University of Technology, Dec 15, 2015. <http://resolver.tudelft.nl/uuid:4c2f34c2-d465-491a-aa64-d991978fedf4>
32. Fink, M. P.: Full-scale investigation of the aerodynamic characteristics of a model employing a sailing concept. Technical Report NASA TN D-4062, NASA Langley Research Center, Hampton, VA, USA, July 1967. <http://hdl.handle.net/2027/uiug.30112106870097>
33. Kroo, I.: Aerodynamics, Aeroelasticity, and Stability of Hang Gliders - Experimental Results. Technical Report NASA-TM-81269. <http://hdl.handle.net/2060/19810015490>, NASA Ames Research Center, Moffett Field, CA, USA, 1981

34. Maughmer, M.: Optimization and Characteristics of a Sailwing Windmill Rotor. In: Princeton University AMS Report, No. 1297, (1976)
35. Jalbert, D. C.: Multi-cell glide canopy parachute. 3131894, 1964
36. Ware, G. M., Hassell, J. L.: Wind-tunnel investigation of ram-air-inflated all-flexible wings of aspect ratios 1.0 to 3.0. NASA TM SX-1923, NASA Langley Research Center, Hampton, VA, USA, 1969
37. Nicolaidis, J. D.: Parafoil Wind Tunnel Tests. Technical Report AFFDL-TR- 70-146, Air Force Flight Dynamics Laboratory, 1971
38. Boer, R. G. den: Numerical and experimental investigation of the aerodynamics of double membrane sailwing airfoil sections. LR-345, Delft University of Technology, Delft, Netherlands, 1982. <http://resolver.tudelft.nl/uuid:d7b421a7-e1f4-4b3c-a053-969f5cab1920>
39. Dadd, G. M., Hudson, D. A., Sheno, R. A.: Comparison of two kite force models with experiment. *Journal of Aircraft* **47**(1), 212–224 (2010). doi: [10.2514/1.44738](https://doi.org/10.2514/1.44738)
40. Python, B.: Methodology improvement for performance assessment of pumping kite power wing. M.Sc.Thesis, Delft University of Technology and Ecole Polytechnique Fédérale de Lausanne, 2017
41. Hummel, J., Göhlich, D., Schmehl, R.: Automatic Measurement and Characterization of the Dynamic Measurands of Tethered Flexible Wings. *Wind Energy Science* **4**(1), 41–55 (2019). doi: [10.5194/wes-4-41-2019](https://doi.org/10.5194/wes-4-41-2019)
42. Rushdi, M., Rushdi, A., Dief, T., Halawa, A., Yoshida, S., Schmehl, R.: Power Prediction of Airborne Wind Energy Systems Using Multivariate Machine Learning. *Energies* **13**(9) (2020). doi: [10.3390/en13092367](https://doi.org/10.3390/en13092367)
43. Oehler, J., Reijen, M. van, Schmehl, R.: Experimental investigation of soft kite performance during turning maneuvers. *Journal of Physics: Conference Series* **1037**(5), 052004 (2018). doi: [10.1088/1742-6596/1037/5/052004](https://doi.org/10.1088/1742-6596/1037/5/052004)
44. Oehler, J., Schmehl, R.: Aerodynamic characterization of a soft kite by in situ flow measurement. *Wind Energy Science* **4**(1), 1–21 (2019). doi: [10.5194/wes-4-1-2019](https://doi.org/10.5194/wes-4-1-2019)
45. Leloup, R.: Modelling approach and numerical tool development for kite performance assessment and mechanical design; application to vessels auxiliary propulsion. Ph.D. Thesis, ENSTA Bretagne/University of Western Brittany, 2014
46. Dupont, C.: Modeling with consideration of the fluid-structure interaction of the behavior under load of a kite for auxiliary traction of ships. PhD thesis, ENSTA Bretagne, 2018
47. Gaunaa, M., Paralta Carqueija, P. E., Réthoré, P.-E. M., Sørensen, N. N.: A Computationally Efficient Method for Determining the Aerodynamic Performance of Kites for Wind Energy Applications. In: Proceedings of the European Wind Energy Association Conference, Brussels, Belgium, Mar 14–17, 2011. <http://findit.dtu.dk/en/catalog/181771316>
48. Deaves, M. E.: An Investigation of the Non-Linear 3D Flow Effects Relevant for Leading Edge Inflatable Kites. M.Sc.Thesis, Delft University of Technology, Sept 1, 2015. <http://resolver.tudelft.nl/uuid:ccb56154-0b70-4a41-8223-24b0f8d145c5>
49. Fogell, N. A., Iannucci, L., Bergeron, K.: Fluid-Structure Interaction Simulation study of a Semi-Rigid Ram-Air Parachute Model. In: 24th AIAA Aerodynamic Decelerator Systems Technology Conference, (2017). doi: [10.2514/6.2017-3547](https://doi.org/10.2514/6.2017-3547)
50. Piquee, J., López Canalejo, I., Breitsamter, C., Wüchner, R., Bletzinger, K.-U.: Aerodynamic analysis of a generic wing featuring an elasto-flexible lifting surface. *Advances in Aerodynamics* **1**(20) (2019)

51. Sachdeva, S.: Impact of turning-induced shape deformations on aerodynamic performance of leading edge inflatable kites. M.Sc.Thesis, Delft University of Technology, 2017
52. Lebesque, G.: Numerically modelling the three-dimensional flow field around a complex leading edge inflatable wing geometry. M.Sc.Thesis, Delft University of Technology, 2020. <http://resolver.tudelft.nl/uuid:f0bc8a1e-088d-49c5-9b77-ebf9e31cf58b>
53. OpenFOAM: <https://www.openfoam.com/>. Accessed: 14 August 2018
54. Menter, F.: Zonal Two Equation Kappa-Omega Turbulence Models for Aerodynamic Flows. In: Proceedings of the 23rd Fluid Dynamics, Plasmadynamics, and Lasers Conference, AIAA Paper 93-2906, (1993). doi: [10.2514/6.1993-2906](https://doi.org/10.2514/6.1993-2906)
55. Jones, W., Launder, B.: The prediction of laminarization with a two-equation model of turbulence. *International Journal of Heat and Mass Transfer* **15**(2), 301–314 (1972). doi: [10.1016/0017-9310\(72\)90076-2](https://doi.org/10.1016/0017-9310(72)90076-2)
56. Wilcox, D.: Reassessment of the Scale-Determining Equation for Advanced Turbulence Models. *AIAA Journal* **26**(11), 1299–1310 (1988). doi: [10.2514/3.10041](https://doi.org/10.2514/3.10041)
57. Menter, F., Kuntz, M., Langtry, R.: Ten Years of Industrial Experience with the SST Turbulence Model. In: Hanjalic, K., Nagano, Y., Tummers, M. (eds.) *Turbulence, Heat and Mass Transfer 4*, pp. 625–632. Begell House, Inc. (2003)
58. Menter, E., Esch, T.: Elements of Industrial Heat Transfer Prediction. In: Proceedings of the 16th Brazilian Congress of Mechanical Engineering (COBEM), pp. 117–127, Uberlandia, Brazil, Nov 2001
59. Rumsey, C.: Turbulence Modeling Resource, NASA Langley Research Center, <https://turbmodels.larc.nasa.gov/sst.html>. Accessed: 14 August 2018
60. Langtry, R., Menter, F., Likki, S., Suzen, Y., Huang, P., Völker, S.: A Correlation-Based Transition Model Using Local Variables—Part II: Test Cases and Industrial Applications. *Journal of Turbomachinery* **128**(3), 423–434 (2006). doi: [10.1115/1.2184353](https://doi.org/10.1115/1.2184353)
61. Saric, W., Reed, H., White, E.: STABILITY AND TRANSITION OF THREE-DIMENSIONAL BOUNDARY LAYERS. *Annual Review of Fluid Mechanics* **35**(1), 413–440 (2003). doi: [10.1146/annurev.fluid.35.101101.161045](https://doi.org/10.1146/annurev.fluid.35.101101.161045)
62. Reshotko, E.: Boundary-layer instability, transition and control. In: Proceedings of the 32nd Aerospace Sciences Meeting and Exhibit, AIAA Paper 94-0001, pp. 117–127, Reno, NV, USA, Jan 1994. doi: [10.2514/6.1994-1](https://doi.org/10.2514/6.1994-1)
63. Langtry, R., Menter, F.: Correlation-Based Transition Modeling for Unstructured Parallelized Computational Fluid Dynamics Codes. *AIAA Journal* **47**(12), 2894–2906 (2009). doi: [10.2514/1.42362](https://doi.org/10.2514/1.42362)
64. Medida, S., Baeder, J.: Numerical Prediction of Static and Dynamic Stall Phenomena using the  $\gamma - \bar{Re}_{\theta t}$  Transition Model. In: American Helicopter Society 67th Annual Forum, Virginia Beach, VA, USA (2011)
65. Zheng, Z., Lei, J.: Application of the  $\gamma - Re_{\theta}$  Transition Model to Simulations of the Flow Past a Circular Cylinder. *Flow, Turbulence and Combustion* **97**(2), 401–426 (2016). doi: [10.1007/s10494-016-9706-9](https://doi.org/10.1007/s10494-016-9706-9)
66. Thedens, P.: <https://github.com/pthedens/mem4py>. Accessed: 18 June 2020
67. Barnes, M. R.: Form finding and analysis of tension structures by dynamic relaxation. *International journal of space structures* **14**(2), 89–104 (1999)

68. Barnes, M. R.: Form finding and analysis of tension space structures by dynamic relaxation. Ph.D. Thesis, City University London, 1977
69. Bungartz, H., Lindner, F., Gatzhammer, B., Mehl, M., Scheufele, K., Shukaev, A., Uekermann, B.: preCICE – A fully parallel library for multi-physics surface coupling. *Computers and Fluids* **141**, 250–258 (2016). doi: [10.1016/j.compfluid.2016.04.003](https://doi.org/10.1016/j.compfluid.2016.04.003)
70. Jasak, H., Tuković, Ž.: Automatic Mesh Motion for the Unstructured Finite Volume Method. *Transactions of FAMENA* **30**(2) (2006)
71. Selim, M., Koomullil, R.: Mesh Deformation Approaches – A Survey. *Journal of Physical Mathematics* **2**(7) (2016)
72. Rendall, T., Allen, C.: Efficient Mesh Motion Using Radial Basis Functions With Data Reduction Algorithms. *Journal of Computational Physics* **228**(17), 6231–6249 (2009)
73. Chan, W. M., Steger, J. L.: Enhancements of a three-dimensional hyperbolic grid generation scheme. *Applied Mathematics and Computation* **51**(2), 181–205 (1992). doi: [https://doi.org/10.1016/0096-3003\(92\)90073-A](https://doi.org/10.1016/0096-3003(92)90073-A)
74. Pointwise: T-REX. <http://www.pointwise.com/doc/user-manual/grid/solve/unstructured-blocks/t-rex.html>. Accessed Jan 7, 2020
75. Blom, D.: <https://github.com/davidsblom/FOAM-FSI>. Accessed: 18 June 2020
76. Folkersma, M.: <https://github.com/mfolkersma/RBFMeshDeformation>. Accessed: 22 June 2020
77. Jarasjarungkiat, A., Wüchner, R., Bletzinger, K.-U.: A wrinkling model based on material modification for isotropic and orthotropic membranes. *Computer Methods in Applied Mechanics and Engineering* **197**(6-8), 773–788 (2008)
78. Chourdakis, G., Risseeuw, D.: <https://github.com/precice/openfoam-adapter>. Accessed: 18 June 2020
79. Valdés, G.: Nonlinear Analysis of Orthotropic Membrane and Shell Structures Including Fluid-Structure Interaction. PhD thesis, Universitat Politècnica de Catalunya, 2007
80. Mok, D.: Partitionierte Lösungsansätze in der Strukturmechanik und der Fluid-Struktur-Interaktion. PhD thesis, Universität Stuttgart, 2001
81. Folkersma, M., Schmehl, R., Viré, A.: Boundary layer transition modeling on leading edge inflatable kite airfoils. *Wind Energy* **22**(7), 908–921 (2019). doi: [10.1002/we.2329](https://doi.org/10.1002/we.2329)
82. Bruining, A.: Aerodynamic characteristics of a curved plate airfoil section at Reynolds numbers 60.000 and 100.000 and angles of attack from -10 to +90 Degrees. Report LR-281. <http://resolver.tudelft.nl/uuid:6b92442a-01f7-4b7c-8d53-c4f10720ff3e>, Delft University of Technology, Delft, Netherlands, 1979
83. Bot, P., Rabaud, M., Thomas, G., Lombardi, A., Leuret, C.: Sharp Transition in the Lift Force of a Fluid Flowing Past Nonsymmetrical Obstacles: Evidence for a Lift Crisis in the Drag Crisis Regime. *Physical Review Letters* **117**(23), 234501 (2016). doi: [10.1103/PhysRevLett.117.234501](https://doi.org/10.1103/PhysRevLett.117.234501)
84. Viré, A., Demkowicz, P., Folkersma, M., Roullier, A., Schmehl, R.: Reynolds-averaged Navier-Stokes simulations for flow past a leading edge inflatable wing for airborne wind energy applications. In: Proceedings of the Torque 2020 conference, Delft, The Netherlands, May 27–29, 2020
85. Benoit, C., Peron, S., S., L.: Cassiopee: a CFD pre- and post-processing tool. *Aerospace Science and Technology* **45**, 272–283 (2015)

86. pyHyp: <https://github.com/mdolab/pyhyp>. Accessed: 02 March 2020
87. Folkersma, M., Thedens, P., Schmehl, R., Vire, A.: Fluid-Structure Interaction of Inflatable Wing Section. In: Proceedings of the 8th International Conference on Coupled Problems in Science and Engineering, (2019)

# ACKNOWLEDGEMENTS

First, I want to thank my promoter, Gerard van Bussel and my co-promoters Roland Schmehl and Axelle Vire, who allowed me to do this exciting project and guided me through it. Next, I want to thank Sylvia Willems for the support along the way. Furthermore, I am grateful to all the committee members for accepting our invitation and assessing my dissertation. I also want to thank Paul Thedens for developing the structural solver, Turo Välikangas for the CFD-related collaboration and Daan Hof for helping me with the Dutch translation. Also, I want to thank my colleagues at Whiffle, who gave me the last push to finish the project.

During the project, I met many wonderful colleagues who kept me sane. Thanks to the afternoon walking team, Julia, Carlos, Mark, Pranav, Christopher and Jigna, for the intriguing conversations. Thanks to the AWESCO team and particularly the Delft section, Sebastian, Ashwin, Paul and Thomas, for the fascinating gatherings all around Europe. Thanks to the card gang, Ashim, Navi, Zi and Vinit, for the exciting games. Thanks to Juan, Ye, Chris, Wei, Bedassa, Shariff, Edoardo and Emanuel for your friendship and the discussions.

Special thanks go to my flatmates in The Netherlands, Rui, Alina, Emma, Jens and Johannes, whose support was essential on the way. Finally, I would like to thank my family in Finland, who let me explore the world and always supported my decisions.



# LIST OF PUBLICATIONS

1. A. Viré, G. Lebesque, **M. Folkersma**, R. Schmehl. "Effect of Chordwise Struts and Misaligned Flow on the Aerodynamic Performance of a Leading-Edge Inflatable Wing", *Energies* 15(4), 1450, 2022.
2. T. Välikangas, **M. Folkersma**, M. Dal Maso, T. Keskitalo, P. Peltonen, V. Vuorinen. "Parametric CFD study for finding the optimal tube arrangement of a fin-and-tube heat exchanger with plain fins in a marine environment", *Applied Thermal Engineering* 200(10):117642, 2022.
3. P. Thedens, **M. Folkersma**, A. Viré, R. Schmehl. "Computational simulation of the aeroelastic behavior of a ram-air kite for airborne wind energy applications", *Wind Energy Science Conference*, 2020.
4. **M. Folkersma**, R. Schmehl, A. Viré. "Steady-state aeroelasticity of a ram-air wing for airborne wind energy applications", *Journal of Physics Conference Series* 1618(3):32018, 2020.
5. A. Viré, P. Demkowicz, **M. Folkersma**, A. Roullier, R. Schmehl. "Reynolds-averaged Navier-Stokes simulations of the flow past a leading edge inflatable wing for airborne wind energy applications", *Journal of Physics Conference Series* 1618(3):32007, 2020.
6. A. Viré, A. Derksen, **M. Folkersma**, K. Sarwar. "Two-dimensional numerical simulations of vortex-induced vibrations for a cylinder in conditions representative of wind turbine towers", *Wind Energy Science* 5(2):793-806, 2020.
7. **M. Folkersma**, R. Schmehl, A. Viré. "Fluid-Structure Interaction of Inflatable Wing Sections", *Book of Abstracts of the International Airborne Wind Energy Conference*, 2019.
8. **M. Folkersma**, P. Thedens, R. Schmehl, A. Viré. "Fluid-Structure Interaction of Inflatable Wing Section", *Proceedings of the 8th International Conference on Coupled Problems in Science and Engineering*, 2019.
9. **M. Folkersma**, R. Schmehl, A. Viré. "Boundary layer transition modeling on leading edge inflatable kite airfoils", *Wind Energy* 22:908– 921, 2019.
10. **M. Folkersma**. "Coupling OpenFOAM and MBDyn with preCICE coupling tool", *Proceedings of CFD with OpenSource Software*, 2019.
11. A. Viré, A. Derksen, **M. Folkersma**, K. Sarwar. "Two-dimensional numerical simulations of vortex-induced vibrations for wind turbine towers", *Wind Energy Science Discussions*, 2019.
12. **M. Folkersma**, P. Thedens, R. Schmehl. "Fluid-Structure Interaction of Inflatable Wing Section", *Proceedings of the 13th OpenFOAM Workshop*, 2018.
13. **M. Folkersma**, R. Schmehl, A. Viré. "Fluid-structure interaction simulations on kites", *Book of Abstracts of the International Airborne Wind Energy Conference*, 2017.